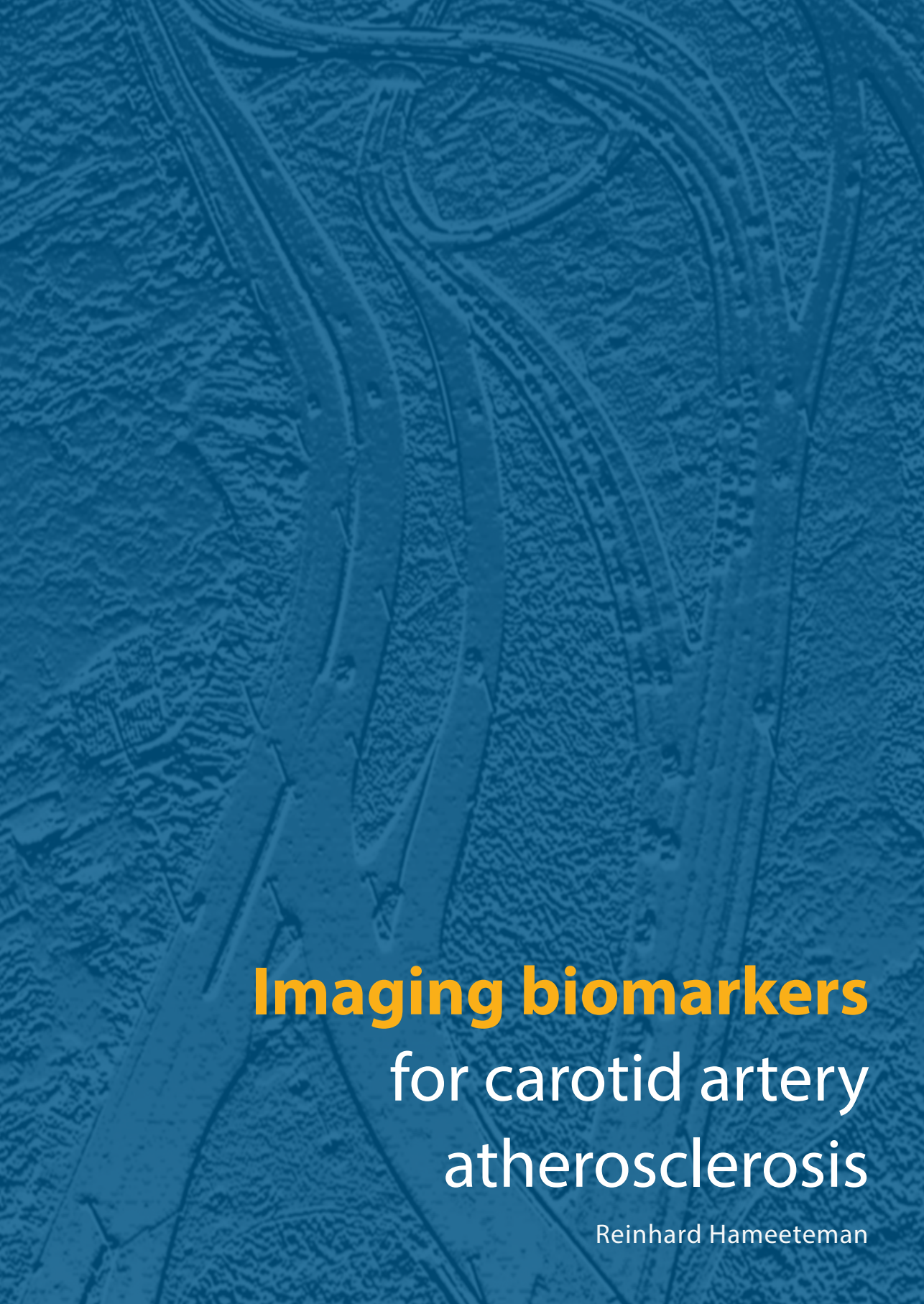

Imaging biomarkers for carotid artery atherosclerosis

Reinhard Hameeteman

Imaging biomarkers for carotid artery atherosclerosis

Beeldgebaseerde biomarkers voor atherosclerose van de halsslagader

Proefschrift

ter verkrijging van de graad van doctor aan de Erasmus Universiteit Rotterdam op gezag van de rector magnificus

Prof.dr. H.A.P. Pols

en volgens besluit van het College voor Promoties.

De openbare verdediging zal plaatsvinden op

dinsdag 26 november 2013 om 15.30 uur

door

Krijn Hameeteman

geboren te Tholen.

Promotiecommissie

Promotor	:	Prof.dr. W.J. Niessen
Overige leden	:	Dr.ir. J.J. Wentzel Prof.dr.ir. B.P.F. Lelieveldt Prof.dr. M. Prokop
Copromotor	:	Dr.ir. S. Klein

Imaging biomarkers for carotid artery atherosclerosis

Reinhard Hameeteman

ISBN: 978-90-5335-755-2

Layout and cover design: Reinhard Hameeteman

Financial support by the Netherlands Heart Foundation for the publication of this thesis is gratefully acknowledged.

The publication of this thesis was further financially supported by: the department of Radiology, Erasmus MC; Quantib BV; Cardialysis; Medis medical imaging systems bv.

The work in this thesis was conducted at the Departments of Radiology and Medical Informatics at the Erasmus MC, University Medical Center, Rotterdam, The Netherlands.

Printed by Ridderprint BV.

Contents

Chapter 1

Introduction

1.1 Background

Cardiovascular diseases (CVD) are the leading cause of death in the western world and their prevalence is rising. Currently CVD account for approximately one out of every five lives (Roger *et al.*, 2011). The primary cause of CVD is atherosclerosis, a disease of the vessel wall.

In Figure 1.1 the structure of an arterial vessel is shown schematically. Looking outwards from the center of the vessel it consists of the following parts:

- **lumen** - this is the central area of the vessel where the blood flows through
- **tunica intima** - this layer is composed of a thin sheet of endothelial cells surrounded by a thin elastic layer
- **tunica media** - this is a layer of smooth muscle cells
- **tunica adventitia** - also called tunica externa. This is the outside part of the artery which is made up of an elastic sheet surrounded by collagen

Atherosclerosis causes thickening of the vessel wall due to the accumulation of fatty materials such as cholesterol between the tunica intima and the tunica media. These areas with fatty materials are called plaques. If the vessel wall thickens, the lumen area may get narrower (stenosis) and the blood flow through the vessel may become compromised. Eventually this thickening of the wall can lead to a total occlusion of the vessel. Stenosis of the artery affects the blood and oxygen supply to the distal organs. In the case of the carotid artery, which is the vessel studied in this thesis, this is the brain. Decreased blood supply to the brain can have fatal consequences.

As mentioned, plaque growth may lead to luminal stenosis. Besides this luminal narrowing it is also possible for the plaque to 'grow outwards' while the vessel remodels. In this

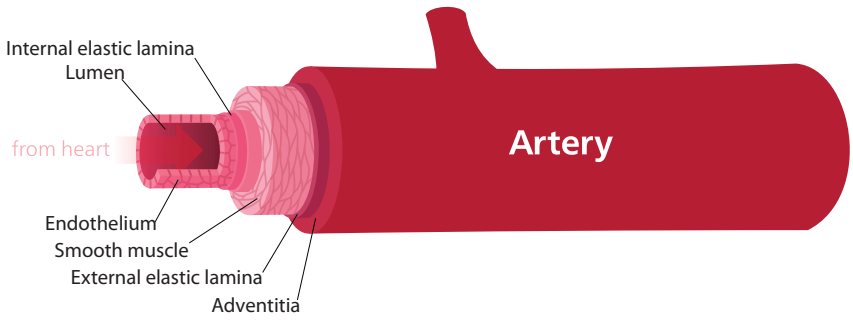

Figure 1.1: Composition of an artery (image adapted from wikimedia).

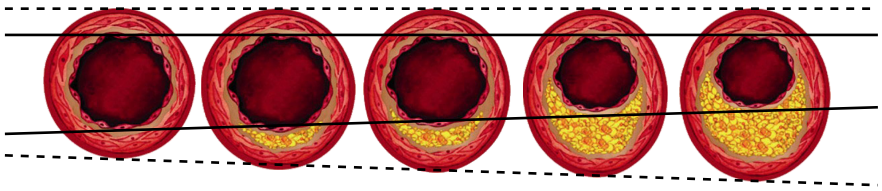

Figure 1.2: Visualization of atherosclerotic plaque development. The plaque buildup in the vessel wall leads to both inward and outward remodeling of the wall: the vessel gets bigger and the lumen becomes smaller (image adapted from www.multivu.com).

case the lumen is hardly compromised and the degree of stenosis is not a good marker for atherosclerosis. Figure 1.2 visualizes both directions of plaque growth.

Plaque rupture constitutes a larger risk to the individual with atherosclerosis than gradually increasing stenosis. If the plaque that is built up in the vessel wall enters the blood stream, the fatty material of the plaque that is carried along by the blood stream may block smaller vessels downstream, leading to cerebral ischemia (Glagov *et al.*, 1987). Even when there is no effect on the blood flow, atherosclerosis can thus still be dangerous. Therefore, much research is aimed at finding plaque characteristics (biomarkers) that can be used besides the stenosis grade to improve risk stratification and for monitoring the progression of atherosclerotic disease.

In this thesis we focus on a specific area of the carotid artery. Each person has two carotid arteries, one on either side of the neck. On the proximal side the arteries connect to the aortic arch while distally they are part of the circle of Willis. The carotid artery can be divided into the common carotid artery (CCA), the external carotid artery (ECA) and the internal carotid artery (ICA) (see Figure 1.3). The CCA is connected to the aortic arch and has a main bifurcation approximately at chin level where it splits into the ECA that supplies blood to the face, and the ICA that is the major blood supplier to the brain. All analyses in this thesis are focused on the area around the carotid bifurcation. This is the area of the carotid artery that is most prone to plaque formation (Yuan *et al.*, 2001).

To image the carotid artery bifurcation we use two imaging modalities in this thesis: Computed Tomography Angiography (CTA) and Magnetic Resonance Imaging (MRI). Carotid artery CTA imaging can be used to visualize the vessel lumen. A contrast agent is injected into the blood stream to increase the attenuation of the blood, which causes hyper-intensities for the vessel lumen. This provides the possibility to measure the stenosis grade. Without contrast agent Computed Tomography (CT) is very well suitable to visualize calcifications within the plaque. When the electrocardiography (ECG) is recorded together with multiple CTA acquisitions of the carotid artery, the images from the CTA can be correlated with the ECG signal and a 4D reconstruction can be made which shows the carotid at different phases of the cardiac cycle (Prokop, 2012). This type of acquisition can be used to study the dynamic

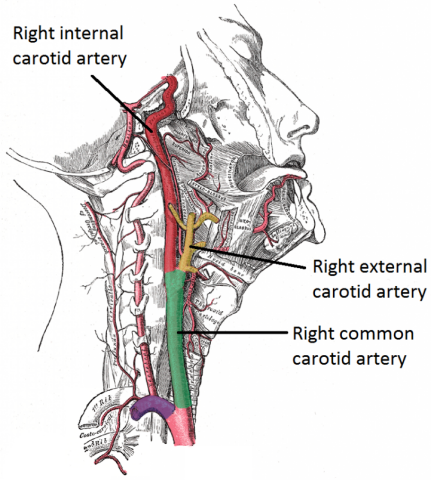

Figure 1.3: Drawing of the carotid artery and its major components: the CCA (between the aortic arch and the bifurcation), the ICA (connecting the brain) and the ECA (connecting the face) (image adapted from wikimedia).

properties of the artery. Carotid artery MRI offers the possibility to visualize several properties of the artery. Through the combination of several MR pulse sequences it is possible to distinguish between the different parts of the vessel. Magnetic Resonance Angiography and black blood imaging can be used to visualize the lumen which provides the possibility to measure luminal stenosis. Black blood and T2 weighted images can be used to visualize the outer vessel wall, which enables assessment of the wall thickness (Yuan *et al.*, 1995, 2001; Varghese *et al.*, 2005). An advantage of CTA over MRI imaging of the carotid artery is that it is fast, offers a high spatial resolution and is relatively cheap. And advantage of MRI is that it does not require ionizing radiation and that it offers more possibilities to distinguish tissue types.

1.2 Purpose

Quantitative imaging biomarkers (QIBs), are parameters derived from imaging data that can be used for the prediction, detection, staging or grading of a disease or for the assessment of treatment response. The advantage of imaging biomarkers over *e.g.* biochemical or histological biomarkers is that they can be noninvasive (*i.e.* when a noninvasive imaging modality such as CT or MRI is used), and are spatially resolved (ESR, 2010). QIBs may be simple scalar values derived from a single image, such as the diameter or cross-sectional area of the carotid artery lumen and the stenosis grade. But in the case of a time series of images it is also possible to quantify the dynamic behavior and, for example, measure the cross-sectional elasticity

of the artery.

Qualification of imaging biomarkers involves *i.a.* the following steps: (1) initial introduction of robust and standardized procedures, (2) correlation with pathology, (3) cross-sectional correlations, (4) correlation with outcome and estimation of effect size (Waterton and Pylkkanen, 2012). The research presented in this thesis is mainly focus on the first step which involves standardization of the acquisition protocols and post-processing methods (ESR, 2010). In Chapter 6 we also address step three.

Manual measurement of QIBs are subject to inter- and intra-observer variations and also often require extensive manual labor. To overcome these difficulties and standardize the measurement, much research is done in finding methods that automate the measurements of QIBs. In this thesis we present and evaluate automated methods for the measurement of four QIBs for carotid artery atherosclerosis on CTA and MRI images: two morphological biomarkers (luminal stenosis on CTA and vessel wall volume on MRI), and two functional biomarkers on CTA (distensibility and longitudinal deformations).

Below we briefly explain the QIBs treated in this thesis. Figure 1.4 provides a graphical presentation of these QIBs. Details can be found in the above mentioned chapters.

The stenosis grade of a vessel is the fraction of the lumen that is occluded relative to the healthy situation. Because the latter is unknown once the stenosis is measured, usually a reference lumen is used distal to the stenosis. In Figure 1.4a the stenosis grade is the ratio of the cross-sectional areas of the solid and the dotted contour. The vessel wall volume (Figure 1.4b) is the volume between the lumen (light surface) and the tunica adventitia (meshed dark surface). If there is plaque formation, the volume of the vessel wall will increase, as also can be seen in Figure 1.2. The distensibility of the carotid artery is a measure for its elasticity. It relates the change in cross-sectional area (orange area in Figure 1.4c) to the change in blood pressure. The graph on the lower half of Figure 1.4c show the cross-sectional area of the artery during a single heart beat. If there is plaque or calcification present in the vessel wall, the vessel is expected to stiffen. Figure 1.4d visualizes longitudinal deformations. Whereas the distensibility measures the cross-sectional elasticity, the longitudinal deformations measure the elasticity of the artery in the direction of the centerline (dark dots).

The performance of a method to measure a QIB in an automated fashion may depend on the quality of the images to which it is applied. Comparison of methods that are evaluated on distinct datasets is therefore not trivial. To alleviate this difficulty and stimulate other researcher to improve our results, all data from Chapter 3- 6 is made available through the internet. Image data and subject descriptions can be downloaded and used to improve the methods presented in this thesis or to compare to those obtained by other methods.

1.3 Thesis overview

In Chapter 2 we provide an overview of the possibilities of CT for quantification of the carotid artery lumen and plaque. In this chapter we also provide a general overview of automated lumen and plaque segmentation methods. One of the first steps in analyzing the carotid artery is the segmentation of the vessel (lumen) from the image. This is an image processing task

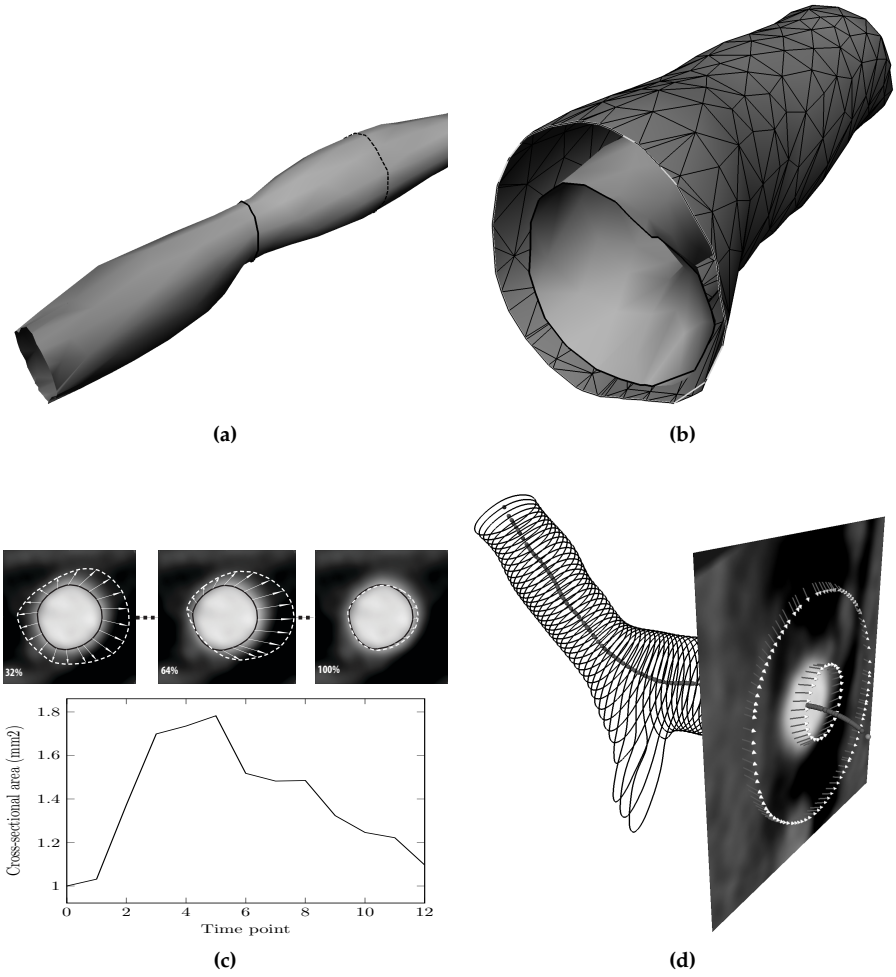

Figure 1.4: Visualization of the different QIBs that are developed and evaluated in this thesis: (a) luminal stenosis (Chapter 3) is the ratio between the cross-sectional areas of the two contours (b) vessel wall volume (Chapter 4) is the volume of the vessel between the lumen border (light surface) and the outside of the adventitia (meshed dark surface) (c) distensibility (Chapter 5) is the maximal cross-sectional area change (indicated by the arrows) during one heart cycle divided by the minimal cross-sectional area and the pulse pressure (d) longitudinal deformation is the displacement of the vessel wall (inner circle arrows) relative to a reference displacement (outer circle arrows).

that has been addressed by many research groups. However a standard to evaluate and compare these methods was lacking. Therefore such evaluation framework was developed and is

described in Chapter 3. Through this framework different lumen segmentation and stenosis grading methods are compared using a standardized set of CTA images and golden standard manual segmentations. In Chapter 4 an automated method to measure the volume of the carotid artery in a section around the bifurcation is presented. This method combines a model based segmentation with machine learning techniques. Using two MRI sequences the method finds both the lumen and outer vessel wall border. The image data of this study has been acquired in the context of a population based imaging study (Ikram *et al.*, 2011). The next QIB for atherosclerosis we analyze is vessel wall elasticity. In Chapter 5 we present and evaluate an automated method to measure the carotid artery distensibility from 4D CTA images. Distensibility is a measure that captures the change in cross-sectional area relative to the change in blood pressure during a heart cycle. In Chapter 6 we investigate two QIBs for carotid artery wall elasticity. The method to measure the distensibility from Chapter 5 is extended so it can also be used to assess the deformations in the direction of the vessel centerline. We compare the distensibility to these longitudinal deformations and analyze the relation of both elasticity measures with several cardiovascular risk factors.

We conclude this thesis with a discussion and recommendations for future research in Chapter 7.

Chapter 2

Quantitative CT imaging of carotid arteries

Based on:

M.J. van Gils, K. Hameeteman, M. van Straten, W.J. Niessen, and A. van der Lugt, Quantitative CT Imaging of Carotid Arteries, in *Multi-modality atherosclerosis imaging and diagnosis*, L. Saba, J.M. Sanches, L.M. Pedro, J.S. Suri. (Eds.), Springer 2013.

2.1 Background

Stroke is the second leading cause of mortality in the Western world after coronary heart disease. Although stroke death rate declined to 44% in the last decade, the burden of disease remains high (Roger *et al.*, 2011). Of all strokes, 87% are ischemic, 10% are intracerebral hemorrhage and 3% are subarachnoid hemorrhage strokes (Roger *et al.*, 2011). About 50% of the ischemic strokes are due to atherosclerotic disease, which is preferentially located in the carotid artery (Warlow *et al.*, 2003).

Till now, the degree of luminal narrowing of the carotid arteries, caused by atherosclerosis, has been the only image-based risk factor for (recurrent) stroke that is used in therapeutic decision making. Large, randomized clinical trials (the North American Symptomatic Carotid Endarterectomy Trial (NASCET) and the European Carotid Surgery Trial (ECST)) have established the imaging criteria for surgical treatment in symptomatic patients. Carotid endarterectomy (CEA) is indicated for symptomatic patients with high-grade stenosis (>70%) and in selected patients with recent symptoms and moderate stenosis (50-69%) (NASCET Collaborators, 1991; ECST Collaborators, 1998; Rothwell *et al.*, 2003). In asymptomatic carotid artery stenosis, a modest benefit of CEA is described in selected patient groups (relatively young male patients) who had a severe stenosis (JAMA; Halliday *et al.*, 2004; Hobson *et al.*, 1993). However, most patients with a stenosis >70% are asymptomatic and most symptomatic patients have a carotid stenosis <70%, which suggest that other factors play an important role in the pathophysiological cascade of ischemic stroke. Especially in the group of patients with moderate carotid stenosis, it is of clinical importance to improve risk prediction.

The last decades, extensive research has been performed to increase our knowledge of the pathophysiology of atherosclerosis. Apart from luminal narrowing of the carotid artery resulting in blood flow compromise, rupture of the atherosclerotic plaque and subsequent thromboembolism is thought to result in ischemic events. Histological studies of coronary arteries and carotid arteries have found that certain atherosclerotic plaque characteristics increase the vulnerability of the plaque to rupture. Inflammation is the hallmark of vulnerability and plaques with active inflammation may be identified by extensive macrophage infiltration. Plaques with a thin cap of <100 μm and a lipid core accounting for >40% of total plaque volume are also considered highly vulnerable. Plaques with a fissured or ruptured cap are prone to thrombosis and thromboembolization (Naghavi *et al.*, 2003). Carotid plaque ulcerations on digital subtraction angiography (DSA) have been associated with plaque rupture (Lovett *et al.*, 2004) and with an increased risk of acute recurrent ischemic events (Eliasziw *et al.*, 1994; Rothwell *et al.*, 2000). Advanced invasive and noninvasive imaging technologies enable the visualization of these atherosclerotic plaque characteristics in vivo.

DSA has long been the modality of choice for imaging carotid arteries, since it accurately visualizes the vascular lumen and its contours. However, DSA has several disadvantages: it is invasive, laborious, time intensive, and expensive. Moreover, DSA requires skilled operators and is therefore less readily available. More importantly, cerebrovascular DSA has a non-negligible morbidity and mortality, with a complication rate of 0.4-12.2% for neurological deficits (Hankey *et al.*, 1990a; Willinsky *et al.*, 2003). These drawbacks and the increasing

interest in the arterial vessel wall have driven the use of other, less invasive modalities for imaging the carotid arteries.

Nowadays, noninvasive imaging techniques like duplex ultrasound (DUS), magnetic resonance imaging (MRI), and computed tomography (CT) not only enable grading of carotid stenosis but also provide a window to the atherosclerotic process in vivo (Saba *et al.*, 2012). They also allow for the quantification of plaque measures like plaque burden and plaque composition.

Using serial imaging, the early natural development of the atherosclerotic plaque can now be studied in vivo. Furthermore, it provides a tool to monitor changes in atherosclerotic plaque in response to secondary preventive therapies. The development of new pharmaceutical therapies is a slow and costly process, since the most reliable way to measure their clinical impact is to study its effect on clinical endpoints. The use of imaging biomarkers of atherosclerotic disease could speed up this process and reduce the number of subjects studied. For an effective use, imaging biomarkers should be derived in a robust, noninvasive way and the imaging modality should be broadly available (ESR, 2010). Further, standardized image acquisition parameters and post-processing methods are required and the imaging biomarkers should be carefully validated and highly reproducible. The changes in an imaging biomarker should be correlated to the biological effect and the clinical endpoints (ESR, 2010). Quantification, and especially automated quantification, of the degree of stenosis and atherosclerotic plaque measures is therefore important in the development of reliable surrogate endpoints for atherosclerosis.

Computed tomography angiography (CTA) is a potential imaging modality for monitoring atherosclerosis in vivo. It is a readily available and fast imaging technique causing minimal inconvenience for the patient. Although CTA involves potentially harmful ionizing radiation, the effective dose during a diagnostic CTA is relatively low (1-5 mSv) (Beitzke *et al.*, 2011). The increased acquisition speed of multidetector CT angiography (MDCTA) reduces motion artifacts. Current multidetector row CTA enables fast vascular imaging from the aortic arch to the intracranial vessels. This enables simultaneous investigation of other vascular territories, which makes that MDCTA can compete with other noninvasive imaging techniques and is increasingly used in the clinical evaluation of stroke patients. In this chapter, the state-of-the-art CTA technique used to evaluate carotid artery stenosis and atherosclerotic plaque is described.

2.2 Luminal imaging using CTA

2.2.1 Technical aspects

In the early 1990s spiral CT was introduced, which enabled a volumetric data acquisition through continuous X-ray source rotation and simultaneous continuous table movement. Using this technique noninvasive imaging of blood vessels became widely available. The steady increase of the longitudinal coverage of the X-ray detectors, i.e., the number of slices, even further improved the feasibility of luminography.

Contrast material is necessary for the visualization of the lumen. Stenosis measurement relies upon the contrast difference between the lumen and its environment. Several technical factors should be taken into account when imaging vessel lumen using MDCTA.

The contrast difference between lumen and surrounding tissue is varying and depends mainly on the amount of lumen attenuation which is artificially increased by contrast material. The attenuation caused by contrast material can vary depending on patient-related factors like cardiac output and weight and on scan parameters and contrast protocol-specific factors. Peak tube voltage (kVp) influences the difference in HU values between different tissues. The lumen contrast density increases as tube voltage decreases. The lumen enhancement pattern is determined by the injection volume, the injection rate, and the iodine concentration in the contrast material (Cademartiri *et al.*, 2002). Timing of contrast bolus arrival should be such that a maximum contrast density is achieved in the carotid artery with a concomitant low contrast density in the neighboring jugular vein. Use of a saline bolus chaser reduces the amount of contrast material needed by 20-40% and reduces the extent of perivenous artifacts caused by a high contrast density in the jugular vein citepCademartiri2002. Synchronization between passage of the contrast bolus and data acquisition can be achieved by real-time bolus tracking at the level of the ascending aorta. Moreover, a craniocaudal scan direction also reduces contrast material-related perivenous artifacts (De Monyé *et al.*, 2006). The contrast injection protocol for carotid artery imaging is generally standardized with a fixed contrast volume of 80-125 mL (iodine concentration of >300 mg/mL) and a saline bolus chaser of 40 mL, both at an injection rate of 2-4 mL/s. The disadvantage of intravenous contrast in CT angiography remains its limited application in patients with renal insufficiency and hyperthyroidism.

Because of the limited spatial resolution of the CT scanner partial volume averaging occurs, leading to the so-called blooming artifact. This is easily appreciated at the boundary of the enhanced lumen and the vessel wall where differences in density are large. In subtle cases this is reflected in a blurred interface between structures as well. Partial volume averaging may influence the appreciation of the real luminal dimensions and therefore the accuracy of the stenosis measurements. The extent of blooming also depends on the convolution kernel chosen in the filtered-back projection algorithm. Sharp convolution kernels increase the contrast of small dense structures as the blurring is reduced, whereas smooth kernels lead to averaging of contrast differences. The signal-to-noise-ratio on the other hand improves when applying a smooth kernel because the image noise is reduced.

The appearance of the lumen-wall interface is influenced by adjustment of the window-level setting. Each lumen contrast opacification has been shown to theoretically have its own optimal window-level setting for which lumen measurements are most accurate (Liu *et al.*, 2000). When calcifications border the lumen, the two hyperdense structures may be difficult to differentiate from each other, impeding accurate lumen measurement. Normally, in CTA a large window width (500-1000 HU) is used, which can be adjusted by the reader dependent on the lumen attenuation and the presence of calcifications near the lumen in order to improve the visual differentiation between dense structures. Figure 2.1 illustrates the influence of window-level setting and convolution kernels on the evaluation of the lumen.

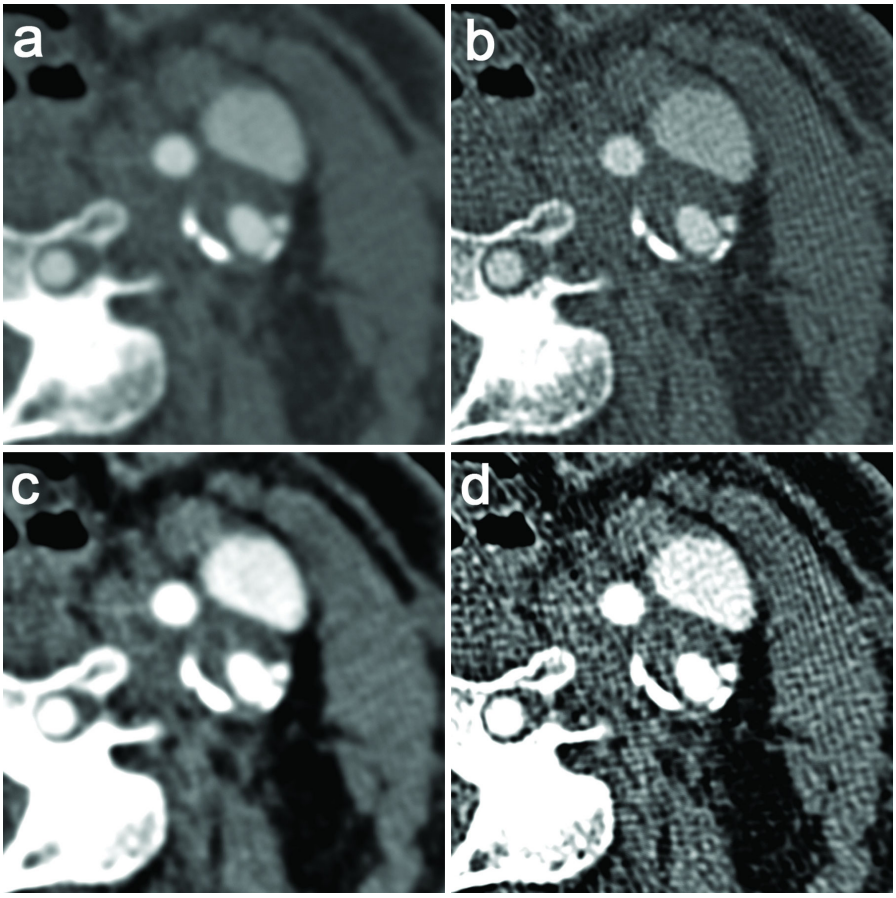

Figure 2.1: Four axial MDCT images through the carotid bifurcation obtained with a smooth (a+c) or a sharp (b+d) kernel and with a larger (W1000 L200; a+b) or smaller (W400 L100; c+d) window width setting. A large window width (a+b) gives a better differentiation between lumen and neighboring calcifications, which mostly appear brighter. A smaller window width (c+d) enables visualization of the small density differences inside the non-calcified part of the plaque. A sharper reconstruction kernel (b+d) increases the contrast between the small dense calcifications and the surrounding structures, whereas a smoother kernel (a+c) leads to averaging of contrast differences, which gives a smoother appearance to the structures.

In MDCTA images a challenge is formed by the artifacts from extra luminal dense structures like dental material, bone, and atherosclerotic calcifications which might obscure a clear visualization of the lumen. Correct head positioning with a slight tilt of the head and an upright position of the chin reduces the effect of beam hardening artifacts from dental material at the level of the carotid bifurcation, the predilection place for atherosclerotic disease in the

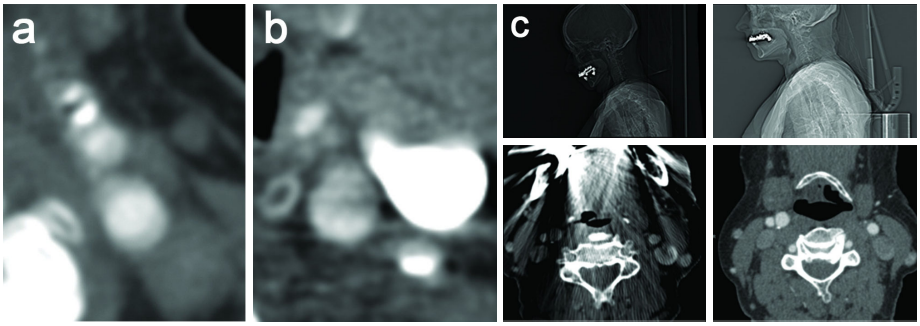

Figure 2.2: (a) Axial image at a level above the carotid bifurcation showing motion artifacts due to swallowing. The tissue boundaries are heavily blurred. (b) The dependent part of the jugular vein is filled with high density contrast material, which causes streaks of low attenuation, artificially introducing a low contrast area in the neighboring carotid artery and hampering visualization of its wall. (c) Dental material can cause enormous streak artifacts (images on the left), impeding correct judgment of surrounding structures. A slight upward tilt of the chin moves these artifacts away from the region of interest and allows a normal visualization of the larger part of the carotid bifurcation (as shown on the right).

carotid artery (Figure 2.2).

As described, convolution kernels and window-level settings highly influence the appearance of high density structures like calcifications. In addition, with a fixed window-level setting, calcification volumes appear smaller in higher kVp-settings (De Weert *et al.*, 2005).

From the cross-sectional source images, 2D or 3D image reconstructions can be created which aid in the identification and measurement of the maximal stenosis. Multiplanar reconstructions (MPR) and curved planar reconstructions (CPR) provide 2D images of any predefined plane and enable accurate stenosis measurement. For creating a longitudinal view of the artery, CPR has the advantage over MPR that it corrects for vessel curvature outside of the plane. Shaded surface display (SSD), volume rendering (VR), and maximum intensity projection (MIP) are all 3D techniques with their own strengths and weaknesses. In SSD all pixels with densities below a certain threshold are excluded and the remaining data are viewed as if their surfaces are illuminated by a point source. VR utilizes the image intensities directly, by assigning opacity and color coding, to create 3D reconstructions. Both techniques are less useful for carotid artery stenosis measurements. MIPs are created by projection of the maximum intensity pixels from a 3D data set on a predefined 2D plane and give a simple overview of the vessel and its stenosis. However, this technique is limited in arteries with atherosclerotic calcifications, since calcifications in the vessel wall can easily cover the contrasted lumen causing overestimation of the degree of luminal stenosis. In addition, bony structure like the spine, thyroid cartilage, cricoid, and hyoid might interfere with a clear overview of the artery in 3D post-processing techniques (Figure 2.3).

New techniques have been investigated that might solve the problem of artifacts from

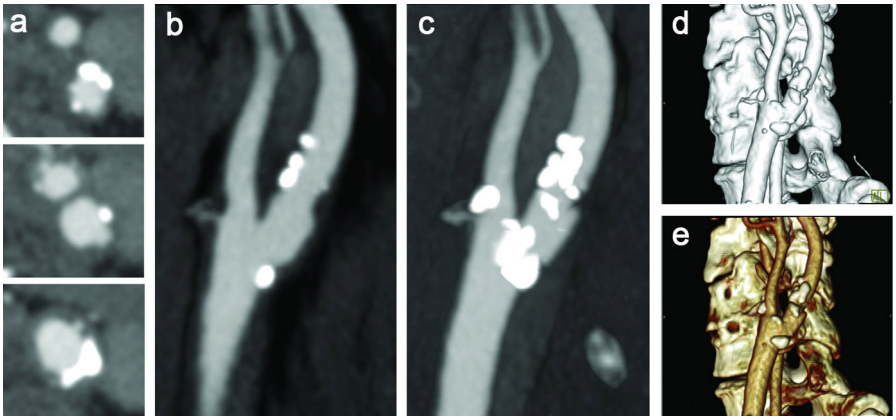

Figure 2.3: (a) Axial slices through the common carotid artery (lower image), the level of the carotid bifurcation (middle) and a level above the bifurcation (upper image). (b) Multiplanar reformat (MPR) in the sagital plane visualizing the atherosclerotic plaque around the bifurcation. (c) Maximum intensity projection (MIP, 8.8 mm) in the same plane. Over projection of calcifications hampers a clear visualization of the lumen. (d) Volume rendering (VR) shows a 3D reconstruction of the carotid artery. (e) Shaded surface display (SSD) of the same carotid bifurcation. Both last techniques suffer from over projection of calcifications.

bone and calcifications on images. Matched mask bone elimination (MMBE) is a technique for the automated removal of bone pixels from CTA data sets. Preceding to the CT angiography a non-enhanced data set is acquired on which the bone pixels are identified. The corresponding pixels on the registered CT angiography are assigned an arbitrarily low value and MIP images free from overprojecting bone can then be obtained (Van Straten *et al.*, 2004; Venema *et al.*, 2001). Whereas for MMBE, acquisition and registration of two separate datasets is necessary, in dual-energy CT (DECT) two image data sets can be simultaneously acquired with different tube voltages (for example 80 and 140 kVp). Tissues can be differentiated by analysis of their attenuation differences depending on the tube voltage. The attenuation difference is especially large in materials with a high atomic number, such as iodine. Bone and calcifications, which show a smaller attenuation difference, can therefore be differentiated from iodine in the carotid lumen. As a result, calcifications can be removed from the contrast-filled lumen, enabling quantification of carotid stenosis in heavily calcified arteries (Uotani *et al.*, 2009). However, because in both techniques an additional rim around the calcified pixels is removed due to blooming artifacts, overestimation of the grade of stenosis can still be introduced.

2.2.2 Stenosis measurement

The accuracy of the stenosis measurement is important, given its role in clinical decision making with respect to carotid endarterectomy. Traditionally, the stenosis in the carotid artery was assessed using intra-arterial digital subtraction angiography (DSA), which is still con-

sidered the gold standard. The degree of stenosis was defined as the residual lumen at the stenosis as a percentage of the normal lumen in the distal internal carotid artery (according to the NASCET criteria) or as the residual lumen as a percentage of the estimated original diameter of the artery at the level of the stenosis (according to the ECST criteria). In the large symptomatic carotid surgery trials, conventional DSA was performed in two or three projections (lateral, posterio-anterior, and/or oblique) which were investigated for the most severe stenosis.Whereas rotational DSA, using multiple planes, showed to provide a benefit in detecting the smallest diameter in a stenosed artery compared to conventional DSA (Elgersma *et al.*, 1999), the association between the severity of stenosis and stroke risk and therefore the indication for surgical intervention remained based on conventional DSA.

The volumetric CTA datasets allow for MPRs and MIPs in any plane and therewith provide much more information on the lumen and its morphology than conventional DSA. The residual lumen is almost never circular and DSA performed in a limited number of projections does not always reveal the narrowest lumen. Analysis of 3D information therefore may provide a more realistic way to assess the true maximum stenosis.

In case CTA replaces DSA in clinical decision making, stenosis measurements on CTA should be performed in a comparable way, i.e., measuring the diameter of the remaining lumen at the level of the maximal stenosis and of the normal lumen distal to the stenosis. This can be done in several ways using different postprocessing techniques. Although with MIP reconstructions images comparable to those in DSA can be obtained, this technique is limited in calcified plaques and it is recommended not to use MIP images for stenosis measurements in arteries with calcifications (Figure 2.4). Generally, one uses 3D software to create MPRs and/or CPRs in oblique planes parallel to the carotid lumen to seek the point of maximum stenosis and measures the smallest diameter in the cross-sectional plane perpendicular to the central lumen line at that level. Figure 2.5 shows this method of stenosis measurement using 3D software. The reference diameter is measured in the same way at a level above the carotid bulb where the lumen walls run parallel to each other (i.e., the healthy distal carotid artery).

When using the ECST criteria to assess the degree of stenosis, CTA directly enables visualization of the outer vessel wall, whereas on DSA the vessel diameter has to be estimated by delineating the projected lumen contour. Therewith, CTA takes into account the changes in vessel diameter caused by vascular remodeling, whereas this phenomenon is ignored when measured on DSA. This might cause differences in ECST stenosis measurements between CTA and DSA.

2.2.3 Diagnostic accuracy

Several diagnostic studies have been performed which compared single slice CTA with DSA in the assessment of carotid stenosis. From a meta-analysis of studies published between 1990 and 2003, single slice CTA has been shown to have a pooled sensitivity of 85% and a pooled specificity of 93% for detection of a 70-99% stenosis. Sensitivity and specificity for detection of an occlusion were 97% and 99%, respectively (Koelemay *et al.*, 2004). Another systemic review reported a pooled sensitivity of 95% and a specificity of 98% for the detec-

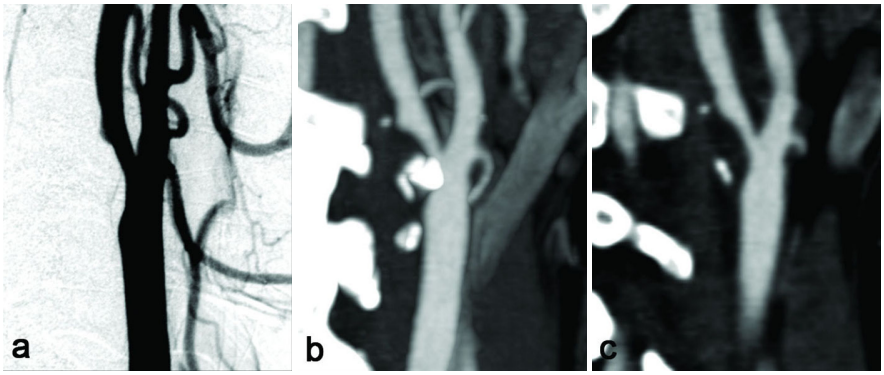

Figure 2.4: (a) Digital subtraction angiography (DSA) of a right carotid artery shows a 50% stenosis at the level of the bifurcation. (b) A maximum intensity projection (MIP, 6 mm) of MDCTA images of the same artery. MIP has the disadvantage of overprojection of calcifications over the lumen, causing overestimation of stenosis measurement. (c) A multiplanar reformatted image (MPR, 1 mm) in the same plane as the MIP in (b); the problem of overprojection does not occur here. Using MPR reconstruction of 3D data the point of maximum stenosis can be found easier compared to using DSA.

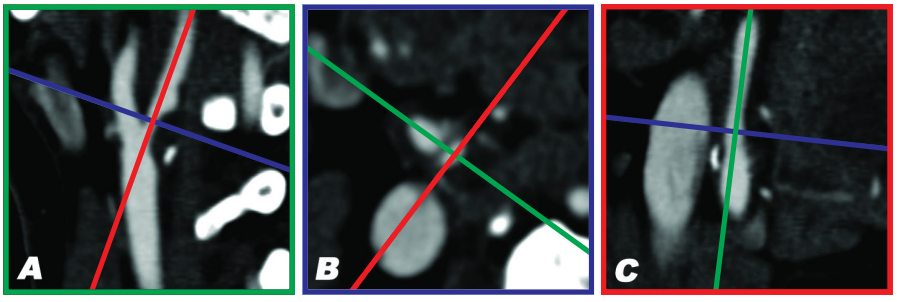

Figure 2.5: Multiplanar reformatted images are created in planes parallel and perpendicular to the lumen axis; the smallest lumen diameter in the cross-sectional plane can then be measured using calipers. (A) A sagital view of the carotid bifurcation. The dashed and dotted lines correspond to the planes that are depicted in (B) and (C). A large atherosclerotic plaque is visible at the origin of the internal carotid artery, causing a high-grade stenosis. (B) The cross-sectional image perpendicular to the central lumen line at the level of the smallest vessel diameter. The residual lumen has an oval shape. (C) The view perpendicular to (A) and (B). In this plane the stenosis is not very prominent.

tion of a 70-99% stenosis (Hollingworth *et al.*, 2003). The latter study also found that CTA was sensitive (95%), but slightly less specific (92%) in depicting stenosis >30%. In 2006, Wardlaw and colleagues performed a meta-analysis comparing noninvasive imaging techniques with intra-arterial angiography. They found only 11 studies on CTA, published between 1980 and 2004, that explicitly met the Standards for Reporting of Diagnostic Accuracy (STARD)

criteria (Bossuyt *et al.*, 2003) and they reported a sensitivity of 77% and a specificity of 95% for diagnosing 70-99% stenosis using CTA (Wardlaw *et al.*, 2006). The authors warned for the methodological shortcomings of many studies evaluating diagnostic imaging. They concluded that the existing data might support the cautious use of noninvasive imaging to diagnose 70-99% stenosis, but that more data are needed from carefully designed trials to determine true sensitivity and specificity of noninvasive imaging techniques in routine clinical practice, especially for 50-69% stenosis, or when used in combination (Wardlaw *et al.*, 2006). In 2009, Chappell and colleagues performed an individual patient data meta-analysis to find clinically significant estimates of the accuracy of noninvasive imaging in diagnosing severe and moderate symptomatic artery stenosis (Chappell *et al.*, 2009). They also concluded that existing primary studies provide limited data and that the literature overestimates the accuracy of noninvasive imaging techniques. The small CTA dataset included in this analysis revealed a sensitivity and specificity of 65% and 56% for detection of 70-99% stenosis, respectively (Chappell *et al.*, 2009).

A difficulty in the evaluation of the accuracy of stenosis measurement using noninvasive imaging techniques is that both acquisition and post-processing procedures evolve rapidly. Although multidetector CTA is now widespread and is expected to improve diagnostic accuracy, this has barely been tested. Only one study compared MDCTA with DSA and found MDCTA to have a high specificity and a high negative predictive value for significant carotid disease (Josephson *et al.*, 2004). Since DSA is not routinely used anymore in clinical practice, the assessment of new noninvasive imaging techniques against DSA can not be justified ethically anymore. Therefore there is an increasing need for practical, reliable methods for evaluating new technologies, for example, by standardized comparison with other noninvasive tests or test phantoms.

Both aforementioned systemic reviews (Koelemay *et al.*, 2004; Hollingworth *et al.*, 2003) did not provide enough evidence to draw robust conclusions about the diagnostic accuracy of the different post-processing techniques, although stenosis assessment using axial slices and MIPs seemed to be better than when using VR and SSD (Hollingworth *et al.*, 2003). Most studies did not report on the exact combinations of reformatting techniques used, which hampers a solid meta-analysis. More recent studies comparing the post-processing techniques in MDCTA revealed that stenosis measurements on axial source images are highly reproducible and accurate and that the additional use of MPRs or other reconstructions is not necessary, but might aid in finding the location of the maximum stenosis (Hackländer *et al.*, 2006; Howard *et al.*, 2010; Puchner *et al.*, 2009).

2.2.4 (Semi)automated quantification of luminal measures

Manual lumen segmentation and stenosis quantification are laborious and suffer from interobserver and intraobserver variability. Consequently much work has been performed on the development of (semi)automated lumen quantification. The majority of publications with respect to lumen quantification focus on the segmentation of the lumen while the assessment of the severity of luminal stenosis is addressed by few.

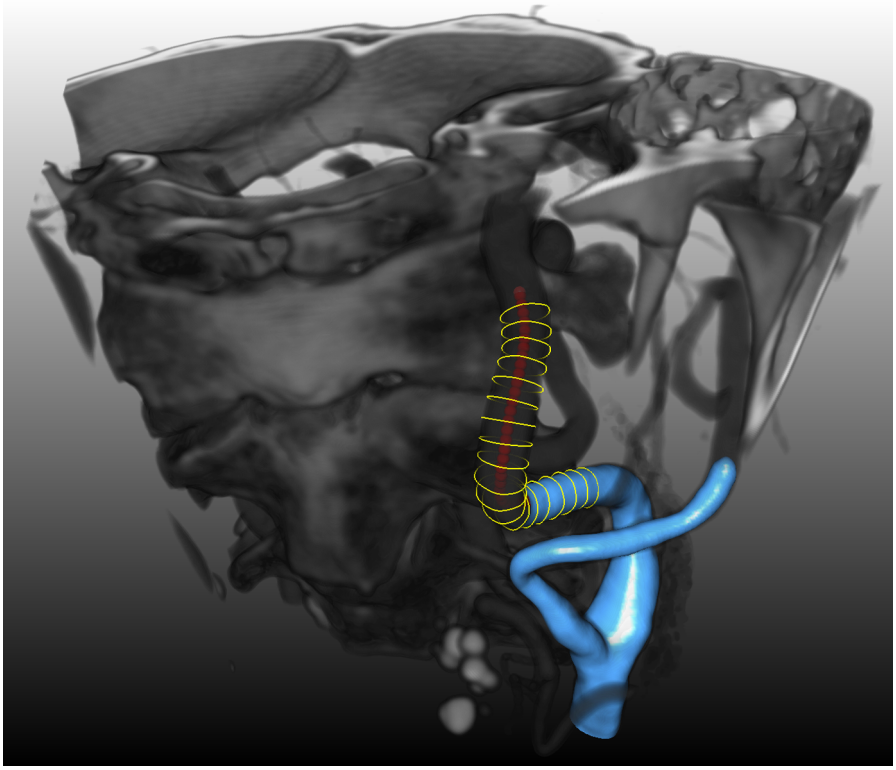

Figure 2.6: Example of a carotid artery lumen segmentation using three different segmentation representations. The dots indicate a centerline through the centroids of the vessel cross-sections. The 'circles' show the lumen contours perpendicular to the centerline. The surface shows an interpolated surface through the contours.

Lumen segmentation methods have been reviewed and grouped according to the mathematical framework used (Kirbas and Quek, 2004) or categorized with respect to (1) the way vessel geometry and appearance are modeled, (2) the image features which are used for vessel extraction, and (3) the methodology used in vessel extraction (Lesage *et al.*, 2009).

Some of the published methods have been tailored to or evaluated on carotid CTA images (Manniesing *et al.*, 2010, 2007; Baltaxe Milwer *et al.*, 2007; Cuisenaire *et al.*, 2008). Reported values vary highly. However the comparison of these methods is hampered by the fact that they all use different imaging data and evaluation measures, like Dice similarity coefficient, mean surface distances, or visual inspection. In addition, most studies were performed on small and selected data sets. Figure 2.6 illustrates a 3D lumen segmentation of a carotid bifurcation.

To facilitate an objective comparison of carotid artery segmentation and stenosis quan-

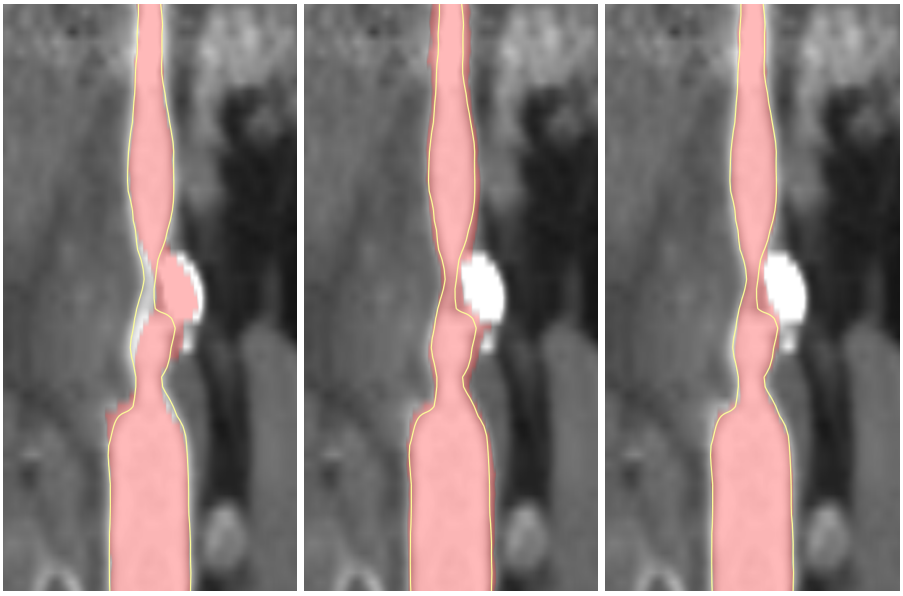

(a) (b) (c)

Figure 2.7: Curved multiplanar reformats (CMPR) of a carotid artery with a calcified atherosclerotic plaque that causes a high-grade stenosis. A visual impression is shown of automated lumen segmentations (shaded area) that have different qualities: (a) with a bad Dice similarity index (SI), (b) a moderate Dice SI and (c) a good Dice SI.

tification algorithms, the Carotid Bifurcation Algorithm Evaluation Framework was set up in 2009 (see Chapter 3) (Hameeteman *et al.*, 2011). This framework consists of a publicly available image database, annotated data for training and evaluation, and standardized evaluation measures. Till date 14 algorithms have been evaluated by the framework, of which only one is fully automatic, whereas the others require three initialization points. The three best performing methods evaluated by the framework have dice similarity coefficients of 0.92, 0.88, and 0.90, mean surface distances of 0.18, 0.54, and 0.17 mm and Hausdorff distances of 1.5, 4.4, and 1.7 mm, respectively (Hameeteman *et al.*, 2011). Figure 2.7 shows three examples of lumen segmentations with three different dice values.

These three best performing methods are based on three different approaches, i.e., graph cut, level set, and active surface algorithms (Hameeteman *et al.*, 2011).

In the graph cut framework voxels are assigned to vessel lumen or background by considering all image voxels as nodes in a three-dimensional graph and creating an optimal surface which separates (cuts) the foreground (lumen) from the background. To compute this optimal cut the image gradient can be used.

In the level set framework, the vessel surface is represented implicitly by the zero level lines (zero level set) of an embedding function (similar as, e.g., sea level in a height map). This

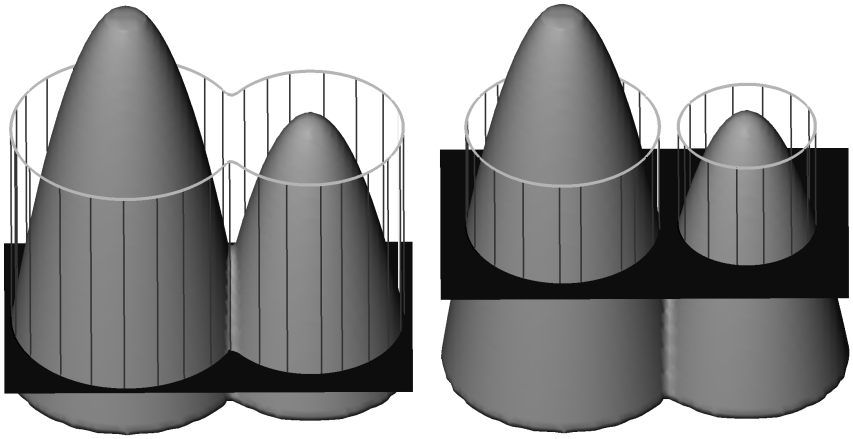

Figure 2.8: Using the level set framework a segmentation (indicated by the grey contours) is seen as the zero level (black plane) of an embedding function in a higher dimension (cone shaped surface). If the embedding function changes, as indicated by the two cones which are slightly different, the zero level (segmentation) changes. Using this framework a segmentation can easily change topology. The segmentation on the left has one object (contour) while the segmentation on the right consists of two distinct objects.

embedding function is then changed (evolved), implicitly resulting in deformation of the zero level set. This representation has the advantage that the zero level set can change topology (Figure 2.8). The evolution of the embedding function should ensure that the zero level set halts at the vessel lumen boundary. This is achieved by defining a speed function derived from the image data. Both the initial segmentation and the design of the speed image are the key ingredients in the design of a level set-based segmentation method.

Active surfaces are a generalization of active contours (also called snakes). Using active surfaces the segmentation is also the result of the evolution of an initially segmented surface. However changing topology is much harder to model in this framework. The segmentation is modeled as a surface on which forces are acting which causes the evolution of the segmentation. This evolution can be constrained by properties of the used surface representation.

Although considerable research has been performed on vessel lumen segmentation, only few researchers have published on automatic vessel stenosis grading (Scherl *et al.*, 2007; Wintermark *et al.*, 2008b; Berg *et al.*, 2005). Also, approaches differ widely in the evaluation that has been performed, both with respect to evaluation measures and number of data sets used.

The evaluation framework discussed previously also allows objective comparison of performance in stenosis quantification. To date only three stenosis grading methods have been evaluated using this framework, also indicating that this field has received less attention (Hameeteman *et al.*, 2011). Clinically, the minimal diameter is often used to calculate the stenosis degree. However, the minimal diameter of a non-elliptical shape is not uniquely de-

fined and is therefore prone to measurement errors and is hard to measure automatically. The evaluation framework evaluates two stenosis measures: an area-based measure which compares the area of the lumen at the stenosis to the area of a distal vessel part and a measure that compares the minimal diameter at the two positions. In the framework, the diameter-based stenosis degree is defined by the smallest line that divides the cross-sectional area in two equal parts. Using automated lumen segmentation, the minimal diameter can easily be replaced by the lumen cross-sectional area. This is a much more accurate measure for the obstruction of the blood flow as carotid arteries, especially at the site of atherosclerotic plaque, generally do not have circular luminal cross sections and also do not run exactly perpendicular to the axial plane of the CT scan. Zhang *et al*. investigated the use of area measurements and found that assessment of area stenosis on CTA was highly reproducible and showed a satisfactory agreement with diameter stenosis on DSA, although it provides a less-severe estimate of the degree of carotid stenosis, especially in noncircular lumens (Zhang *et al.*, 2005). The average error in assessing carotid artery stenosis of the best stenosis grading method according to the evaluation framework was 16.9% for area-based and 17.0% for diameter-based measurements (Hameeteman *et al.*, 2011).

Besides stenosis grading, lumen segmentation also enables the extraction of other quantitative measures. The extracted lumen model can, e.g., be used for Computation Fluid Dynamic calculations to assess the shear stress in the atherosclerotic carotid bifurcation (Groen *et al.*, 2007) and the quantification of geometric parameters such as vessel tortuosity and bifurcation angles (Lee *et al.*, 2008).

2.3 Plaque imaging using CTA

2.3.1 Technical aspects

Assessment of different atherosclerotic plaque components in CTA relies on the differences in linear attenuation coefficient expressed in Hounsfield Units (HU) of the plaque components. Plaque component differentiation is highly dependent on scan parameters.

Reconstruction of thin slices is very important for plaque evaluation. Thin slices allow for datasets with isotropic and higher resolution and therefore enhance the differentiation of plaque components. Especially for plaque components of which HU values are close, like lipid and fibrous tissue, thin slices are crucial.

Where blooming artifacts from vessel wall calcifications can hamper correct stenosis measurements, it also causes a problem in the evaluation of plaque, since it interferes with optimal plaque characterization of the non-calcified part of the plaque. The finite spatial resolution of CT causes partial volume averaging and therefore blooming artifacts. Blooming of calcifications leads to overestimation of calcification size and inability to evaluate the atherosclerotic regions that border the calcifications. Moreover, the calcification volume appears larger when using lower kVp settings (De Weert *et al.*, 2005).

For accurate differentiation of plaque components a high signal-to-noise ratio (SNR) is necessary. Image noise depends mainly on the product of the tube current and rotation time

(mAs), the tube voltage, and reconstruction kernel. Because the atherosclerotic plaque is a relative small structure, a thin slice thickness and a small field-of-view are required. These result in a decrease of SNR, which should be compensated by a higher radiation exposure.

High intraluminal contrast material density may influence the density measurements in the plaque. Ex vivo studies in coronary arteries revealed that intraluminal attenuation strongly affects the measured attenuation of the plaque (Cademartiri *et al.*, 2005). This can be explained not only by partial volume effects but also by the entrance of contrast material in the plaque via the vaso vasorum. It is unknown yet if this effect is also seen in the larger carotid artery, but it underlines the necessity of standardized scan protocols, especially since carotid plaque enhancement in CTA is thought to be associated with increased risk for neurological events (Romero *et al.*, 2009; Saba and Mallarini, 2011).

Another technical aspect influencing accurate differentiation of plaque components in CTA is the convolution kernel used for reconstruction of the image dataset. The convolution kernels allow for influencing the image characteristics; a smooth algorithm will reduce spatial resolution, image noise, and image contrast for tiny structures, whereas a sharp algorithm has the opposite effect. Plaque characterization and quantification of the different plaque components based on measurement of HU densities is thus highly influenced by the convolution kernel used. Smooth kernels hamper the correct differentiation between tissues with small differences in density, as is the case for lipid and fibrous tissue. In contrast, sharp kernels not only increase contrast differentiation but also lead to an increase in calcium size and low-intensity rings around calcifications (edge-enhancement artifacts), which hamper further plaque interpretation. Intermediate reconstruction kernels turned out to allow optimal plaque interpretation (De Weert *et al.*, 2005).

The window-level setting also influences the visualization of the different plaque components. Whereas a large window-width is used in luminography to differentiate lumen from calcifications that border the lumen, a small window-width is necessary to enhance the small differences in HU density inside the non-calcified plaque (Figure 2.1).

2.3.2 Diagnostic accuracy

Plaque surface morphology

The accuracy of DSA in the detection of plaque ulceration, as compared to macroscopic surgical observations, has been found to be low (sensitivity 46% and sensitivity 74%) (Streifler *et al.*, 1994). CTA allows for analysis of the plaque surface (Figure 2.9) and the differentiation between ulcerations and irregularities and has been demonstrated to perform better than DSA (Randoux *et al.*, 2001). A validation study, comparing single slice CTA with histological specimens reported a sensitivity and specificity of 60% and 74%, respectively (Walker *et al.*, 2002). However, MDCTA has been found to have a high sensitivity and specificity (94% and 99%, respectively) in detecting plaque ulcerations compared to surgical observation (Saba *et al.*, 2007). Assessment of plaque ulceration on MDCTA is highly reproducible (κ >0.86) (De Weert *et al.*, 2009; Wintermark *et al.*, 2008c).

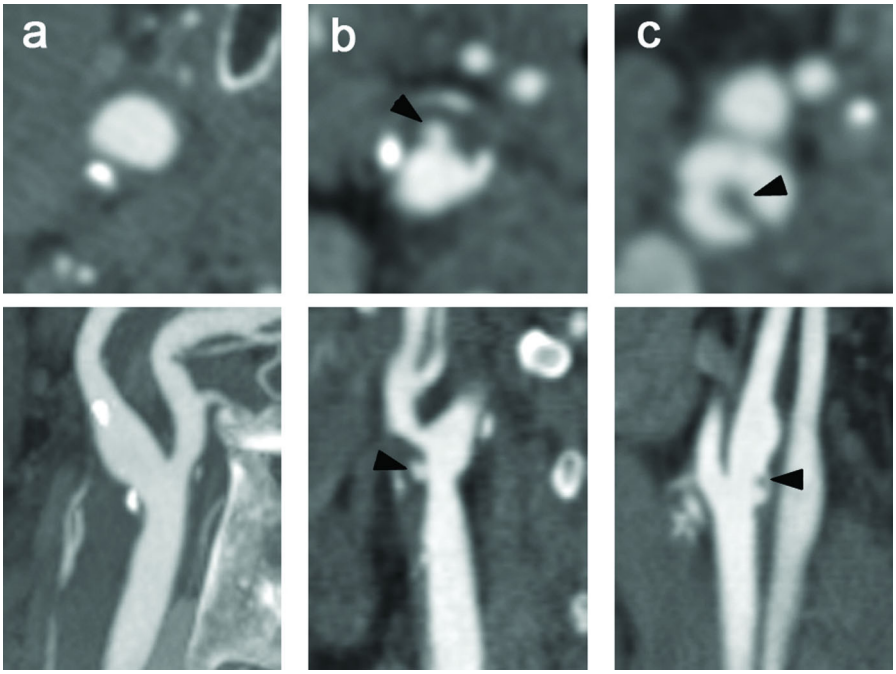

Figure 2.9: Cross-sectional images (upper panels) perpendicular to the central lumen line and multiplanar reformats (lower panels) of carotid bifurcations. (a) An atherosclerotic carotid plaque with a smooth surface. (b) A plaque at the level of the carotid bifurcation with an ulceration. (c) An ulcerated plaque with thrombus material that protrudes into the lumen.

Plaque composition

The first validation studies compared 3 mm single slice CT images with histological sections from carotid endarterectomy specimens and did not show clear-cut results. Whereas two studies reported that calcifications, lipid, and fibrous tissue could be differentiated based on density measurements (Estes *et al.*, 1998; Oliver *et al.*, 1999), another study concluded that single slice CT was not sufficiently robust to reliably characterize plaque composition and plaque morphology (Walker *et al.*, 2002). The introduction of multidetector CT enabled a more detailed analysis of the atherosclerotic carotid plaque composition and the differentiation of plaque components.

Several validation studies have been performed, in carotid arteries as well as in coronary arteries. In coronary artery studies, intravascular ultrasound (IVUS) is used as a gold standard. In carotid artery studies, the availability of histological carotid plaque specimens from carotid endarterectomy enables reliable validation against histology. An additional advantage is that the characterization of the separate plaque components can be performed easier and in more detail in the larger carotid arteries. In 2005, we performed an ex vivo valida-

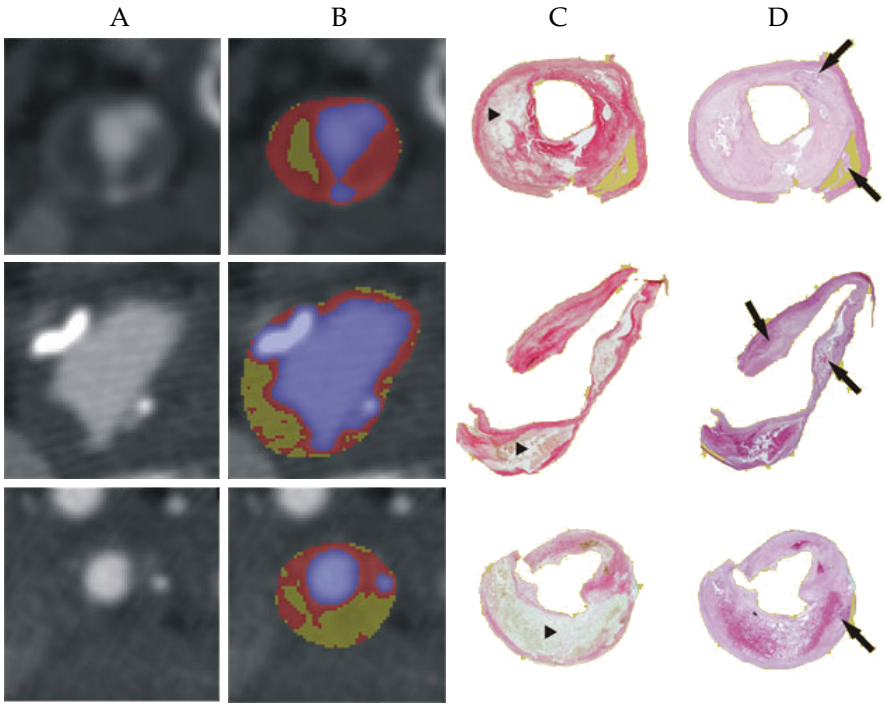

Figure 2.10: Column A: axial MDCT images of a carotid artery with atherosclerotic plaque. Column B: MDCT plaque composition based on HU differences. Column C+D: Corresponding histological sections with Sirius Red (SR) and haematoxylin eosin (HE) staining, respectively. Blue regions in the MDCT plaque composition images correspond well with lumen and calcifications on HE stained histological sections (arrows). The red regions correspond well with the red collagen-rich regions in the SR stained sections. Yellow regions correspond with the lipid core (i.e. lipid, hemorrhage and necrotic debris) (arrowhead) regions on histology (the non-red regions on the SR stained sections that are not calcified areas on the HE stained sections). (Reprinted with permission from *de Weert TT, Ouhlous M, Meijering E, et al (2006) In vivo characterization and quantification of atherosclerotic carotid plaque components with multidetector computed tomography and histopathological correlation. Arterioscler Thromb Vasc Biol 26 (10):2366-2372)*

tion study, in which CEA specimens were scanned and the images were compared with the histological slices (Figure 2.10). The CT value of lipid-rich regions differed significantly from that of fibrous-rich regions (45 ± 21 HU versus 79 ± 20 HU, $p<0.001$). An ROC analysis revealed 60 HU as the optimal cut-off point for differentiation between lipid and fibrous tissue, with a sensitivity of 89% and a specificity of 93% (De Weert *et al.*, 2005). The study was repeated in vivo, in which the CT values for lipid- and fibrous-rich tissue were 25 ± 19 HU and 88 ± 18 HU, respectively. Again an optimal threshold value of 60 HU was found, with a sensitivity and specificity of both 100% (De Weert *et al.*, 2006). Calcifications are easily detected on CT images as high density structures and equivalent to coronary calcium scoring in electron

beam CT, 130 HU is generally taken as a threshold for differentiating calcifications.

Wintermark and colleagues performed a validation study in which they compared in vivo MDCTA images with histological sections for the non-calcified plaque components and with ex vivo MDCTA images for the calcifications (Wintermark *et al.*, 2008c). They found the following scan-parameter dependent cut-off values, determined as the half way HU attenuation value between the average HU values of each plaque component: 39.5 HU between lipid-rich necrotic core and connective tissue, 72.0 HU between connective tissue and hemorrhage, and 177.1 HU between hemorrhage and calcifications. They further compared the CT classification with the histological classification of type of atherosclerotic plaque and stage of lesion development according to the system derived from the AHA classification and found an overall agreement of 72.6% (unweighted κ of 67.6%) (Wintermark *et al.*, 2008c). The concordance for calcifications was perfect, whereas the reliability of the identification of the noncalcified plaque components was limited due to overlap of the values between the soft components. However, CTA showed good correlation with histology for larger lipid cores and larger hemorrhages. Further they demonstrated that CTA performed well in measuring fibrous cap thickness (R^2=0.77, p<0.001) (Wintermark *et al.*, 2008c).

2.3.3 Quantification of plaque components

Calcifications in the vessel wall can easily be measured in a quantitative way. Agatston and colleagues were the first to quantify coronary calcifications with electron beam CT (Agatston *et al.*, 1990). As a default, the threshold to differentiate calcification is >=130 HU in non-contrast CT scans. Although the Agatston score as a quantification tool can be used in carotid arteries, other scoring methods like a volume score are more frequently used (Kwee, 2010). However, when CTA images are used, the threshold has to be higher in order to automatically differentiate calcifications from the bordering luminal contrast. Another possibility is to first delineate the inner and outer borders of the carotid plaque and subsequently discriminate calcifications using a threshold of 130 HU within the plaque. In this way, 3D volumetric MDCTA datasets also allow for quantification of the soft plaque components.

Annotation of the luminal area can be done (semi)automatically based on thresholds that separate the bright, contrast-filled lumen from the lower density plaque. However, calcifications bordering the lumen might be included in the lumen segmentation and therefore manual correction is necessary. Using lumen and outer vessel wall contours, the plaque area can be calculated by subtracting lumen area from total vessel area. Validation studies of plaque area measurements with histology as gold standard are hampered by the fact that histological preparation leads to shrinkage of the specimens. Nevertheless, strong correlations have been found between ex vivo and in vivo MDCTA and histology for the assessment of plaque area ($R^2 = 0.81$ and $R^2 = 0.73$, respectively) (De Weert *et al.*, 2005, 2006). Intraobserver reproducibility of plaque area measurements with MDCTA was good (coefficient of variation of 8%) (De Weert *et al.*, 2006).

The CT value thresholds in HU that differentiate between plaque components create the opportunity to quantify plaque composition. The aforementioned in vivo validation study,

comparing MDCTA images with histological specimens, showed that area measurements of calcifications were overestimated by MDCTA; however the correlation with histology was good ($R^2 = 0.74$). The correlation between MDCTA and histology for fibrous area measurements was also good (R^2 0.76) but was poor for lipid (R^2 0.24). Further investigation, however, showed that this correlation improved in mildly calcified plaques and non-calcified plaques ($R^2 = 0.77$ and $R^2 = 0.81$, respectively). The intraobserver variability of area measurements of the different plaque components was low, with a coefficient of variation of 8%, 11%, and 15% for calcifications, fibrous tissue, and lipid, respectively (De Weert *et al.*, 2006).

Plaque volume and plaque component volumes can be calculated by multiplying area measurements with slice increment and the number of slices in the range of interest. In an in vivo study in 56 patients, plaque volume and plaque component volumes could be assessed in a reproducible way. The difficulty of defining the transition of normal wall into atherosclerotic plaque contributes highly to the interobserver variability. Consensus about the longitudinal dimensions of the plaque improved the reproducibility of plaque volumes strongly (De Weert *et al.*, 2008).

2.3.4 (Semi)automated plaque measurements

Manually assessing lumen and vessel contours is a time-consuming task and is highly influenced by the window-level setting. Segmentation of the outer vessel wall and subsequent automated plaque characterization has received considerably less attention than luminal analysis.

The challenge of automated analysis of carotid atherosclerotic plaque lies in the difficulty of defining the outer vessel wall. This is a challenging task due to the low and varying contrast between the plaque and its surrounding soft tissue. Vukadinovic *et al*. developed a semiautomated method to segment the outer vessel wall (Vukadinovic *et al.*, 2010), which only required clicking initialization points for lumen segmentation and clicking seed points for defining the range of interest for plaque segmentation. The method uses a level-set framework for vessel lumen segmentation (Manniesing *et al.*, 2010), followed by classification of calcium objects using a set of image features related to the appearance, shape, and size of bright objects in the CTA data set. Subsequently, image voxels are identified as lying inside or outside the vessel wall, using a same set of image features. Finally, the outer vessel wall is determined by fitting an ellipsoid that utilizes the information from the calcium and inner/outer vessel classification step. After generation of the inner and outer vessel wall contours, the plaque components (lipid, fibrous tissues, and calcifications) are automatically differentiated based on the aforementioned HU-thresholds. Figure 2.11 shows the results of (semi)automatically generated plaque segmentations.

The method has been trained and tested on manually annotated MDCTA datasets of the carotid arteries and validated against manually segmented carotid arteries. The average Dice similarity index was 91%, which was comparable to the similarity index between two observers (Vukadinovic *et al.*, 2010). Subsequently, the performance of this plaque segmentation method in quantifying plaque volume and plaque component volumes was studied by com-

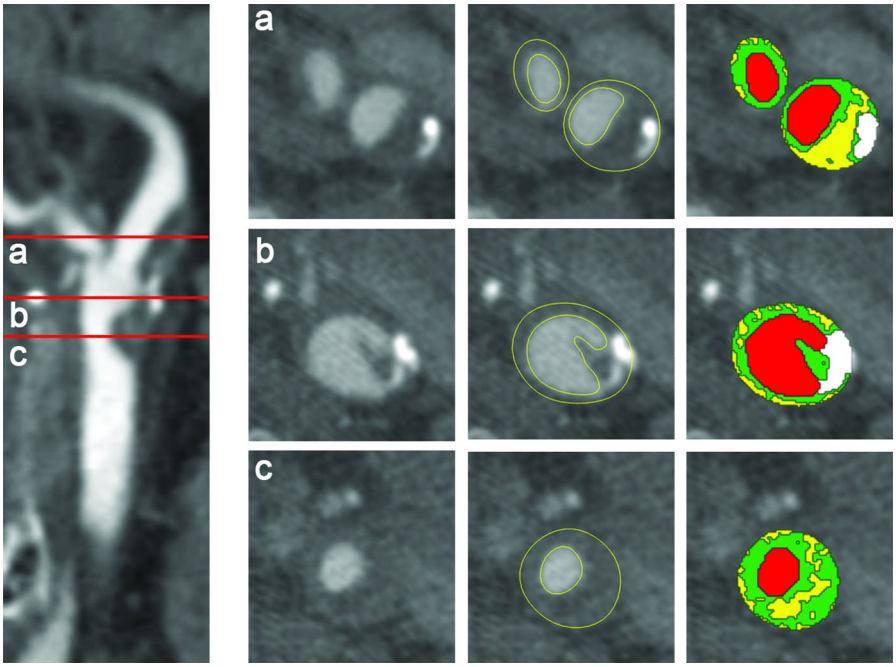

Figure 2.11: (Semi-) automated segmentation of lumen and plaque is performed on axial images within a predefined range. Contours of lumen and plaque are generated and can be manually adjusted if necessary. Within the plaque area (outer vessel wall contour minus lumen contour) the plaque components are differentiated based on Hounsfield Units (lipids: <60 HU, fibrous 60-130 HU, calcification <130 HU). The color overlay shows the different structures; lumen = red, lipid = yellow, fibrous = green, calcification = white. This figure shows a CPR image of a carotid bifurcation on the left and plaque segmentation on axial slices at three levels: (a) through the internal and external carotid artery, showing a large, mainly non-calcified atherosclerotic plaque in the internal carotid artery; (b) through the distal common carotid artery just below the bifurcation on which an ulcerated surface is visible and (c) through the common carotid artery at the level of the smallest vessel diameter.

paring measurement error of the automated method using manual contours as a reference standard with the interobserver variability in manual annotations. The differences between the automated method and the manual observers were comparable to the interobserver differences (Vukadinovic *et al.*, 2012).

Although the method is highly automated some observer interventions are still needed and the outer vessel wall segmentations should still be checked manually for erroneous in or exclusion of calcifications, and therewith over-segmentation or under-segmentation of the plaque. Taken these manual interventions into account, the intraobserver and interobserver reproducibility of the semiautomated method is better as compared to the reproducibility of manual annotating, with intraclass correlation coefficients of 0.93/0.84 for plaque volume and 0.86-1.00/0.76-0.99 for plaque component volumes (unpublished data).

2.4 Applications of quantitative atherosclerotic measures

MDCTA-based quantitative plaque measures have been used in several studies to investigate atherosclerotic development. Rozie *et al*. investigated in a cross-sectional study the correlation between cardiovascular risk factors and plaque volume and plaque composition. They found that plaque volume and severity of stenosis were just moderately correlated, which means that plaque volume could be an additional predictor for ischemic stroke. An increasing plaque volume was associated with increased lipid and calcium proportion and a decreased fibrous proportion.Age and smoking were independently related to plaque volume. Patients with hypercholesterolemia had a significantly higher contribution of calcifications and a significantly lower contribution of lipid in the atherosclerotic plaque (Rozie *et al.*, 2009). Another study investigated whether plaque features could be correlated with the presence of ulcerations, which is thought to be a marker of plaque rupture (Lovett *et al.*, 2004). It was demonstrated that degree of stenosis, plaque volume, and the proportion of lipid-rich necrotic-core were associated with the presence of carotid plaque ulcerations (Homburg *et al.*, 2011). In another cross-sectional study, carotid atherosclerotic plaque features were identified that were significantly different in acute carotid stroke patients compared to non-stroke patients and on the infarct side compared to the contralateral side in stroke patients. These features included increased vessel wall, thinner fibrous caps, greater number of lipid cores, and their location closer to the lumen. The number of calcium clusters was a protective factor (Wintermark *et al.*, 2008a).

Numerous studies report on the role of plaque calcifications in plaque stability. The findings are not conclusive. A recent systemic review suggests that clinically symptomatic plaques have a lower degree of calcifications than asymptomatic plaques (Kwee, 2010). The percentage calcification within a plaque of a stenosed artery, rather than the absolute volume seems to be associated with plaque stability (Nandalur *et al.*, 2007). This underscores why the (automated) quantification of the relative contribution of the plaque components might add to the improvement of stroke risk prediction.

The MDCTA plaque imaging studies performed so far had a cross-sectional study design. The ability to quantify atherosclerotic features in vivo creates the potential to further explore atherosclerotic plaque development by prospective, serial in vivo imaging of the carotid plaque (Figure 2.12). Currently, a prospective serial MDCTA plaque imaging study is being performed, which investigates the temporal changes in plaque burden and plaque composition and its determinants in TIA and stroke patients.

2.5 Summary and future directions

Currently, MDCTA is a noninvasive imaging technique frequently used in clinical practice for the assessment of carotid stenosis grading and is replacing the more invasive technique of DSA. MDCTA can perfectly be combined with a native CT scan and a perfusion CT scan

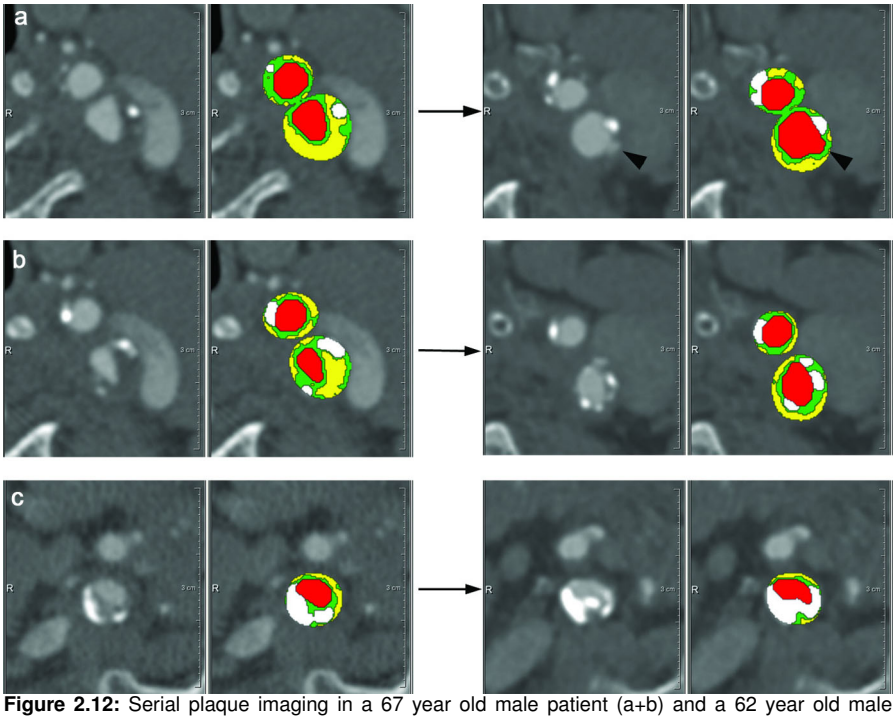

Figure 2.12: Serial plaque imaging in a 67 year old male patient (a+b) and a 62 year old male patient (c). On the left, axial MDCTA images and the plaque color overlays of the baseline scan and on the right the corresponding images of the follow-up scan. (a) Predominantly non-calcified plaque at a level just above the bifurcation. At follow-up imaging after 6 years an ulceration is visible (arrowhead). (b) Images from the same artery at a more distal site. (a+b) At follow-up imaging a decrease in plaque volume and a change in plaque composition is demonstrated. (c) Internal carotid artery demonstrating an increase in calcification of the vessel wall at follow-up (after 6 years).

of the brain in the evaluation of stroke patients.

Although plaque imaging is currently only used in research settings, the same MDCTA data set might provide further clinically important information on the atherosclerotic plaque burden, plaque surface morphology, and plaque composition for a more individualized risk prediction. Large, prospective studies demonstrating significant associations between CTA-based risk factors and (recurrent) events are yet lacking. Future research should focus on the role of plaque measures in stroke risk prediction and on the use of MDCTA-based quantified plaque measurements in monitoring efficacy of medical therapy. Large -preferably multicenter-studies should pay attention to the standardization of data acquisition and postprocessing across centers and imaging time points, since several technical parameters highly influence quantification of plaque features as is broadly depicted in this chapter. More effort should further be put in the development of robust, accurate, automated quantification of plaque measures in order to minimize measurement variability.

Chapter 3

Evaluation framework for carotid bifurcation lumen segmentation and stenosis grading

Based on:

K. Hameeteman, M.A. Zuluaga, M. Freiman, L. Joskowicz, O. Cuisenaire, L. Flórez Valencia, M.A. Gülsün, K. Krissian, J. Mille, W.C.K. Wong, M. Orkisz, H. Tek, M. Hernández Hoyos, F. Benmansour, A.C.S. Chung, S. Rozie, M. van Gils, L. van den Borne, J. Sosna, P. Berman, N. Cohen, P.C. Douek, I. Sánchez, M. Aissat, M. Schaap, C.T. Metz, G.P. Krestin, A. van der Lugt, W.J. Niessen, T. van Walsum, Evaluation framework for carotid bifurcation lumen segmentation and stenosis grading, *Medical Image Analysis*, 15(4):477-488, 2011.

3.1 Introduction

Cardiovascular diseases account for 30% of all deaths worldwide (Abegunde *et al.*, 2005). Atherosclerosis, a disease of the vessel wall, is the major cause of cardiovascular diseases such as stroke (Frostegård, 2005). Atherosclerosis may lead to stenosis (luminal narrowing), but it is also possible for atherosclerotic plaque to build up without narrowing the lumen. (Glagov *et al.*, 1987) Cardiovascular imaging is an important means to monitor and quantify the state of the vessel wall and lumen.

Manual lumen segmentation and stenosis quantification is laborious and suffers from inter and intra rater variabilities (Scherl *et al.*, 2007). Consequently much work has been performed on (semi)-automated cardiovascular image processing, of which the majority focuses on lumen quantification and assessment of the severity of luminal stenosis in various imaging modalities.

In 2004, Kirbas and Quek (2004) published a review paper on vessel lumen segmentation algorithms. More recently, an extensive review paper on the same subject was published by Lesage *et al.* (2009). Both papers provide an overview of the currently published vessel segmentation methods, categorized according to the technology (Kirbas and Quek, 2004) or the combination of method characteristics such as the used vessel models, image features and extraction schemes (Lesage *et al.*, 2009). However, as explicitly indicated by Lesage *et al.* (2009), direct performance comparisons of different approaches are lacking because of the wide range of applications, and more generally, because of the lack of standard image databases and validation criteria for most vascular segmentation applications. Moreover, many of the reviewed algorithms are not publicly available which hampers an objective and fair comparison by third parties.

The goal of the framework described in this chapter is to provide a standardized evaluation framework for carotid artery lumen segmentation and stenosis grading in Computed Tomography Angiography (CTA). We focus on the carotid bifurcation (Figure 3.1), where the Common Carotid Artery (CCA) splits into the External Carotid Artery (ECA) and Internal Carotid Artery (ICA). The latter is one of the major blood supplying arteries to the brain. In 25% of all stroke patients, the stroke is caused by atherosclerotic disease in the carotid artery bifurcation. As shown by the North American Symptomatic Carotid Endarterectomy Trial (NASCET Collaborators, 1991) and the European Carotid Surgery Trial (ECST Collaborators, 1998) the stenosis grade is an important clinical measure in deciding whether or not to perform carotid endarterectomy (surgical procedure to remove the atherosclerotic plaque from the vessel). Carotid endarterectomy is indicated in case of a stenosis of 50-99% (Rothwell *et al.*, 2003). So the accuracy of stenosis analysis influences clinical decision making. Traditionally stenoses around the carotid bifurcation have been assessed with intra-arterial catheter angiography, *i.e.* Digital Subtraction Angiography (DSA), which is still considered the gold standard. DSA has a 0.3-1% risk of neurological deficits such as stroke (Waugh and Sacharias, 1992; Hankey *et al.*, 1990b) which makes the use of less invasive diagnostic imaging preferable. CTA is a good, less invasive alternative to DSA for the assessment of stenosis in the carotid bifurcation (Binaghi *et al.*, 2001; Koelemay *et al.*, 2004).

Besides the assessment of the stenosis caused by atherosclerotic plaque, imaging also allows for the evaluation of the atherosclerotic plaque itself. Much research is currently focused on the question whether specific plaque features like composition or morphology are associated with an increased risk for clinical events. However, in current practice the degree of stenosis is still the only biomarker which influences clinical decision making.

Besides CTA, MRI and US are able to visualize the plaque. Currently it is not clear which technique is most suitable in providing clinical useful information on both stenosis and the atherosclerotic plaque.

Our choice for lumen segmentation of the carotid bifurcation is motivated by the clinical relevance of this structure. Additionally, the carotid is a medium sized vessel which makes it suitable as a test case for a wide range of vessel segmentation algorithms, while still having the typical challenges in segmenting diseased vessels, such as calcifications and severe stenosis. Also the presence of a bifurcation and nearby bone and veins imposes additional challenges on the segmentation. Moreover, lumen segmentation is a first step in the assessment of stenosis, which is the clinical relevant parameter that is assessed in the CLS2009 framework.

The remainder of this chapter is organized as follows: in Section 3.2 previous work is discussed, followed in Section 3.3 by a description of the CLS2009 framework for the segmentation of the carotid artery lumen and its stenosis grading. Section 3.4 gives a description of the first use of the framework during the MICCAI workshop, including a short description of the methods that were tested and the results of these methods as produced by the framework. This is followed by some concluding remarks in Section 3.5.

3.2 Previous work

There is a growing number of initiatives that set up a publicly available data repository and standardized evaluation framework. This demonstrates an increasing interest in standardized evaluation and the possibility to compare methods to each other. In this section we give a few examples and we briefly discuss some published lumen segmentations and stenosis grading methods.

In the field of computer vision the following frameworks can be used: the Range Image Segmentation Comparison (Hoover *et al.*, 1996), the Retrospective Image Registration Evaluation Project (West *et al.*, 1997), the Berkeley Segmentation Dataset and Benchmark (Martin *et al.*, 2001), and the Middlebury Stereo Vision evaluation (Scharstein and Szeliski, 2002).

Several workshops involving the setup of an evaluation framework in the field of medical imaging, have been organized at the MICCAI and SPIE conferences. Reports on some of these frameworks have appeared recently (Heimann *et al.*, 2009; Schaap *et al.*, 2009; Niemeijer *et al.*, 2010; Ginneken *et al.*, 2010). More initiatives can be found at the website http://www.grand-challenge.org.

The carotid bifurcation segmentation and stenosis grading framework in CTA images (CLS2009 framework) was initially presented at the *3D Segmentation in the Clinic: A Grand*

Challenge III workshop during the MICCAI 2009 conference in London. There are two challenges that are related to CLS2009: the Rotterdam Coronary Artery Algorithm Evaluation Framework which does not address lumen segmentation, but centerline extraction and the EXACT09 framework, which compares submitted segmentations of the airways to *each other* and generates a reference standard from these submitted segmentations. In contrast to the CLS2009 framework the EXACT09 framework does not have a gold standard obtained from manual segmentations.

Some CTA vessel lumen segmentation methods have been evaluated on carotid arteries around the bifurcation (Manniesing *et al.*, 2007; Baltaxe Milwer *et al.*, 2007; Cuisenaire *et al.*, 2008). All these methods use different evaluation measures, and different data sets. Manniesing reports a Dice similarity index (Dice, 1945) of 0.77 for 14 out of 20 carotid arteries for which a path through the carotid lumen could be obtained. Algorithm parameters were trained on a separate set of 10 CTA datasets. Milwer reports a sensitivity of 0.85 and a positive predictive value of 0.80 (equivalent to a Dice similarity of 0.82) on a set of 65 2D cross-sections of 13 CTA datasets. The algorithm parameters were determined empirically. Cuisenaire performs a visual assessment on failure or success by an expert and reports a 93 % success score on extraction of six modeled head and neck vessels in 28 CTA datasets.

Results of semi-automatic stenosis grading methods for carotid arteries in CTA images have been reported by Berg *et al.* (2005), Scherl *et al.* (2007) and Wintermark *et al.* (2008b). The level of automation varies, and only Scherl gives an extensive description of the lumen segmentation and stenosis grading algorithm. Different evaluation measures are used, although they all report an agreement measure, correlation (Berg), difference (Scherl), regression and Bland Altman analysis (Wintermark), with DSA (Berg) or manual (Scherl and Wintermark) measurements. Both Scherl and Wintermark use the minimal diameter as a quantity to measure the stenosis, but neither of them explicitly defines this measure. The number of included patients for the evaluation differs widely: Berg uses 36 CTA datasets, Scherl 10, and Wintermark 125.

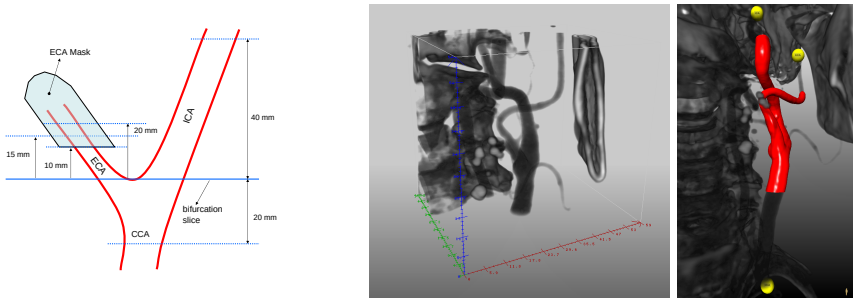

Figure 3.1: Region around carotid bifurcation: (a) schematic depiction of the region of interest; (b) a rendering of this region for one of the datasets; (c) visualization of a dataset with the three initialization points and the reference segmentation.

3.3 Evaluation framework

The CLS2009 framework comprises a publicly accessible data repository, a set of standardized evaluation measures and an online evaluation system. This section starts with a description of the segmentation tasks, followed by a description of the datasets and their acquisition protocols. Next we describe the procedure that was used to generate manual segmentations and stenosis gradings, followed by a description of the used procedure to merge the different manual segmentations into a reference standard. The section concludes with the description of the evaluation measures.

3.3.1 Lumen segmentation and stenosis grading

The evaluation framework focuses on the CCA and ICA (see Fig 3.1), the clinically most relevant parts of the carotid bifurcation. A small part of the ECA is also included, to allow evaluation of the segmentation at the location where the ECA bifurcates from the ICA.

The segmentation task focuses on the lumen of the CCA, ICA and ECA around the carotid bifurcation in a CTA dataset. The exact region of which the lumen must be segmented is defined around the bifurcation slice, which is defined as the first (caudal to cranial) slice where the lumen of the carotid artery appears as two separate lumens: the lumen of the ICA and the lumen of the ECA. The segmentation must include the CCA, starting at least 20 mm caudal of the bifurcation slice, the ICA, up to at least 40 mm cranial of the bifurcation slice, and the ECA, up to between 10 and 20 mm cranial of the bifurcation slice, see also Figure 3.1.

The performance measures are computed in the region of interest. The bifurcation slice is not revealed to the participants, who must ensure that their segmentation at least includes this region. Our definition of the bifurcation slice and the region of interest should be sufficient to determine a suitable region of interest for the segmentations.

The segmented lumen of the ECA should be cut between 10 and 20 mm cranial of the bifurcation slice. To allow for some flexibility in cutting of the ECA lumen, the region around the ECA between 10 and 20 mm cranial of the bifurcation slice is a "masked" region, where the evaluation measures are not evaluated, see also Figure 3.1a.

The lumen segmentation must be represented as a partial volume segmentation, i.e. an image where each voxel value represents the occupancy of the voxel by the vessel lumen: a value of 0 means no lumen present, and a value of 1 means fully occupied with lumen.

The second use of the CLS2009 framework is the evaluation of stenosis gradings for the ICA. Two stenosis grades must be determined for each ICA: an area-based and a diameter-based stenosis grade.

We use the following NASCET-like (NASCET Collaborators, 1991) definition for the area-based stenosis grade S_{a}:

$$S_{\mathrm{a}} = 100\% \times \left(1 - \frac{a_m}{a_r}\right) \tag{3.1}$$

where a_m is the minimal cross-sectional area along the CCA and ICA, and a_r the average cross-sectional area over a distal reference part of the ICA. For the diameter-based stenosis

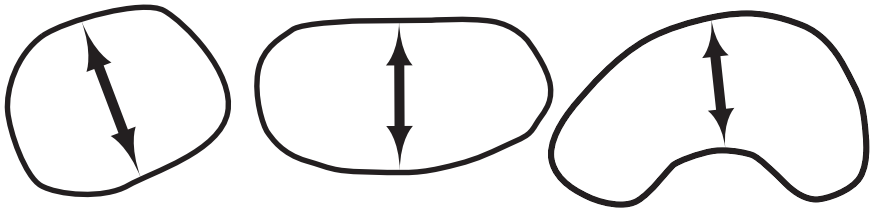

Figure 3.2: Examples of our definition of the diameter of a cross sectional contour.

grade S_{d} we similarly use:

$$S_{\mathrm{d}} = 100\% \times \left(1 - \frac{d_m}{d_r}\right) \tag{3.2}$$

where d_m and d_r are the minimal and average reference cross-sectional diameter respectively. We define the diameter of a cross-section as the shortest straight line that divides the contour in two equally-sized areas. Using this definition, the diameter of non circular or non elliptic cross sections is well defined. See Figure 3.2 for examples of the diameter for several contour shapes. The reference measure in Equation 3.1 and 3.2 should be based on a vessel section, distal to the location of the stenosis and should reflect the normal luminal diameter or area.

We distinguish two categories for the lumen segmentation and the stenosis grading task: a category for fully automatic methods, which do not require user interaction, and one for semi-automatic methods where three initialization points may be used. To eliminate dependency on these initialization points, they are incorporated in the available data repository. The image data for both tasks (lumen segmentation and stenosis grading) is the same: the CTA dataset (including header information such as voxel size and world coordinate system). The three points are located within the carotid artery proximal and distal to the above defined region of interest (see Figure 3.1c):

1. A point in the CCA, at the level of the cranial side of the thyroid gland.
2. A point in the ICA, just before the artery enters the skull base.
3. A point in the ECA, where the artery is close to the mandible.

3.3.2 CTA data

The dataset repository consists of 56 CTA datasets from three different medical centers: the Erasmus MC (Rotterdam, The Netherlands), Hôpital Louis Pradel (Bron, France) and the Hadassah Hebrew University Medical Centre (Jerusalem, Israel). All datasets were routinely acquired CTA datasets of the carotid bifurcation. The medical center in which a dataset was acquired is made known to the participants. Example slices of the datasets from the three research centers are shown in Figure 3.3.

Stenosis category	Stenosis degree (%)	Number of datsets
0	0	12
1	0–30	10
2	30–50	6
3	50–70	10
4	70–99	18

Table 3.1: Distribution of the datasets over the 5 stenosis categories based on the reference standard.

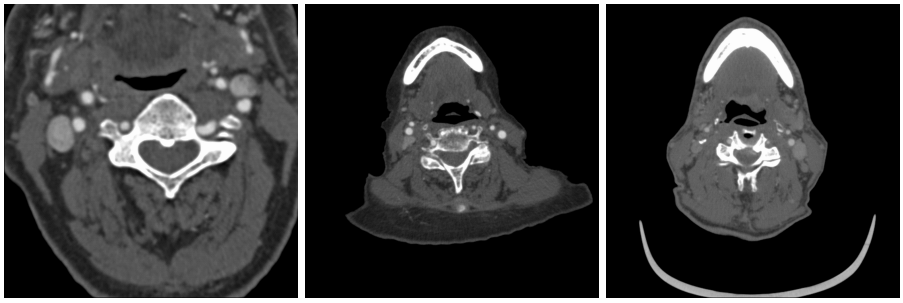

Figure 3.3: Examples of a slice of the CTA datasets. From left to right a slice from Erasmus MC, the Hadassah Hebrew University Medical Centre and Hôpital Louis Pradel.

The datasets were selected such that they contain a large range of stenosis degrees and all stenosis categories (as listed in Table 3.1) contained an equal number of datasets. The initial stenosis degrees were determined by visual inspection. Creating the reference standard and measuring the stenosis based on lumen area slightly changed this distribution. The distribution, based on the measurements from the reference standard, is shown in Table 3.1.

The details of the scanning protocols for each of the medical centers are provided below. The CTA scanning parameters are summarized in Table 3.2.

Erasmus MC protocol

The CTA data from Erasmus MC was acquired on a 16-row CT scanner (Sensation 16 - Siemens Medical Solutions, Forchheim, Germany) with a standard scan protocol using the following parameters: 120 kV, 180 mAs, collimation 16×0.75 mm, table feed per rotation 12 mm, pitch 1.0, rotation time 0.5 seconds and scan time 10–14 seconds. The CTA scan range is from the ascending aorta to the intra cranial circulation (2 cm above the sella turcica). All patients received 80 ml contrast material (Iodixanol 320 mg/ml, Visipaque Amersham Health, Little Chalfont, UK), followed by 40 ml saline bolus chaser, both with an injection rate of 4 ml/sec. Synchronization between the passage of contrast material and data acquisition was achieved by real time bolus tracking at the level of the ascending aorta. The trigger threshold was set at

	EMC	Hd	LP
Scanner	Sensation 16	Brilliance 64	Brilliance 64
In plane voxels	512×512	512×512	512×512
Slices	395–579	750	636–827
Pixel size (mm)	0.23–0.26	0.55	0.414–0.547
Z-spacing (mm)	0.6	0.5	0.45
Slice thick.	1	1	0.9
Kernel	B30f	B	B

Table 3.2: Overview of scanning parameters of CTA datasets, EMC = Erasmus MC, Hd = Hadassah, LP = Louis Pradel.

an increase in attenuation of 75 Hounsfield Units (HU) above baseline attenuation (approximately 150 HU in absolute value). Image reconstructions were made with in-plane pixel sizes of 0.23–0.26×0.23–0.26 mm^2, matrix size of 512×512 (real in-plane resolution 0.6×0.6 mm), slice thickness of 1.0 mm, increment of 0.6 mm and with an intermediate reconstruction kernel (B30f).

Hadassah protocol

The CTA data from the Hadassah Hebrew University Medical Centre was acquired on a 64-row CT scanner (Brilliance 64 – Philips Healthcare, Cleveland OH) with a standard scan protocol using the following parameters: 120 kV, 251 mAs, collimation 64×0.625 mm, pitch 1.20, rotation time 0.75 seconds and scan time 7.30 seconds. The CTA scan range was from the ascending aorta to the intra cranial circulation (2 cm above the sella turcica). All patients received 75 ml contrast material (Iopamiro, Bracco Diagnostics, Milano Italy), with an injection rate of 3.5 ml/sec. Image reconstructions were made with in-plane pixel sizes of 0.55×0.55 mm^2, matrix size of 512×512, slice thickness of 1.0 mm, increment of 0.5 mm and with an intermediate reconstruction kernel (B).

Louis Pradel protocol

The CTA data of Hôpital Louis Pradel was acquired on a 64-row CT scanner (Brilliance 64 – Philips Healthcare, Cleveland OH) with a standard scan protocol using the following parameters: 120 kV, 300 mAs, collimation 52×1.5 mm, rotation time 0.35 seconds and scan time 10–14 seconds. The CTA scan range was from ascending aorta to the intra cranial circulation (2 cm above the sella turcica). All patients received 80 ml contrast material (Iomeron 4000 mg/ml, BRACCO, Milano, Italy) followed by 40 ml saline bolus chaser, both with an injection rate of 4 ml/sec. Synchronization between the passage of contrast material and data acquisition was achieved by real time bolus tracking at the level of the ascending aorta. The trigger threshold was set at an increase in attenuation of 75 HU above baseline attenuation. Image reconstructions were made with in-plane pixel sizes of 0.414–0.547×0.45 mm^2, matrix size of 512×512 (real in-plane resolution 0.6×0.6 mm), slice thickness of 0.9 mm, increment

Center	Training	Testing	Total
Erasmus MC	9	27	36
Hadassah	3	7	10
Louis Pradel	3	7	10
Total (#)	15	41	56

Table 3.3: Datasets per center, and distribution over training and testing sets.

of 0.45 mm with an intermediate reconstruction kernel (B).

Datasets for training and testing

Fifteen of the 56 datasets are made available for training. The reference standard for these training datasets is also available for download. The training datasets were chosen such that they were equally distributed over the five stenosis categories. The reference standard of the remaining 41 datasets is not made available for download. These datasets are used for testing the performance of the algorithms. The distribution of the number of datasets over the training and testing sets and over the different centers is shown in Table 3.3.

3.3.3 Reference standard

The reference standard was created by averaging three manual segmentations of the lumen in the CTA datasets. This section describes the manual annotation process, the creation of a partial volume representation from each observers' annotations and the averaging of the observers' segmentations to obtain the reference standard.

Manual annotations

Three different observers annotated the carotid lumen boundary and graded the stenosis in the ICA for each data set. Each contributing center performed the annotations on the data it provided, thus the three observers for each of the three centers were different and there were nine observers in total.

The manual annotations for the lumen segmentation and stenosis grading were performed with a custom made tool, based on MeVisLab (MeVis Research, Bremen, Germany). The annotation procedure was as follows:

1. The bifurcation point was identified and manually selected

2. Positions along the centerlines for both the ICA and ECA were clicked, starting in the CCA, 20 mm caudal of the bifurcation slice, and extending to 40 mm cranial of the bifurcation slice for the ICA and 20 mm cranial of the bifurcation slice for the ECA. This way two centerlines were defined: CCA-ICA and CCA-ECA. The part in the CCA thus was annotated twice.

3. Resampled centerlines were used to generate Curved Multi Planar Reformatted images (CMPRs), in which longitudinal contours were drawn for three different orientations (each 60^o apart) of the CMPRs. Figure 3.4 shows an example of one of the three orientations with two longitudinal contours.

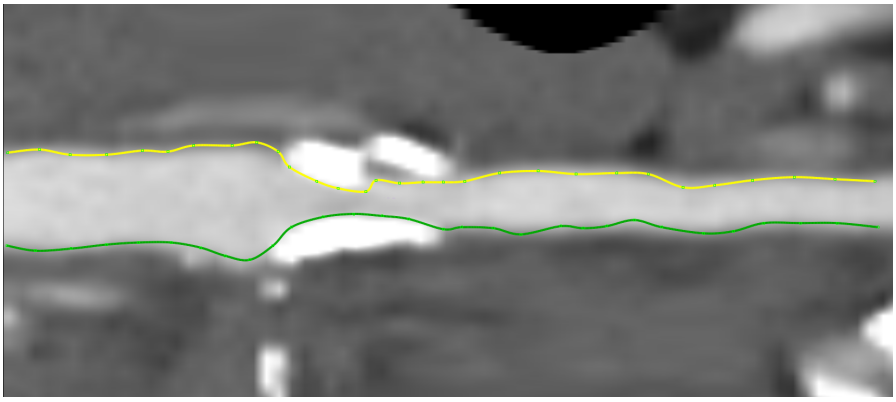

Figure 3.4: Example of two longitudinal contours drawn on a CMPR image.

4. Cross-sectional contours orthogonal to the centerline were created at 1 mm intervals along the centerline. These contours were created by fitting a Catmull-Rom spline (Catmull and Rom, 1974) through the (six) positions where the cross-sectional plane intersects the longitudinal contours. Figure 3.5 shows a visualization of a subset of these contours together with the longitudinal contours, the centerline and a cross-sectional image plane that is perpendicular to the centerline. The longitudinal contours of Figure 3.4 and 3.5 are the same.

   The contours were edited and updated if they did not match the luminal boundaries.

The contours were drawn on a display with fixed window level settings (center = 176 HU, width = 800 HU).

Observers' contours processing

The contours of each observer were separately processed to obtain the partial volume segmentations (see Figure 3.6):

1. The contours (both for the ICA and the ECA) were converted to partial volume segmentations, using a Thin Plate Spline interpolation between the contour points (Turk and O'Brien, 1999).

2. Signed distance maps (both for the ICA and the ECA) were generated from the partial volume segmentations of the ICA and ECA.

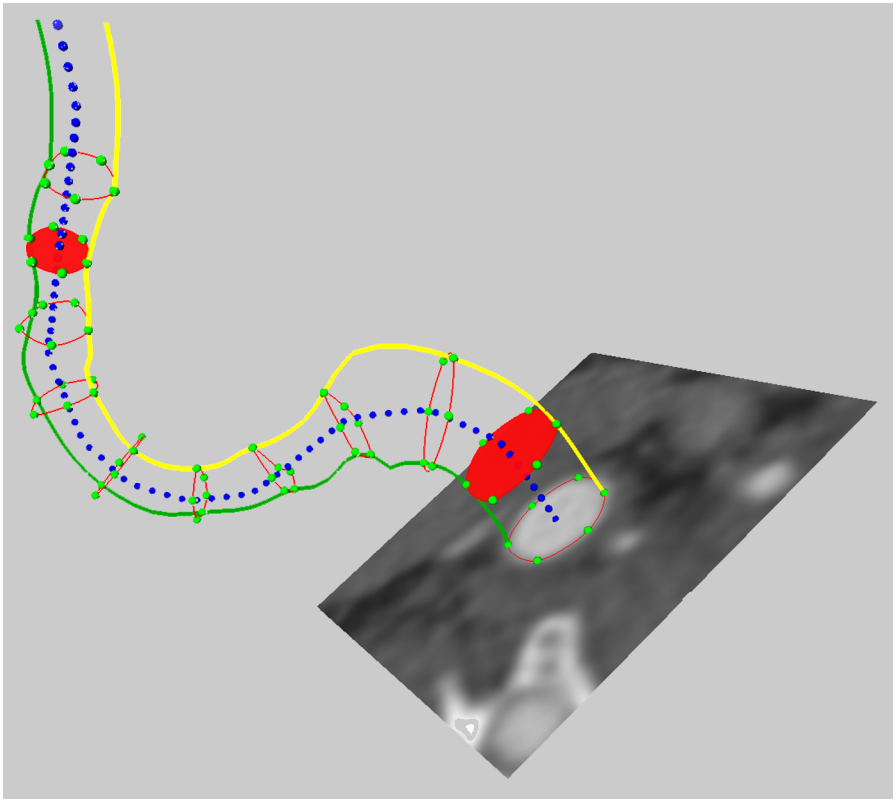

Figure 3.5: Example of two longitudinal contours (which correspond to the ones shown in Figure 3.4) with cross-sectional contours that are spline interpolations of the six intersection points (light dots) of longitudinal contours with the plane (shown image plane) that is perpendicular to the centerline (dark dots between the two longitudinal contours).

3. The ICA and ECA signed distance maps were combined, where the resulting value was the signed minimum absolute value if both distances had the same sign and the minimum value if the distances differed in sign. Thus a voxel that is inside the vessel in either the ICA or the ECA segmentation is also part of the vessel in the combined segmentation and a voxel outside the vessel in both segmentations will get the minimum distance of both distance maps. The result is a signed distance map for the complete bifurcation.

4. The partial volume (pv) segmentations of the ICA and ECA were also combined by taking the voxel-wise maximum to obtain the partial volume segmentation of the bifurcation. In this way we effectively combine the two parts, since at least the maximum of both pv segmentations is part of the combined segmentation. This partial volume

segmentation is used to rate the observer in the same way as the contestants' segmentations.

All signed distance maps used world distances in mm.

Combining observers' lumen segmentations

The three segmentations of the observers were used to generate the data of the reference standard: bifurcation slice number, evaluation region of interest and the lumen segmentation.

The bifurcation slice was computed by averaging the locations, as indicated by the observers. This slice, and the bounding boxes of the contours, were used to determine the region of interest for the evaluation.

The region of interest was the bounding box of the contours, extended with 15 mm both in x- and in y-direction. The z-range was determined from the reference bifurcation slice, and ranged from 20 mm caudal of the bifurcation slice to 40 mm cranial of the bifurcation slice.

The lumen segmentation of the reference standard contains three representations: a signed distance map, a surface representation and a partial volume segmentation. It also contains the mask for the distal part of the ECA. These lumen representations and the mask were constructed in the following way:

1. The signed distance map was obtained by averaging the observers' signed distance maps, and subsequently performing a signed distance transform on the zero-level set.

2. The surface representation was obtained by determining the isosurface at zero of the reference signed distance map, obtained in the previous step.

3. The partial volume representation was generated from the reference standard signed distance map by interpolating the distance map on super-resolution, and determining the fraction of subvoxels that have a negative distance (*i.e.* that were inside the lumen).

4. For the separate branches of the ICA and ECA average distances maps of the three observers were created. These average maps of the two separate branches were used to create the mask of the distal part of the ECA. This mask contains all voxels that satisfied each of the following three criteria:

    - the voxel is in the 10–20 mm range cranial of the bifurcation, and
    - the ECA signed distance map value of the voxel is less than 2 mm, *i.e.* the voxel is inside or close to the ECA, and
    - the ECA signed distance map value is less than the ICA signed distance map value, *i.e.* the voxel is closer to the ECA than to the ICA.

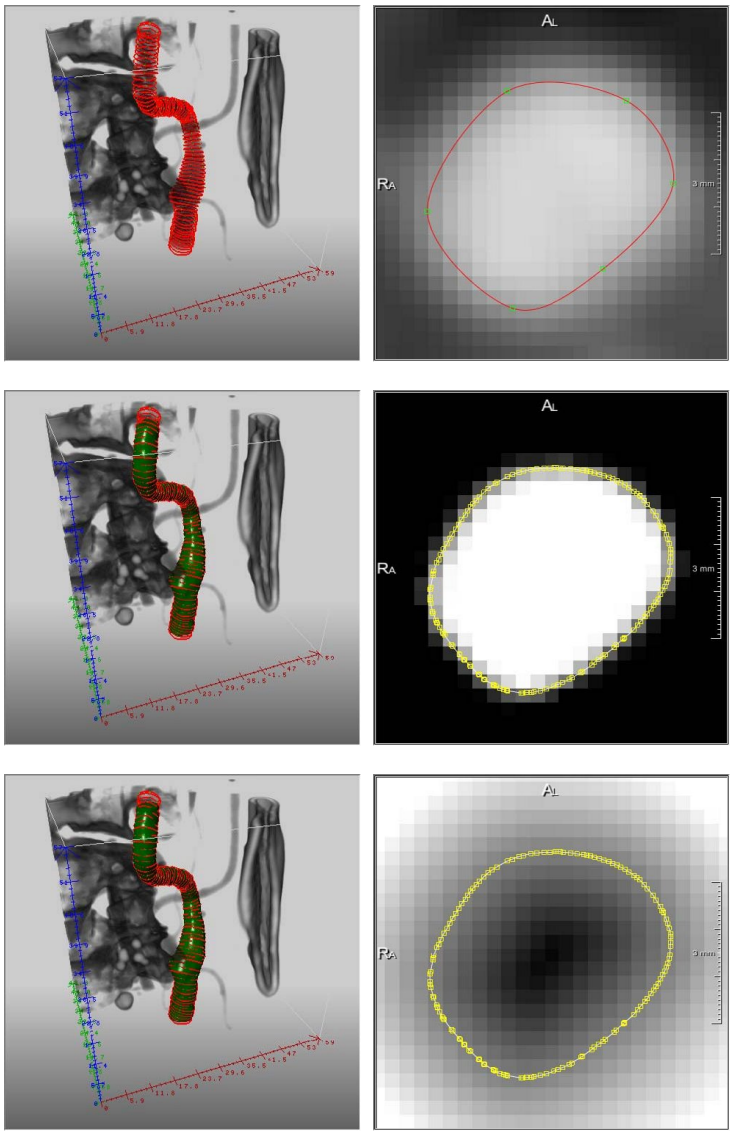

Figure 3.6: Processing of observer annotations, left column shows a 3D visualization and right column a 2D visualization. From top to bottom: initial contours, partial volume from contours (left: isosurface at 0.5) and signed distance map from partial volume (left: isosurface at 0.0).

Stenosis values

The ICA and CCA contours were used for stenosis grading. The ECA contours were not used as atherosclerosis and luminal stenosis in this artery is of less clinical relevance. Graphs of the contour area and diameter (see Section 3.3.1) along the centerline were created, based on the corrected cross-sectional contours.

In the graphs, the longitudinal position of the minimal area or diameter could be selected, after which a default reference segment was shown 20 mm distal to the selected stenosis and 10 mm in length. The position and length of the reference segment could be manually edited, subject to the constraint that the reference area should remain distal of the minimal area location, and should not extend outside the segmented region, i.e. beyond 40 mm cranial of the bifurcation slice. The stenosis grade was determined using the values from these graphs. The three observer values for the stenosis were averaged to obtain the reference standard stenosis values.

Initialisation points

The three initialization points for the semi-automatic methods (see Section 3.3.1) were annotated by one of the observers.

3.3.4 Evaluation measures and ranking

Lumen segmentation

The partial volume lumen segmentations as supplied by a participant are evaluated using the following three performance measures[1]:

- The Dice similarity index D_{si}:

$$D_{\text{si}} = \frac{2 \times \left|\text{pv}_r \cap \text{pv}_p\right|}{\left|\text{pv}_r\right| + \left|\text{pv}_p\right|} \tag{3.3}$$

  where pv_r and pv_p are the reference and a participant's partial volumes respectively, the intersection operation is the voxel-wise minimum operation, and $|.|$ is the volume, *i.e.* the integration of the voxel values over the complete image.

- The mean surface distance D_{msd}:

$$D_{\text{msd}} = \frac{1}{2} \times \left(\frac{\int_{S_r} \left|\text{sdm}_p\right| \, ds}{A_r} + \frac{\int_{S_p} \left|\text{sdm}_r\right| \, ds}{A_p} \right) \tag{3.4}$$

  where $\left|\text{sdm}_p\right|$ and $\left|\text{sdm}_r\right|$ are the absolute signed distance maps of the reference and a participant's segmentation respectively, S_r and S_p are the lumen boundary surfaces

[1] We used a fourth measure at the MICCAI Workshop: the root mean squared distance, which is in between the other two distance measures. We decided to remove this fourth measure, as it did not add valuable information.

(isosurfaces of the signed distance map at the value 0) and A_i is the surface area of surface S_i, *i.e.* $A_i = \int_{S_i} ds$.

- The Hausdorff[2] distance D_{hd}:

$$D_{hd} = \max\left(\max_{x \in S_r} \left|sdm_p(x)\right|, \max_{x \in S_p} \left|sdm_r(x)\right|\right) \tag{3.5}$$

Both distance measures are symmetric, and all measures are only evaluated in the region of interest that is specified in Section 3.3.1.

Stenosis grading

The stenosis grade error is defined as the absolute difference between the reference standard value and the value determined by a participant. Because revealing the (exact) error per dataset also reveals the reference stenosis grades, the stenosis errors are not communicated per dataset, but only per ensemble (training or testing). Providing the ranking per dataset may potentially be used to determine the reference values by using multiple submissions. Hence we also do not show the stenosis ranking per dataset. The final ranking, however, is determined by averaging the (hidden) errors per dataset and stenosis grade (diameter and area).

Stenosis grading is often performed after a lumen segmentation is obtained. Thus, we developed a simple standard stenosis grading algorithm and applied it to all segmentation results. The algorithm takes the partial volume lumen segmentation of the participants as input and determines the desired stenosis measure. The algorithm first determines the vessel surface. Based on this surface a center line is created using the vmtk package (Antiga and Steinman, 2004). Along this centerline the vessel surface is cut at 1 mm intervals with a plane perpendicular to the centerline using the default vtkCutter class (Schroeder *et al.*, 2006). The intersection points are then used to calculate the cross-sectional area and minimal diameter of the vessel along the centerline. The resulting area and diameter curves are smoothed using a Gaussian kernel with $\sigma = 3$mm. The minimal value of these smoothed curves is found, which is defined as the location of the stenosis. Using the found position, the degree of stenosis is then determined from the un-smoothed curve using both the minimum value and the average value of the reference area which is defined as 2 cm distal to the bifurcation and 1 cm long.

The stenosis values of this standard algorithm are determined for each submission where there is a successful lumen submission, but are not used in ranking the stenosis submissions.

Ranking

The evaluation measures lead to one performance value for each participant, for each dataset and for each evaluation measure. Per dataset and per evaluation measure a ranking of the

[2]During the workshop we used the average instead of the maximum of the two maximum surface distances. The Hausdorff distance gives similar rankings, but is considered to be more informative.

participants is made, by ordering them from best to worst and giving a rank according to their position in the list: 1 for the best submission and P for the worst (with P the number of participants). If there are no results for a participant for a certain dataset the ranks for all evaluation measures for that dataset are set to the highest value (P).

In this way, we obtain $N \times M$ rankings (for N datasets and M measures, with $N = 41$ for testing, $M = 3$ for lumen segmentation and $M = 2$ for stenosis grading). The overall ranking for a participant is obtained by averaging the ranks of all these $N \times M$ rankings.

We also report the average values of the evaluation measures per participant. The values of evaluation measures for missing or failed datasets are not taken into account in this averaging, so these values represent the results for the datasets that were successfully processed. We also report the number of datasets on which a method was successful.

Availability of the framework

The evaluation framework is publicly available through the website: http://cls2009.bigr.nl. All CTA datasets, the reference standard for the training set as well as binaries and source code of the evaluation software can be downloaded from this website. This software is the same as which is used by the framework to evaluate the submitted results with the testing data. Participants can use it together with the training set reference standard to determine the evaluation measures without using the website. The framework provides the possibility to submit results. The evaluation measures will be determined for submitted results and, after confirmation by the registrant, included in the ranking of all the methods. The website also provides the possibility to create custom queries on the datasets based on the research center and stenosis grading.

3.4 MICCAI workshop

The evaluation framework was used in a competition setup at the MICCAI 2009 workshop *3D Segmentation in the Clinic: A Grand Challenge III*. Around 100 groups from academia and industry were invited by e-mail to participate in the workshop. Thirty-one teams registered at the website, 21 of which sent in the data confidentiality form, which was required to download the data, 13 teams downloaded the data and 9 teams submitted results. For the lumen segmentation, there was one submission from a commercial company, which did not participate in the workshop. Eight teams participated in the category for semi-automatic methods and one team submitted results of a fully automatic method. Only three teams submitted results for the stenosis grading, none of these methods were fully automatic.

The set of testing CTA datasets was divided in two parts for the workshop: a set to be processed prior to the workshop (31 datasets), and an on-site set to be processed by the participants during the morning session of the workshop (10 datasets). The results presented here are the aggregate results over all 41 datasets of the test set. Each team had the opportunity to resend a submission after the workshop to eliminate practical problems (e.g. erroneous file format submissions) during the on-site competition.

3.4.1 Evaluated algorithms

Below we provide a very brief description of the algorithms involved in the MICCAI workshop challenge. For a more extensive description we refer to the respective papers that are available through the workshop issue of the Midas Journal (Hameeteman *et al.*, 2009a,b).

Krissian and Arencibia-García

The algorithm by Krissian and Arencibia-García (2009) is divided into two main steps: first, two minimal cost paths are tracked between the CCA and both the ECA and the ICA. The cost functions are based on a multi-scale vesselness response. Second, after detecting the junction position and cutting or extending the paths based on the requested lengths, a level set segmentation is initialized as a thin tube around the computed paths and evolves until reaching the vessel wall or a maximal evolution time.

Freiman *et al.*

The algorithm by Freiman *et al.* (2009) uses a two-phase graph-based energy minimization approach. Its inputs are start and end seed points inside the vessel. The two-step graph-based energy minimization method starts by computing the weighted shortest path between the vessel seed endpoints based on local image and seed intensities and vessel path geometric characteristics. It then automatically defines a region of interest from the shortest path and the estimated vessel radius, and extracts the vessels boundaries by minimizing the energy on a corresponding graph cut.

Zuluaga *et al.*

The algorithm by Zuluaga *et al.* (2009) consists of two stages: intensity-based preprocessing and model-based lumen delineation. The intensity-based preprocessing contains denoising by a Dual Tree Complex Wavelet Transform filter (Doré and Cheriet, 2009), pre-segmentation using typical HU ranges refined by a Fuzzy C-means classifier, enhancement using gradient magnitudes and an exponential function within the pre-segmented regions. The model-based delineation extracts one centerline per seed-point by use of an elastic model and multi-scale eigen-analysis of the inertia matrix (Orkisz *et al.*, 2008), which is followed by a distance-based identification of the bifurcation and surface pruning along the centerlines.

Wong *et al.*

The algorithm by Wong *et al.* (2009) first generates a rough centerline using a vesselness measure and Minimal Cost Path search. This centerline is then simplified and used as initialization of an algorithm to find the principal curve (Kégl *et al.*, 2000). This algorithm uses a 1D intensity model and results in a centerline with associated vessel radii. By assuming circular lumen cross-sections, both the segmentation and stenosis grading can then be determined.

Cuisenaire

The algorithm by Cuisenaire (2009) is a fully automated method that segments not only the carotid bifurcation but also the vessels from the aortic arch to the circle of Willis (COW), as well as the external branch and the vertebral arteries (Cuisenaire *et al.*, 2008). The centerline of each vessel is first extracted using a local adaptive fast marching algorithm that is both seeded and constrained by an anatomical model. These constraints are adapted to the individual patient using both registration of the brain and segmentation of the brain and spine. Seeds are automatically placed in the COW and the lower part of the neck. The vessel lumen is segmented using 3D active objects initialized as a tube around the centerline.

Florez Valencia *et al.*

In the algorithm of Flórez Valencia *et al.* (2009) the lumen is modeled by right generalized cylinders (RGC) with piece-wise constant parameters (Azencot and Orkisz, 2003). Their parameters are identified from planar contours extracted along the minimal paths between the end-points. The contours are extracted by use of 2D Fast Marching. Identification of the parameters (observations) is based on a geometrical analogy with piece-wise helical curves (axis) and on Fourier series decomposition of the contours (surface). Consistency from one piece to another is managed by a Kalman optimal estimator (Flórez Valencia *et al.*, 2006).

Gülsün and Tek

The algorithm by Gülsün and Tek (2009) uses graph-cuts optimization technique together with centerline models for segmenting the carotid arteries. It first detects the centerline representations between user placed seed points. This centerline extraction algorithm is based on a minimal path detection method which operates on a medialness map. The lumen of carotid arteries is then extracted by a graph-cut optimization technique using the detected centerlines as input.

Mille *et al.*

The algorithm by Mille *et al.* (2009) is based on an extension of the minimal path method that models the vessel as a centerline and boundary. This is done by adding one dimension for the local radius around the centerline. The crucial step is the definition of the local metrics to minimize. The tubular structure of the vessels is exploited by designing an anisotropic metric. This metric is well oriented along the direction of the vessel, admits higher velocity on the centerline, and provides a good estimate of the vessel radius. In order to deal with carotid stenosis or occlusions, the segmentation is refined using a region-based level set method derived from the Chan-Vese model (Chan and Vese, 2001).

3.4.2 Workshop results

Table 3.4 shows the average results and ranking for all lumen evaluation measures, for both the automatic and semi-automatic algorithms. The 'Total success' column shows the number of datasets over which the average values were calculated (see Section 3.3.4). The only fully

Method	Total	Dice		Msd		Hausdorff		Processing	Total
name	success	%	rank	mm	rank	mm	rank	time	rank
Observer A	41	95.1	2.61	0.10	2.68	0.65	2.73	–	2.67
Observer B	41	94.6	3.34	0.11	3.37	0.83	3.07	–	3.26
Observer C	41	94.4	3.46	0.12	3.32	0.97	3.85	–	3.54
M.A. Gülsün and H. Tek	41	91.8	5.95	0.18	5.68	1.5	5.27	50 s.	5.63
K. Krissian *et al.*	41	87.3	6.05	0.54	7.02	4.4	6.83	15 min.	6.63
O. Cuisenaire	33	89.6	8.05	0.17	6.90	1.7	7.00	1-2 min.	7.32
J. Mille *et al.*	41	83.5	8.66	0.74	8.68	10	8.90	90 sec.	8.75
M. Freiman *et al.*	41	82.9	8.85	0.75	9.05	9.2	8.90	2 min.	8.94
W.C.K. Wong *et al.*	41	77.5	9.34	1.1	9.73	11	9.07	90 sec.	9.38
M.A. Zuluaga *et al.*	41	80.9	9.63	0.82	9.68	10	9.07	4 min.	9.46
L. Florez Valencia *et al.*	37	53.6	11.1	3.4	10.9	12	10.2	2 min.	10.7

Table 3.4: Lumen segmentation performance of all submissions. The average value and rank is shown for each of the three similarity measures as defined in Section 3.3.4. The algorithm by Cuisenaire (in **bold**) is the only automatic method.

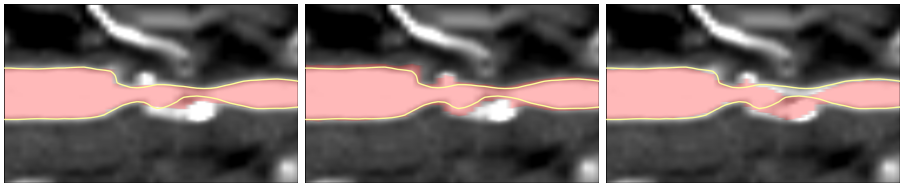

(a) (b) (c)

Figure 3.7: Visual impression of reference standard (light line) and user segmentations (shaded area) with different Dice measures: (a) 94.5, example from M.A. Gülsün and H. Tek, (b) 88.4, example from O. Cuisenaire and (c) 88.1, example from L. Florez Valencia *et al*.

Observer	AB	BC	CA	Average
Dice	0.92	0.91	0.91	0.92
Msd	0.18	0.20	0.19	0.19
Hausdorff	1.23	1.39	1.41	1.34

Table 3.5: Lumen measure of the three observers with respect to each other.

automatic method submitted by Cuisenaire has similar distance and Dice measures as the team of Gülsün and Tek, but because it is only successful in 33 of the 41 datasets (the automatic method to find the bifurcation apparently did not work in eight of the cases) it is ranked lower than the team of Gülsün and Tek and the team of Krissian and Arencibia-García.

The table also contains the results of the observers, which have been scored in the same ways as the other participants. Observer A is the overall best observer (for each of the three clinical sites), Observer C is the overall worst observer, and Observer B is the remaining observer.

Figure 3.7 gives a visual impression of the relation between the Dice measure and the segmentation quality. The figure shows a CMPR image of a region around a calcified bifurcation overlaid with three different segmentations. The Dice measures are calculated over the whole evaluation region and not just at the shown region.

We also determined the overlap and distance measures of the three observers with respect to each other. Together with their averages, which is the inter-observer variability, they are shown in Table 3.5. To make these inter-observer measures better comparable to the results of the participants, we only determined them on the test data.

These results show that protocolized manual carotid artery lumen segmentation in CTA can be performed with an average precision of around 0.19 mm, which is smaller than the voxel size. The Dice and Msd of the observers with respect to each other are comparable to the results of the best semi-automatic method by M.A. Gülsün and H. Tek. Only the Hausdorff distance of the last mentioned method is substantially worse. The method of Cuisenaire also shows comparable results, but this fully automatic method fails on eight cases, which makes comparison less straightforward as these may be the more difficult cases.

Method name	Stenosis Category				
	None	0-30	30-50	50-70	70-99
Observer A	2.58	2.73	2.57	2.50	2.96
Observer B	3.58	3.30	3.43	3.12	2.88
Observer C	3.62	3.63	3.19	3.88	3.33
M.A. Gülsün and H. Tek	6.08	5.90	5.09	5.62	5.33
K. Krissian *et al*.	7.46	6.03	6.38	6.29	7.12
O. Cuisenaire	7.12	6.50	6.71	8.54	7.83
J. Mille *et al*.	8.62	8.47	9.81	8.42	8.62
M. Freiman *et al*.	8.46	8.87	8.95	9.00	9.42
W.C.K. Wong *et al*.	9.50	10.2	9.52	8.75	8.79
M.A. Zuluaga *et al*.	8.62	9.83	9.57	9.46	9.75
L. Florez Valencia *et al*.	10.8	10.7	11.3	10.6	10.3

Table 3.6: The average rank of all the methods specified for the different stenosis categories.

Table 3.4 shows a substantial difference in the distance measures between the best three methods and the others. This can be explained by the fact that some of those other methods use a circular or elliptic model for the vessel cross-sectional area (Mille *et al.*, 2009; Zuluaga *et al.*, 2009; Wong *et al.*, 2009), whereas the best three methods are based on graph cut (Gülsün and Tek, 2009), level set (Krissian and Arencibia-García, 2009) and active surface (Cuisenaire, 2009) algorithms respectively and do not have such hard vessel model constraints. Since the segmented vessel contains a bifurcation, the cross-sectional area is expected to deviate from the circular model, which makes methods that use such a model less successful. The lower scores of Florez Valencia *et al*. can be explained by failures in the initialization of the fast marching contour extraction. This initialization is based on the extraction of a centerline, which is not robust enough in the presence of complex lesions.

Note that the results of Zuluaga *et al*. in Table 3.4 reveal that the procedure to calculate the ranks (as described in Section 3.3.4) makes it possible for method A to have better average measures than method B, while still having a worse average rank. If e.g. for a certain dataset the measures of all methods are approximately the same, this may lead to much higher rank for method A compared to method B although their measures do not differ much.

Table 3.6 lists the average ranking for lumen segmentation in each of the stenosis categories. It shows that the top three ranked methods perform consistently best over the various categories.

Table 3.7 shows the average stenosis results on the test set. The ranking of these methods does not change for the different stenosis categories.

The difference in stenosis grading performance between the observers and the participants is large when compared to the results of the lumen segmentation. This could be explained by the fact that the teams that participated in the stenosis grading competition have a relatively large error in the lumen segmentation. As the stenosis grades are determined

from lumen segmentations, inaccurate segmentations may lead to inaccurate stenosis grades. This is also confirmed by looking at the standard stenosis grading in relation to the lumen measures. Table 3.8 provides the correlation between the lumen measures and the standard stenosis measures and Figure 3.8 shows a scatter plot of the area based standard stenosis error and the Hausdorff distance of the used segmentation. As can be seen there is a strong correlation between the Hausdorff lumen distance and the error in both the diameter and area based stenosis measures. The correlation between the standard stenosis measures and the other lumen measures (Dice and Msd) is less strong. This can be explained by noting that both Dice and Msd are averages over the whole segmentation while a good stenosis measure requires a good segmentation on one specific location: the location of the stenosis. A large segmentation error on this location hardly influences the Dice and Msd, while it will directly influence on both the Hausdorff distance and the stenosis measures.

Note that in the standard stenosis algorithm, the orientation of the centerline determines the cross-sectional planes from which the area and minimal diameter are calculated. Thus the calculated measures highly depend on the extracted centerline. These standard centerlines are defined using the radius of the maximum inscribed sphere. Some of the submitted methods extract a centerline as an intermediate result, which may be a better centerline for stenosis measurement than the one extracted by the standard stenosis algorithm.

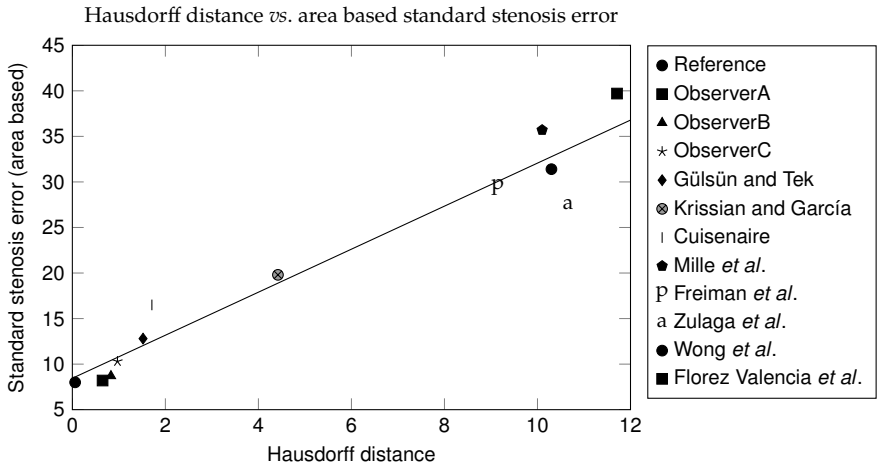

Figure 3.8: Average area based standard stenosis error with respect to the average Hausdorff distance for all methods. The line shows a linear regression fit. The Pearson correlation coefficient is 0.97.

Method name	Total success	Diameter Δ%	Diameter rank	Area Δ%	Area rank	Standard algorithm Diameter Δ%	Standard algorithm Area Δ%	Standard algorithm Lumens	Total rank
Observer A	41	3.40	2.15	2.90	2.02	*6.70*	*8.20*	*41*	2.09
Observer B	41	5.40	2.51	4.30	2.32	*9.00*	*8.70*	*41*	2.41
Observer C	41	5.70	2.66	5.00	2.68	*11.2*	*10.3*	*41*	2.67
M.A. Gülsün and H. Tek	41	—	—	—	—	*9.70*	*12.8*	*41*	—
K. Krissian *et al.*	41	—	—	—	—	*14.3*	*19.8*	*41*	—
O. Cuisenaire	33	—	—	—	—	*16.7*	*16.5*	*33*	—
J. Mille *et al.*	41	—	—	—	—	*31.2*	*35.7*	*41*	—
M. Freiman *et al.*	41	—	—	—	—	*24.5*	*29.4*	*41*	—
W.C.K. Wong *et al.*	41	31.4	4.20	25.2	4.17	*27.8*	*27.5*	*41*	4.18
M.A. Zuluaga *et al.*	41	17.0	3.56	16.9	3.71	*30.0*	*31.4*	*41*	3.63
L. Florez Valencia *et al.*	41	43.3	4.73	37.0	4.39	*36.2*	*39.7*	*37*	4.56

Table 3.7: Stenosis measures (as defined in Section 3.3.4) for all submissions. For both stenosis measures, the average difference with the reference stenosis and the rank is shown. The values in italics have been calculated with the standard stenosis grading algorithm and have not been supplied by the participants. The lumens column shows the number of lumen segmentations from which the standard values are calculated.

Stenosis measure	Dice	Msd	Hausdorff	Total rank
diam	-0.87	0.78	0.97	0.93
area	-0.87	0.79	0.97	0.92

Table 3.8: Pearson correlation coefficient between the standard stenosis measures and the lumen measures.

3.5 General discussion and conclusion

We presented an evaluation framework for carotid lumen segmentation and stenosis grading and made this framework publicly available via the website http://cls2009.bigr.nl.

The evaluation framework focuses on the effectiveness of lumen segmentation and stenosis gradings. Another important aspect for getting a novel technology accepted in daily clinical routine is efficiency. We decided not to take the computational costs into account in our framework. The main reasons are the lack of a standard performance parameter, and the variety of hardware and software platforms that is being used by the various groups participating in the challenge. Additionally, several research groups do not optimize their algorithms on computational costs, and performance estimates on current hardware and software platforms will be outdated soon because of rapid developments and increases in computational power. However, to get an indication in the computational expenses associated with the compared algorithms, we asked the current users to provide us with a rough estimate of the computational time for the processing of one dataset. Those values are listed in Table 3.4.

The framework we presented contains data from three medical centers and two different CT scanner vendors (Siemens Healthcare and Philips Healthcare), which prevents bias of the algorithms towards a specific scanner or acquisition protocol. However, other CT vendors (*e.g.* GE Healthcare, Toshiba Medical Systems) are still lacking, and thus the variety of the CTA datasets could still be improved. If other clinical centers want to contribute CTA data to our framework we will support them. From the current participants, only Wong *et al.* (2009) uses the provided scanner information to resample the image data of Erasmus MC.

Quantitative evaluation of medical imaging algorithms is essential for progress in the field of medical imaging. An objective, unbiased comparison of quantitative results is only feasible if the same evaluation measures are used, and if the datasets used in the evaluation are similar. We intend to contribute with our framework to the growing need for quantitative evaluations of medical image processing techniques. New lumen segmentation and stenosis grading algorithms can be evaluated using the described framework.

The framework proved to be an effective tool in the comparison of vessel lumen segmentation and stenosis grading techniques at the 2009 MICCAI workshop *3D Segmentation in the Clinic: A Grand Challenge III*, and is available for new evaluations of lumen segmentation and stenosis grading algorithms.

Acknowledgments

Reinhard Hameeteman, Wiro Niessen and Theo van Walsum are supported by the Stichting voor de Technische Wetenschappen (STW) of The Netherlands Organization for Scientific Research (NWO). Aad van der Lugt is supported by Netherlands Organization for Health Research and Development (NWO-KF grant 907-00-122) and the The Dutch Heart Foundation (grant 2007B161).

Chapter 4

Carotid wall volume quantification from magnetic resonance images using deformable model fitting and learning-based correction of systematic errors

Based on:

K. Hameeteman, R. van 't Klooster, M. Selwaness, A. van der Lugt, J.C.M. Witteman, W.J. Niessen and S. Klein, Carotid wall volume quantification from magnetic resonance images using deformable model fitting and learning-based correction of systematic errors, *Physics in Medicine and Biology*, 58(5):1605, 2013.

4.1 Introduction

The prevalence of cardiovascular diseases is rising and heart disease is the leading cause of death in the western world, claiming approximately one out of every five lives (Roger *et al.*, 2011). Atherosclerosis, a disease of the vessel wall, is the primary cause of cardiovascular disease. Atherosclerotic wall thickening in the carotid arteries can cause a narrowing or total occlusion of the lumen. Atherosclerotic plaque that does not cause occlusion may still lead to clinical events because of rupture and development of thromboembolism, which may subsequently lead to cerebral ischemia (Glagov *et al.*, 1987). Consequently, much research is aimed at finding parameters that describe the plaque, and which can be used to improve risk stratification and for monitoring the progression of atherosclerotic disease. One of those parameters is the size of the plaque and its relation to the size of the vessel.

Magnetic Resonance Imaging (MRI) is an important means to monitor and quantify the state of the vessel wall and lumen. Several studies have shown the possibility to visualize the vessel lumen and outer wall on MRI (Dehnavi *et al.*, 2007; Takaya *et al.*, 2006; Varghese *et al.*, 2005; Zhang *et al.*, 2003; Kang *et al.*, 2000; Yuan *et al.*, 1998). Annotation of both the lumen border and the outer vessel wall is a laborious task. Therefore, several researchers have proposed automatic wall segmentation methods e.g. (Yuan *et al.*, 1999; Van 't Klooster *et al.*, 2012). Although calculating the volume of the vessel wall is straightforward once a segmentation is made, a comparison between automatic and manual wall volume measurements has, to the best of our knowledge, not yet been done.

In this chapter we present an automatic method to measure carotid wall volume from MR images. The contribution is five-fold:

1. The automatic method combines a deformable model approach (Van 't Klooster *et al.*, 2012) with a learning-based postprocessing step, in which systematic segmentation errors of the deformable model fitting are corrected. The idea behind this segmentation correction was developed by Wang *et al.* (2011). However, whereas the method described by Wang *et al.* (2011) was designed for brain structure segmentation, we modified it such that it can handle vessel-shaped structures.

2. An intensity inhomogeneity correction method is designed to compensate for the non-uniform sensitivity pattern of the RF surface coils.

3. A training set of eight subjects with manual annotations is used to exhaustively optimize a number of algorithm parameters.

4. The final algorithm is evaluated on a different set of 19 subjects, and the automatic results are compared with manual vessel wall volume measurements and inter-observer variability.

5. All image data used in this study together with the manual and automatic measurements are made available through the website http://ergocar.bigr.nl.

The remainder of this chapter is organized as follows. Firstly, Section 4.2 explains the deformable model fitting and learning-based segmentation correction, and the wall volume quantification. Section 4.3 describes the image data and the preprocessing steps. Section 4.4 describes the experiments that were conducted to optimize the parameters of the method and to evaluate the wall volume quantification. The results of the experiments are given in Section 4.5. Discussion and conclusion are given in Sections 4.6 and 4.7 respectively.

4.2 Methods

4.2.1 Deformable model fitting

The method described by Van 't Klooster *et al.* (2012) was used to create an initial segmentation of the lumen and outer wall. This method requires a MR Angiography (MRA) image and a Black Blood (BB) image. The MRA image is used to obtain a robust initial segmentation of the carotid lumen. This segmentation is copied to the BB image and based on this initialization, the lumen and outer wall are segmented. The MRA and BB images are assumed to be co-registered (see Section 4.3.3). The only required user input consists of two initialization points. Based on these, the method fully automatically fits a deformable surface model of the lumen and the outer wall to the image data. Below, a brief description of this method is given which is summarized in Figure 4.1. For further details we refer to Van 't Klooster *et al.* (2012).

The method starts with a two-point initialization: one in the common carotid artery (CCA) and one in the internal carotid artery (ICA). These two points are used to initialize a wavefront propagation (De Koning *et al.*, 2003) in the MRA image which results in an approximate centerline with an associated lumen diameter estimate (white contour in frame 1 of Figure 4.1) at each centerline position. This centerline together with the diameters is used to initialize a NURBS surface (De Koning *et al.*, 2003) (suface mesh in frame 2). The method then performs an optimization step in which the boundaries of the NURBS surface are more precisely fit to the lumen boundaries in the MRA image by searching for the maximum gradient magnitude in an intensity profile with a specified length (dL_{MRA}) perpendicular to the lumen surface (frame 3 shows the location of a profile and frame 4 the corresponding intensities along the profile; frame 5 shows an update of the initial contour). Only those edges are selected which have a high value (bright) inside the model and a low value (dark) outside the model. This optimization step is performed for a given number of iterations (nL_{MRA}).

The lumen NURBS surface found in the MRA image is used to initialize the lumen segmentation in the BB image (frame 6). Here, the same optimization of the surface fit to the lumen boundary is performed as in the MRA image (frame 7 and 8), using again a specified length (dL_{BB}) of the intensity profile and number of iteration steps (nL_{BB}). The edge direction in this step is set from dark inside the model to bright outside the model.

The estimated lumen surface is expanded and used to initialize the search for the outer wall. This is done in the same manner as for the BB lumen segmentation, by searching for the maximum gradient magnitude in an intensity profile with a specified length (dW_{BB}) for a number of iterations (nW_{BB}). For this segmentation step, the edge direction is set from bright

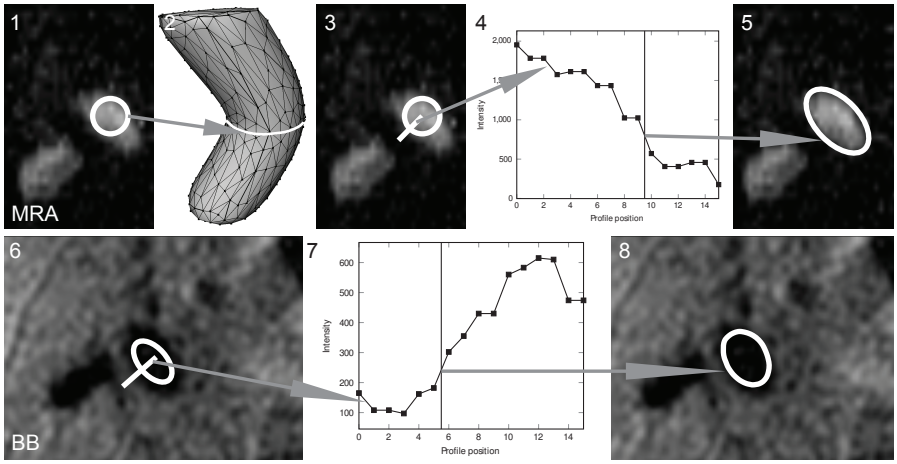

Figure 4.1: Graphical summary of the deformable model fitting method. An MRA segmentation based on wavefront propagation (1) is used to initialize a NURBS surface (2), which is fit to the lumen boundary by searching for a maximum gradient magnitude (4) along an intensity profile (3). The resulting segmentation is used as initialization in the BB image (6) where it is optimized (7,8) in the same manner as is done in the MRA image.

inside the model to dark outside the model.

4.2.2 Learning-based correction of systematic errors

Using a deformable model to acquire an automatic segmentation limits the precision of the final segmentation to the flexibility of the used (NURBS) model. In areas where there is a sudden change in the shape of the vessel, this may lead to errors. Also, the deformable model approach described in the previous section was originally designed and optimized for one particular set of images. To compensate for the limitation of the deformable model and to adjust for the differences in image characteristics when using a different scanner, surface coil, and/or different MR acquisition parameter settings, we propose to use a postprocessing step in which the segmentation is tailored to a new set of images. The idea behind this method was developed by Wang *et al.* (2011). We will refer to this method as the Learning-Based Segmentation Correction (LBSC) method. As the LBSC method was designed for brain structure segmentation, we modified it to be able to handle vessel structures. We will refer to this modified method as the Learning-Based Vessel Segmentation Correction (LBVSC) method.

The LBSC method uses a ground truth segmentation (in our case manual annotations) to train a classifier that modifies a binary segmentation made by a host segmentation method (in our case the result from the deformable model fitting described in Section 4.2.1). The LBSC method classifies all voxels in a region of interest (ROI), which is created by dilating the host segmentation. For each voxel, a feature vector is computed, consisting of:

- all image values in a 5x5x5 neighborhood of the voxel in the MR image (125 features)
- all values in a 5x5x5 neighborhood of the voxel in the host segmentation (125 features)
- x, y and z coordinate of the voxel relative to the center of mass of the host segmentation (3 features)
- product of the neighborhood and coordinate features ($3 * (125 + 125)$ features)

This leads to a total of 1003 features. The LBSC method trains a classifier on the difference between the host segmentation and the manual annotation. It thus learns to correct the errors made by the host segmentation. AdaBoost is chosen as classifier, which combines many weak classifiers (regression stumps) into a single strong classifier (Freund and Schapire, 1997). The AdaBoost classifier has previously been shown to be successful in the context of medical image segmentation (Tu *et al.*, 2007; Morra *et al.*, 2008).

For our application, a number of modifications are proposed: We use the signed distance to the host segmentation's border and the z-index as spatial features. Since the carotid artery is roughly perpendicular to the transversal plane, this latter feature is an approximation of the position along the centerline. For elongated structures like vessels, these two spatial features seem more appropriate than the distance to the center of mass. In addition to these spatial features we used the intensity of the BB image and its gradient magnitude. Instead of using a 5x5x5 neighborhood we used a 7x7x3 neighborhood. The effect of this neighborhood size, ($fL_x \times fL_y \times fL_z$ and $fW_x \times fW_y \times fW_z$ for the lumen and outer wall feature neighborhood respectively) on the segmentation accuracy was determined experimentally (see Section 4.4.2). Thus the two spatial features of the LBVSC method are:

- signed distance to the boundary host segmentation (1 feature)
- relative z-index (1 feature)

The 441 appearance features are the 7x7x3 neighborhood voxels of:

- the host segmentation (i.e. 0 or 1) (147 features)
- the BB image (147 features)
- the gradient magnitude of the BB image (147 features)

Similar to the LBSC method we also used the product of the spatial and appearance features as additional features $(2 * (147 + 147 + 147)) = 882$, leading to a total of $2 + 441 + 882 = 1325$ features.

Since most errors in the host segmentation are near the boundary of the segmentation, our LBVSC method only classifies the voxels within a ROI around this boundary. This region is defined by a morphological dilation minus an erosion of the binary host segmentation using a spherical kernel with radius rL_{dilation} and rL_{erosion} for the lumen and rW_{dilation} and

rW_{erosion} for the outer wall segmentation. The binary host segmentation of the outer wall includes the lumen area.

When the classifier is trained on the difference between the host segmentation and the manual annotation (as in the original LBSC method), only the voxels that are not correctly segmented in the host segmentation get a negative label. If the host segmentation has large overlap with the manual annotation, this leads to many positive samples and only a few negative samples. To prevent this unequal class sizes we trained the AdaBoost classifier directly on the label from the manual annotation, which leads to a better balance between the classes. To make the classification tractable, only half of the randomly selected voxels within the ROI are used as samples.

Whereas the output of the deformable model fitting described in Section 4.2.1 is smooth, the output of the LBVSC method may have holes or isolated voxels. Therefore a morphological closing with a kernel radius of 2 voxels is applied to the output of the LBVSC method and isolated voxels are removed using connected components analysis.

4.2.3 Vessel wall volume quantification

The vessel wall volume V_{wall} is quantified in a region of 25 mm in the transversal direction centered at the bifurcation. The bifurcation point is manually annotated and defined as the first transversal plane on which two separate lumens (one of the ICA and one of the External Carotid Artery (ECA)) are visible. In cases where part of the evaluation region falls outside the scan range, the evaluation region is restricted by the image boundaries.

Application of the LBVSC method results in a binary mask for the lumen and the outer wall. The difference of these two masks is defined as the vessel wall. The vessel wall volume is computed by voxel counting and multiplying the result with the volume of one voxel.

Besides the volume, a clinically used parameter to quantify the vessel wall V_{wall} is the Normalized Wall Index (NWI) which is defined as:

$$\text{NWI} = \frac{V_{\text{wall}}}{V_{\text{lumen}} + V_{\text{wall}}} \tag{4.1}$$

where V_{lumen} is the volume of the vessel lumen. Bigger plaques thus lead to a higher NWI.

4.3 Data specific preprocessing

4.3.1 Data description

The image data of this study is taken from a prospective, population-based study among subjects aged 45 years and older. This study has been described in detail elsewhere (Hofman *et al.*, 2011). All participants having a maximum intima-media thickness of more than 2.5 mm (determined using Ultra Sound (Van den Bouwhuijsen *et al.*, 2011)) in at least one carotid artery were invited for a carotid MRI exam. In total, 1072 participants were scanned.

MRI of the carotid arteries was performed on a 1.5-T MR scanner (Signa Excite, GE Healthcare, Milwalkee, USA) with a bilateral phased-array surface coil. To reduce motion artifacts,

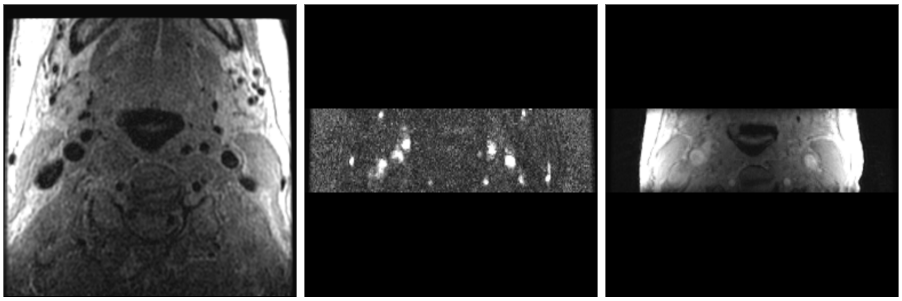

(a) BB **(b)** PC **(c)** PCMag

Figure 4.2: Example slice near the bifurcation of the three different MR sequences used in this study.

subjects were stabilized in a custom-designed head holder. The total scanning time was about 30 minutes in which *i.a.* the following sequences were acquired (see Van den Bouwhuijsen *et al.* (2011) for acquisition details):

- Proton density weighted Fast Spin Echo Black-blood (BB)
- Phase Contrast sequence which consists of an image showing flow in any direction (PC), a magnitude image (PCMag) and 3 images for the flow in the x, y and z direction.

The PC is used as MRA image for the deformable model fitting (see Section 4.2.1) and the PCMag image is used to register the PC image to the BB image (see Section 4.3.3). Figure 4.2 shows an example slice of each of these MR sequences.

4.3.2 Inhomogeneity correction

The bilateral phased-array surface coils cause severe intensity inhomogeneity within the neck. The sensitivity near the skin is much higher than in the middle of the neck. Figure 4.3c shows a typical example of the intensity profile across the neck in a BB image. Many popular intensity inhomogeneity correction methods have strong assumptions on the distribution of the modeled bias field. For example, N3 (Sled *et al.*, 1998) and N4 (Tustison *et al.*, 2010) assume the distribution of the bias field intensities to be log-normal. Other methods like the one proposed by Brinkmann *et al.* (1998) and Cohen *et al.* (2000) assume a slowly varying bias field. These methods do not result in a satisfactory correction of the intensity inhomogeneities in the case of phased-array surface coils. The method proposed by Salvado *et al.* (2006), called Local Entropy Minimization with a bicubic Spline model (LEMS), was designed to deal with inhomogeneities caused by phased array surface coils.

The original LEMS method was designed for 2D images. To ensure a smooth bias field across slices, we extended the method to 3D with the following modifications.

LEMS tries to identify the voxels that do not have any signal as they cannot be used to estimate the bias field. We estimated the background voxels using the whole 3D image. Furthermore, the 2D slice based estimation of the bias field is smoothed in the slice direction using Gaussian blurring with a σ of 3 slices.

This way a spatially smooth bias field is obtained as can be seen in Figure 4.4.

Because the LEMS method uses a multiplicative bias field model, the correction is performed by dividing the original image by the estimated bias field. This can lead to very large intensity values in the corrected image in regions where the estimated bias field has small values. The registration between the BB and MRA image (see Section 4.3.3) is hampered by a few extremely high intensity values within the image, therefore the highest 1% of the intensities of the corrected image are clamped. Figure 4.3a and 4.3b show an example of the BB image before and after inhomogeneity correction, respectively, and the effect of the correction on the intensity profile can be seen in Figure 4.3c.

4.3.3 Registration

As stated in Section 4.3.1, the complete MRI exam takes approximately 30 min. Although the position of the head of the subjects is stabilized using a head-holder, they still have the ability to move their body, which can cause twisting of the neck. Moreover, cardiac and breathing motion can also lead to displacement of the arteries in the neck. This motion leads to small mis-registrations between the different sequences. The lumen and vessel wall segmentation method described in Section 4.2.1 requires a registered BB and MRA image. We perform an intensity-based registration method to align the images. The PC image contains very little anatomical information as can be seen in Figure 4.2b and is therefore not very well suited for an intensity based registration. The PCMag image (shown in Figure 4.2c) which is simultaneously acquired with the PC image contains much more anatomical information. Therefore the PCMag image was registered to the BB image and the resulting deformation was applied

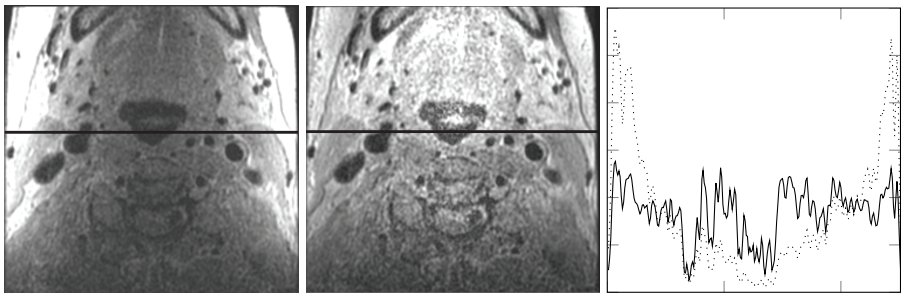

Figure 4.3: Example of the intensity inhomogeneities caused by a surface coil (a), the same image after applying the LEMS method (b) and the intensity profiles of the red line in the original (black, dashed line) and the corrected (gray, solid line) image (c).

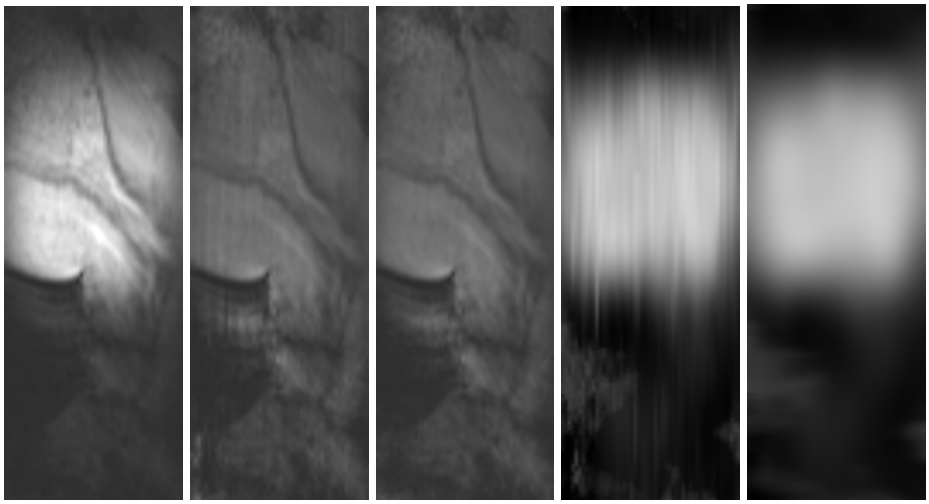

(a) original **(b)** LEMS **(c)** LEMS 3D **(d)** Bias field **(e)** 3D Bias field

Figure 4.4: Inhomogeneity correction using LEMS and smoothing the estimated correct field. Sagital slice of (a) the original BB image, (b) after correction using standard LEMS, (c) using LEMS with smoothed bias field, (d) estimated bias field of the standard LEMS method and (e) estimated bias field with smoothing in the slice direction.

to the PC image.

The registration first performs a rigid registration step to compensate for global displacements. Because the BB image and the PCMag image contain different anatomical regions, a mask was used for both the fixed and the moving image to indicate the regions where there should be overlapping information. The rigid registration was followed by a B-Spline registration (Rueckert *et al.*, 1999) using mutual information as similarity metric (Thévenaz and Unser, 2000). For the optimization we used an adaptive stochastic gradient descent optimizer (Klein *et al.*, 2009). The registration was performed in a multi-resolution framework with three resolution levels and was achieved using the ITK (Ibanez *et al.*, 2005) based registration toolbox `elastix` (Klein *et al.*, 2010).

4.4 Experiments

For the experiments, 27 subjects were randomly selected from the full database. This evaluation set was split in a training set of 8 subjects and a test set of 19 subjects. The training set was used to optimize the parameters of the deformable model fitting (dL_{MRA}, nL_{MRA}, dL_{BB}, nL_{BB}, dW_{BB} and nW_{BB}) and the LBVSC method (rL_{dilation}, rL_{erosion}, rW_{dilation}, rW_{erosion}, $fL_{\text{x}} \times fL_{\text{y}} \times fL_{\text{z}}$ and $fW_{\text{x}} \times fW_{\text{y}} \times fW_{\text{z}}$). The test set was used to evaluate the vessel wall volume and NWI quantification.

4.4.1 Manual annotations

On the complete set of 27 subjects the lumen and outer wall of both the left and the right carotid artery were annotated manually by observer 1 (ob1). On the test set observer 2 (ob2) performed the same annotations. The manual annotation started with an accurate definition of the centerline, after which longitudinal contours along this centerline were drawn in a curved planar reformatted image for both the lumen and the outer wall. These longitudinal contours were used to create cross-sectional contours perpendicular to the centerline. The cross-sectional contours were then adjusted to fit the lumen and the outer wall. More details on the annotation process can be found in Chapter 3. The manual annotations were converted into binary masks for calculating the Dice (Dice, 1945) overlap coefficient and using the masks in the LBVSC step. The mask generation was achieved by fitting a surface through the contour points using variational interpolation (Heckel *et al.*, 2011) and voxelizing this closed surface. The mask of the outer wall contains everything within the outer wall including the lumen.

The manual annotations of the ICA do not incorporate the external part in the bifurcation region. Because the automatic method does not differentiate between ICA and ECA in the bifurcation region, the automatic segmentation may cover a larger part of the lumen area within the bifurcation region. This larger automatic segmentation is not wrong, but would result in errors during the evaluation because the manual ground truth does not contain the ECA. To make sure that this does not influence the evaluation results, the ECA region of the bifurcation was masked out and no evaluation was done in that region.

4.4.2 Parameter optimization

Surface distance

Since there is no ground truth definition in the MRA sequence, the values of profile length dL_{MRA} and the number of iterations nL_{MRA} were chosen such that the resulting segmentation visually provided a good initialization for the BB lumen segmentation.

For the parameter optimization of the deformable model fitting in the BB image, a distance measure was computed between the NURBS surface and the manual contours. First, the surface was intersected with the MPR plane (perpendicular to the centerline) in which the contours were drawn. This created a contour for the automatic segmentation. Then the symmetric average Euclidean distance between the manual and automatic contours was calculated. This distance was calculated for all manual contours and the average was computed for each carotid. The average over all carotid segmentations in the training set (denoted by $\delta L_{\text{surface}}$ and $\delta W_{\text{surface}}$ for the lumen and outer wall segmentation, respectively) was used as optimization objective.

The dL_{BB}, nL_{BB}, dW_{BB} and nW_{BB} parameters were selected by an exhaustive search, minimizing $\delta L_{\text{surface}}$ and $\delta W_{\text{surface}}$. First the lumen parameters were optimized and then the outer wall parameters. The value of dL_{BB} was optimized between 5 and 25 mm in steps of 2 mm. The number of iterations nL_{BB} was optimized over the following set: {5,10,15,25,50,75,100,150}. The outer wall parameter dW_{BB} was optimized between 5 and 15 mm in steps of 2 mm and nW_{BB} over the following set: {0,1,2,3,5,7,10,25,50,75}. Each combination of profile length and

number of iterations was tested, leading to 88 lumen experiments and 60 outer wall experiments.

Learning-based vessel segmentation correction

The influence of the neighborhood size of the features, $fL_x \times fL_y \times fL_z$ and $fW_x \times fW_y \times fW_z$, on the resulting segmentation was determined for the following values: 3x3x3, 5x5x3, 5x5x5, 7x7x3, 7x7x5, 7x7x7, 9x9x3, 9x9x5, 9x9x7, 9x9x9. For each of these feature neighborhoods the optimal combination of rL_{dilation} and rL_{erosion}, and rW_{dilation} and rW_{erosion} was determined. These LBVSC parameters were optimized with respect to the Dice overlap of the resulting segmentation with the manual segmentation. For each combination of neighborhood size dilation and erosion radius, a new classifier was trained. As the training of each classifier took several hours, performing cross-validation on the training set would take too much time. Therefore each classifier was trained on the complete training set and the evaluation of the resulting segmentation was also performed on the complete training set. This may lead to an overestimation of the performance of the LBVSC method. This is of minor importance, since these experiments are only meant to optimize the dilation and erosion parameters, and the true performance will be evaluated on the test set (see Section 4.5.3). The dilation and erosion radii were varied over the interval $[0, 9]$ mm in steps of 1 mm. The AdaBoost classifier was trained using 400 iterations.

4.4.3 Evaluation on test set

The algorithm was evaluated on the 38 carotids of the 19 datasets in the test set. We evaluated the final segmentation of the lumen and the outer wall by calculating the Dice coefficient for each. This evaluation was done both without the segmentation correction step, and applying the original LBVC method and our modification, the LBVSC method. The significance of the difference caused by applying the segmentation correction methods was tested using a paired t-test.

The vessel wall volumes and NWI from the manual annotations were computed in the same way as for the automatic segmentation (see Section 4.2.3). This was done for both observers that annotated the test set.

The manual and automatic wall volumes were compared by calculating the average difference between the two volumes, the average difference of the NWI and the standard deviation of these two difference measures. Also the Pearson and intra-class correlation (Shrout and Fleiss, 1979) coefficient were calculated.

In these evaluations on the test set both observers were compared to each other and to the automatic method.

The influence of the number of training sets for the LBVSC method was determined by increasing this number from 10 until 18 in steps of 2. Because for the eight datasets in the training set no manual segmentations of the second observer was available, we only used the manual annotations of the first observer for evaluation. For each training set size (10, 12, 14, 16 and 18 datasets) 10 different random selections of the 38 data sets were made and the

nL_{BB} \ dL_{BB} (mm)	5	7	9	11	13	15	17	19	21	23	25
5	0.84	0.77	0.73	0.70	0.69	0.69	0.71	0.90	0.91	0.92	0.93
10	0.76	0.62	0.54	0.51	0.50	0.50	0.51	0.72	0.73	0.74	0.74
15	0.70	0.54	0.46	0.44	0.43	0.43	0.45	0.66	0.66	0.66	0.67
25	0.65	0.47	0.40	0.39	**0.39**	0.39	0.42	0.63	0.63	0.64	0.65
50	0.70	0.53	0.49	0.46	0.45	0.43	0.46	0.52	0.63	0.71	0.87
75	0.68	0.52	0.48	0.45	0.46	0.45	0.48	0.56	0.78	0.82	0.94
100	0.67	0.50	0.48	0.45	0.46	0.47	0.49	0.59	0.78	0.92	0.96
150	0.65	0.50	0.47	0.45	0.47	0.47	0.51	0.64	0.80	1.30	0.96

Table 4.1: Average surface distance $\delta L_{\text{surface}}$ for the various settings of profile length dL_{BB} and the number of iterations nL_{BB} used in the BB lumen segmentation. The minimum value is shown in bold font.

results of these 10 experiments were averaged. Just as in the other evaluations on the test set we calculated the Dice coefficient between the automatic segmentation of the lumen and the outer wall.

4.5 Results

4.5.1 Parameter optimization

The PC MRA images used in this study have a lower contrast compared to the TOF images used in (Van 't Klooster *et al.*, 2012). Especially in the bifurcation area the optimization of the MRA lumen surface generated a small or "half moon" shaped vessel surface leading to a bad initialization for the BB lumen segmentation. To handle this problem we drastically reduced the number of iterations, nL_{MRA}, to 1 and kept the profile length dL_{MRA} to the minimum of 5 voxels. This gives the NURBS surface less freedom to adjust and results in a more circular cross-section of the segmented lumen.

Table 4.1 and 4.2 show the results of the optimization experiments for the lumen and outer wall parameters respectively. The bold cell indicates the optimal value, i.e the minimal average surface distance $\delta L_{\text{surface}}$ and $\delta W_{\text{surface}}$. We did not perform any experiments using a profile length of less than 5 mm as this would require the estimation of a gradient on less than 3 voxels.

Learning-based vessel segmentation correction

Figure 4.5 shows for each neighborhood size the maximum Dice overlap (optained with optimum settings of the erosion and dilation parameters, which may be different for each neighborhood size). As can be seen from Figure 4.5 the influence of the feature neighborhood size on the segmentation accuracy is relatively small for both lumen and outer wall. As the computational costs increase significantly with a growing feature neighborhood we chose a neighborhood size of 7x7x3, which is computationally feasible and accounts for the anisotropic

nW_{BB} \ dW_{BB} (mm)	5	7	9	11	13	15
0	0.54	0.54	0.54	0.54	0.54	0.54
1	0.52	0.51	0.50	0.50	0.50	0.50
2	0.51	0.50	0.49	0.49	0.49	0.49
3	0.49	0.49	0.50	0.54	0.58	0.62
5	**0.48**	0.50	0.57	0.67	0.75	0.84
7	0.49	0.53	0.66	0.81	0.93	1.05
10	0.51	0.61	0.82	1.02	1.19	1.34
25	0.62	0.90	1.27	1.59	1.87	2.11
50	0.74	1.12	1.55	1.95	2.28	2.57
75	0.81	1.23	1.69	2.11	2.50	2.83

Table 4.2: Average surface distance $\delta W_{surface}$ for the various settings of the profile length dW_{BB} and the number of iterations nW_{BB} used in the BB outer wall segmentation. The minimum value is shown in bold font.

voxel size.

Table 4.3 and 4.4 show the Dice overlap values for the 7x7x3 feature neighborhood size for different combinations of dilation and erosion radii, $rL_{dilation}$, $rL_{erosion}$, and $rW_{dilation}$ and $rW_{erosion}$ for the lumen and outer wall, respectively. The maximum Dice coefficients are shown in bold font. The values for a dilation and erosion with zero radius show the Dice overlap without applying the LBVSC method. The tables for the other feature neighborhood sizes can be found on the website http://ergocar.bigr.nl. In both Table 4.3 and 4.4 the

$rL_{dilation}$ (voxels) \ $rL_{erosion}$ (voxels)	0	1	2	3	4	5	6	7	8	9
0	78.9	80.4	80.6	80.8	80.8	80.8	80.8	80.7	80.8	80.8
1	85.1	84.7	85.0	85.2	85.2	85.2	85.2	85.2	85.1	85.1
2	86.2	85.7	86.0	86.1	86.1	86.2	86.1	86.2	86.2	86.2
3	87.2	86.8	87.1	87.1	87.1	87.2	87.2	87.2	87.2	87.2
4	88.2	87.9	88.1	88.0	88.1	88.1	88.0	88.1	88.2	88.2
5	88.6	88.5	88.8	89.1	88.9	**89.1**	88.8	88.9	88.8	88.8
6	88.8	88.3	88.9	88.6	88.7	88.6	88.7	88.9	89.0	89.0
7	88.8	88.0	88.3	88.7	88.6	88.9	88.8	88.7	88.9	88.9
8	88.5	87.7	88.2	88.5	88.3	88.5	88.5	88.5	88.5	88.5
9	88.2	87.6	87.9	88.0	88.1	88.1	88.3	88.2	88.1	88.0

Table 4.3: Average lumen Dice overlap values of the final segmentation for various sizes of the region around the host segmentation border which is defined by the dilation $rL_{dilation}$ and erosion $rL_{erosion}$ radius. The maximum value is in bold font. The value for zero dilation and erosion is the Dice overlap value for the uncorrected segmentation.

value for zero dilation and erosion is the smallest. On the training set the LBVSC method improved the segmentation result of the deformable model fitting: with any setting of $rL_{dilation}$,

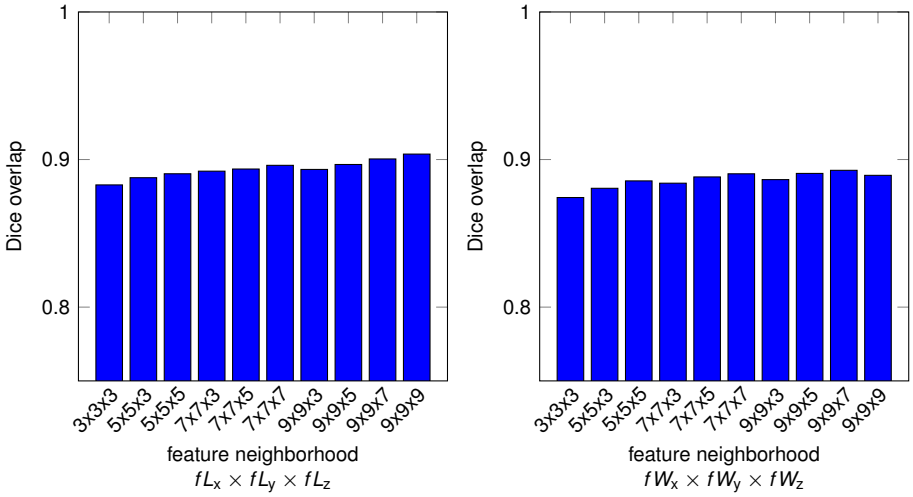

Figure 4.5: Influence of the feature neighborhood size on the final Dice overlap with the manual segmentation for (a) the lumen and (b) the outer wall.

rL_{erosion}, rW_{dilation} and rW_{erosion} the results was better than $rL_{\text{dilation}} = rL_{\text{erosion}} = 0$ or $rW_{\text{dilation}} = rW_{\text{erosion}} = 0$.

4.5.2 Optimal parameters

Table 4.5 summarizes the optimal method parameters for both the lumen and the outer wall segmentation.

4.5.3 Evaluation on test set

The average Dice similarity coefficients for the lumen and outer wall are listed in Table 4.6. The average Dice overlap between the automatic segmentation and both observers is comparable to the Dice between the two observers. The overlap with the first observer is higher, which is expected as the automatic method was trained using the segmentations of this observer. The LBSC method only improved the outer wall segmentation of the observer on which it was trained. There was no significant difference for the lumen segmentation. The LBVSC method significantly increased the average lumen overlap for observer 1 whereas it remained the same for observer 2. For the outer wall the LBVSC method has a positive effect on the Dice overlap with respect to both observers.

The difference in effect of the LBVSC method between the training (Table 4.3 and 4.4) and test set (Table 4.6) is explained by the fact that in the former the training set was used to both

$rW_{dilation}$ (voxels) \ $rW_{erosion}$ (voxels)	0	1	2	3	4	5	6	7	8	9
0	81.3	82.2	82.3	82.4	82.3	82.3	82.4	82.3	82.4	82.4
1	85.5	85.6	85.5	85.5	85.5	85.6	85.5	85.6	85.5	85.4
2	86.4	86.4	86.4	86.4	86.4	86.4	86.4	86.4	86.5	86.4
3	87.2	87.3	87.3	87.3	87.3	87.3	87.3	87.3	87.1	87.3
4	87.8	87.9	88.0	87.9	87.9	87.9	88.0	87.9	87.9	88.0
5	88.3	88.3	88.3	88.2	88.3	88.3	88.3	**88.3**	88.3	88.2
6	88.2	88.2	88.1	88.2	88.2	88.1	88.3	88.3	88.1	88.1
7	87.8	87.9	87.9	87.9	87.9	87.9	88.1	88.0	88.0	88.1
8	87.8	87.7	87.4	87.8	87.7	87.9	87.9	87.6	87.7	87.5

Table 4.4: Average outer wall Dice overlap values of the final segmentation for various sizes of the region around the host segmentation border which is defined by the dilation $rW_{dilation}$ and erosion $rW_{erosion}$ radius. The maximum value is in bold font. The value for zero dilation and erosion is the Dice overlap value for the uncorrected segmentation.

Lumen		Outer wall	
parameter	value	parameter	value
nL_{MRA}	1	nW_{BB}	5
dL_{MRA}	5	dW_{BB}	5
nL_{BB}	25	$fW_x \times fW_y \times fW_z$	$7 \times 7 \times 3$
dL_{BB}	13	$rW_{dilation}$	5
$fL_x \times fL_y \times fL_z$	$7 \times 7 \times 3$	$rW_{erosion}$	7
$rL_{dilation}$	5		
$rL_{erosion}$	5		

Table 4.5: Optimal lumen and outer wall method parameters

train the classifier of the LBVSC method and measure the effect of the LBVSC method on the Dice overlap of the resulting segmentation (see also Section 4.4.2).

Figure 4.6 gives a visual impression of the effect of the LBVSC method on the outer wall segmentation. The LBVSC method (the dashed white contour) here clearly improved the segmentation of the deformable model fitting method (the solid white contour): it is closer to the manual annotation (solid black contour).

In Figure 4.7 the scatter plots of the volume and NWI measurements by observer 1, observer 2 and the automatic method are shown. The two large markers in the volume measurements indicate two outliers where observer 1 and observer 2 disagree. Figure 4.8 gives an example slice of these outliers where observer 1 and 2 disagreed. The contours shown in Figure 4.8 are the manual annotations of the outer wall for both observers. It is obvious from these segmentations that in this dataset it is very hard to determine the location of the outer vessel wall and both observers made a different choice on what to include in the vessel wall. In the subsequent analysis we removed these outliers.

	Lumen					Outer wall				
	No correction	LBSC	p-value	LBVSC	p-value	No correction	LBSC	p-value	LBVSC	p-value
ob1-ob2	0.90	0.90	–	0.90	–	0.90	0.90	–	0.90	–
ob1-auto	0.83	0.84	0.45	0.86	0.03	0.85	0.86	0.02	0.87	< 0.01
ob2-auto	0.84	0.83	0.64	0.84	0.86	0.83	0.85	0.11	0.86	0.01

Table 4.6: Dice overlap between the different measurements of the test set without segmentation correction and using the LBSC and LBVSC method.

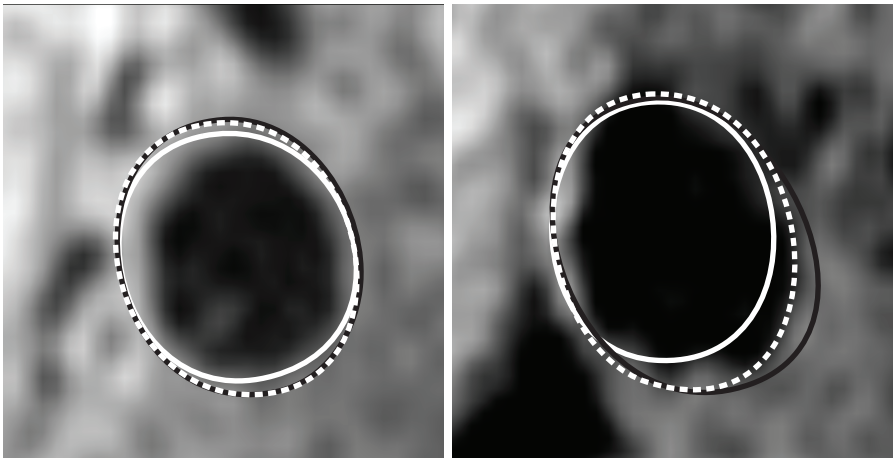

Figure 4.6: Two examples of the effect of the LBVSC method on the outer wall segmentation. The black solid line is the annotation by observer 1, the white solid line is the segmentation from the deformable model fitting method, the dashed white line is the segmentation after applying the LBVSC method.

Table 4.7 gives the average vessel wall volume and NWI measurements of both observers and the automatic method without applying the segmentation correction and with the LBSC and LBVSC method. As can be seen, the automatic segmentation slightly overestimated the vessel wall volume when compared to observer 1 and underestimated the volume when compared to observer 2. Observer 2 on average made larger volume measurements than observer 1. The average vessel wall volume of the automatic method is between the volumes estimated by observer 1 and observer 2, but was on average closer to observer 1 on which it was trained. The p-values of the differences between the automatic method with and without the LBVSC method are 0.0005 and 0.1 for V_{wall} and NWI respectively.

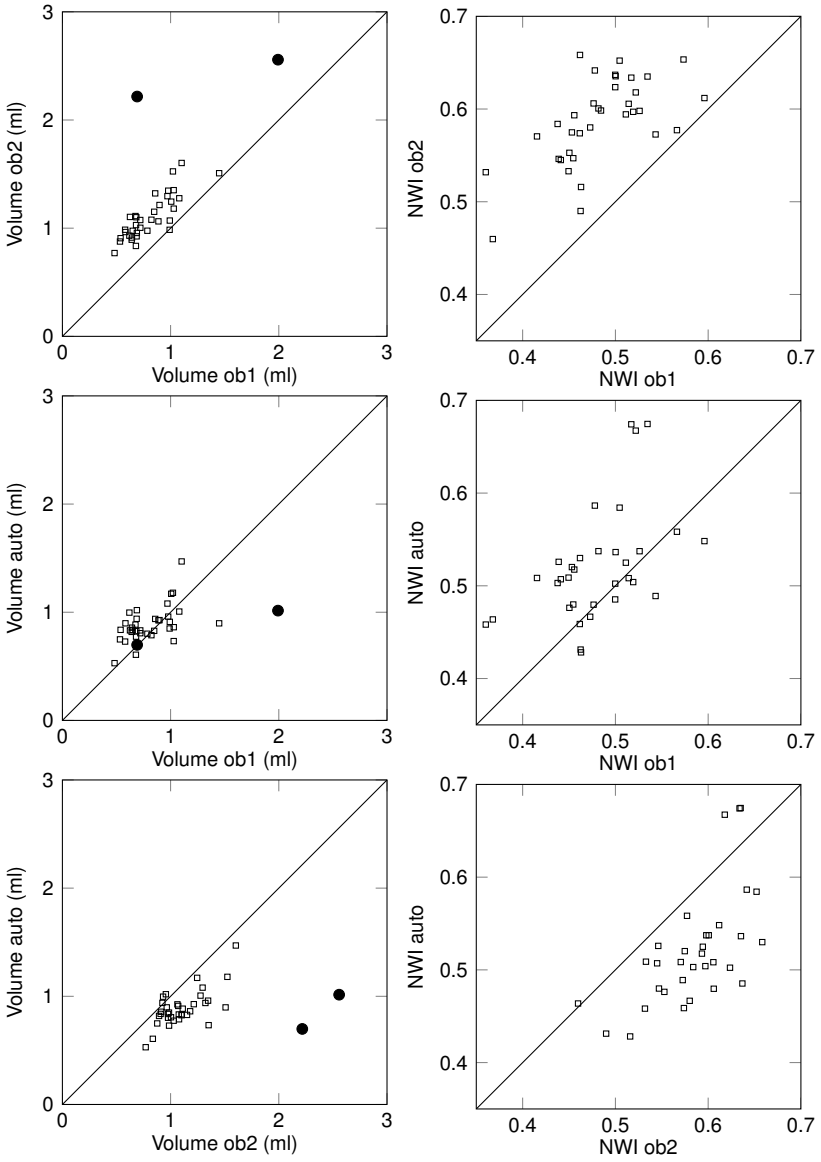

Figure 4.7: Scatter plot of the volume measurements (left column) and normalized wall index (right column) for observer 1 *vs*. observer 2 (top row), observer 1 *vs*. automatic method (middle row) and observer 2 *vs*. automatic method (bottom row). In the volume measurement graphs two outliers are present and shown with filled round markers. These outliers are not shown in the NWI graphs because they would stretch the scale too much.

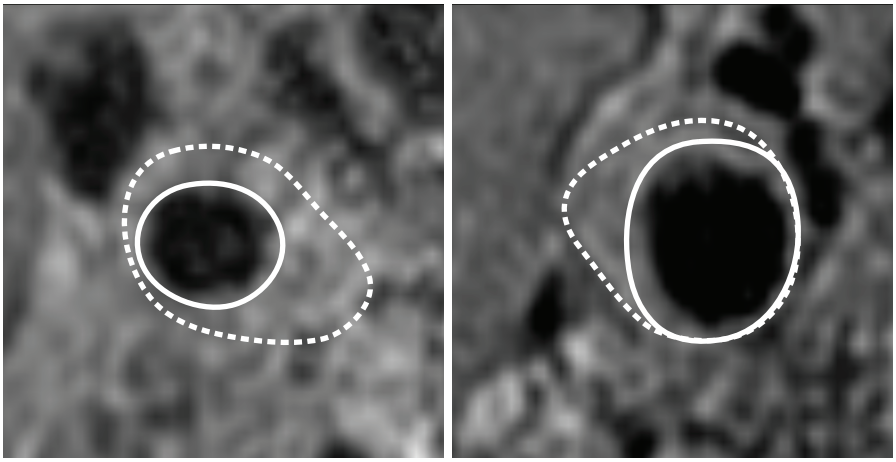

Figure 4.8: Example slice from the two outlier datasets. The solid contour is from observer 1 and the dashed contour from observer 2.

	ob1	ob2	No correction	LBSC	LBVSC
V_{wall} (ml)	0.80 ± 0.21	1.1 ± 0.20	0.78 ± 0.13	0.83 ± 0.11	0.89 ± 0.17
NWI (ml/ml)	0.48 ± 0.05	0.59 ± 0.05	0.51 ± 0.05	0.51 ± 0.05	0.54 ± 0.08

Table 4.7: Average $\pm$ standard deviation of vessel wall volume (ml) and normalized wall index measurements (ml/ml).

Table 4.8 shows the differences, Pearson and intra-class correlations of the volume and NWI measurements. The average difference in the wall volume measurements of the automatic method with respect to both observers is smaller than the average difference between the observers. Although the Pearson correlation coefficient of the volume measurements between the observers and the automatic method is not as good as the correlation between the two observers, the intra-class correlation with both observers is better than (observer 1) or almost the same as (observer 2) between the two observers.

Looking at the clinically used NWI, the average difference between the measurements of automatic method and both observers is again smaller than the average difference between the two observers. Also the correlation coefficients between the automatic method and both observers are better than or almost the same as the correlations between the measurements of the two observers.

Table 4.9 shows the Dice overlap between the manual segmentation of the first observer and the automatic method for different size of the training set. The table show that increasing the size of the training set leads to a small increase in overlap.

	V_{wall}			NWI		
	ΔV_{wall} (ml)	Pearson	icc	ΔNWI (ml/ml)	Pearson	icc
ob2 - ob1	0.30 ± 0.19	0.83	0.58	0.10 ± 0.04	0.51	0.32
auto - ob1	0.08 ± 0.20	0.51	0.62	0.05 ± 0.07	0.50	0.52
auto - ob2	-0.21 ± 0.15	0.57	0.57	-0.05 ± 0.07	0.54	0.56

Table 4.8: The average volume differences, the Pearson and intra-class correlation coefficients of the volume and NWI measurements between the two observers and the automatic method.

Number of training sets	10	12	14	16	18
Dice lumen	0.84	0.84	0.84	0.85	0.86
Dice outer wall	0.85	0.84	0.84	0.85	0.86

Table 4.9: Influence of the number of training sets used for training the LBVSC method on the Dice overlap of the lumen and the outer wall, and the NWI

4.6 Discussion

The interobserver measurements presented in this study show that the systematic difference between the outer vessel wall annotations of two observer can be considerable (see the scatter plots in Figure 4.7). As we do not have manual annotations of the second observer on the training set, it is impossible to train the automatic method on both observers, or generate a new reference standard based on the combined annotations of these two observers without compromising the size of the test set. However, the annotation protocol for both observers was the same and the variation between the two observers can also be expected in clinical practice.

The method described in this paper was designed in order to analyze the MRI data acquired in the context of a population study. This population study uses a 1.5 T MRI scanner and a BB sequence which may not be the best possible sequence for imaging the vessel wall. Despite these limitations the described automatic method performs comparable to the observers. In future research it would be interesting to study the effect of different acquisition settings (1.5T vs. 3T, different MR sequences, the use of a head stabilizer) on the vessel wall quantification. The evaluation described in this study was performed on 19 subjects. For the future we plan a quantification of the vessel wall volume and normalized wall index on all 1072 subjects that participated in this study. Manual measurements on this number of subjects becomes infeasible.

The deformable model fitting method enforces a NURBS model on the lumen and wall boundary, and uses a single image feature (the maximum gradient magnitude) to fit the model. For the lumen border this is an adequate image feature. The gradient of the outer wall is less strong, which makes the application of this image feature less successful. The LBVSC method is not limited to the use of a single image feature, but instead uses many features

to classify the outer wall voxels. This explains the difference in effect of the LBVSC method on the lumen and outer wall segmentation.

As long as there is a training set on which the LBVSC can be trained, the method described in this chapter can easily be adapted to other images, acquired on a higher field MR scanner or using different protocols. If there is a training set consisting of a ground truth definition of multiple observers, these could be combined using existing methods like consensus reading or STAPLE (Warfield *et al.*, 2004), but they can also be used to train multiple classifiers and combine these classifiers into a single stronger classifier using methods described in e.g. (Tax *et al.*, 2000).

4.7 Conclusion

In conclusion, we presented a method that can automatically quantify the wall volume and normalized wall index of the carotid artery in a region around the bifurcation. The method consists of a deformable model fitting step and a learning-based correction of systematic errors. Intensity inhomogeneities in the MR images were reduced using a 3D-extended version of the LEMS method. The parameters of both the deformable model fitting and the LBVSC method have been optimized by extensive experiments using the manual annotations of a single observer on a training set. Evaluation was performed with respect to annotations of two observers on a separate test set. Our experiments justify the conclusion that the automatic method performs comparably to the manual annotations in terms of wall volume and normalized wall index measurements and can therefore be used to replace the manual measurements.

All image data, annotations and results from this study are made available through the website http://ergocar.bigr.nl. We challenge every one to improve our automatic vessel wall volume and normalize wall index measurements on these datasets and publish their results.

Chapter 5

Automatic carotid artery distensibility measurements from CTA using nonrigid registration

Based on:

K. Hameeteman, S. Rozie, C.T. Metz, R. Manniesing, T. van Walsum, A. van der Lugt, W.J. Niessen, S. Klein, Automatic carotid artery distensibility measurements from CTA using nonrigid registration, *Medical Image Analysis*, 17(5):515-524, 2013.

5.1 Introduction

Atherosclerosis of the carotid artery bifurcation is related to cerebral ischemia. Atherosclerosis may lead to luminal stenosis with subsequent hemodynamic consequences. In early stages of the disease, atherosclerotic plaque builds up without lumen narrowing. This may also lead to ischemic events due to plaque rupture with thromboembolisation in the intracranial circulation (Glagov *et al.*, 1987). Consequently, much research is currently focused on finding parameters that describe atherosclerotic plaque rupture risk in order to improve prediction and treatment selection. Arterial wall elasticity is one of the parameters associated with the accumulation of atherosclerotic plaque (Christensen and Neubauer, 1988; Newman *et al.*, 1971). Wall elasticity can be described by the distensibility, a measure of the stiffness of a vessel with respect to the distending pressure. The aim of this study is to investigate the feasibility of manual and automatic measurements of carotid artery distensibility on 4D Computed Tomography Angiography (CTA), to facilitate further research on this biomarkers for atherosclerosis.

The vessel distensibility $\mathcal{D}$ is defined (Laurent *et al.*, 2006) as the maximum change in cross-sectional area, relative to the pressure change, scaled by the minimum area:

$$\mathcal{D} = \frac{\Delta A}{A_{\min} \Delta p} \tag{5.1}$$

To compute this, cross-sectional area change over the cardiac cycle has to be measured. Image-based distensibility measurements thus require imaging over the complete cardiac cycle. Traditionally, arterial stiffness is assessed by acquiring a 2D ultrasound image sequence parallel to the centerline of the carotid artery(Van Popele *et al.*, 2001; Pannier *et al.*, 2002) and subsequently measuring the minimum and maximum vessel wall distances of a region of interest during one or more heart cycles. Assuming a circular cross-section, the lumen area is then calculated or the area parameters in Equation 5.1 are replaced by diameters.

Several studies have demonstrated the feasibility of distensibility measurement in large vessels like the aortic arch and abdominal aorta, using ECG-gated CTA (Weber *et al.*, 2009; Ganten *et al.*, 2008; Zhang *et al.*, 2007). An advantage of CTA over ultrasound is that the true cross-sectional area can be measured precisely, and thus non-circular cross-sections can be accounted for. All these studies used a Multi Planar Reformatted (MPR) image containing the cross-section of the investigated vessel. On these MPR images the lumen was segmented manually on each time frame of the cardiac cycle and voxel counting was used to derive the lumen area.

Manual distensibility measurements become more difficult for smaller vessels, because the annotation error becomes larger with respect to the change in cross-sectional area. Distensibility measurements on the carotid artery, a vessel much smaller than the aorta, may therefore require an automatic method with more consistent and reproducible measurements. In this chapter the feasibility to determine the carotid artery distensibility is investigated using both manual measurements, and a new automatic method.

A number of (semi) automatic methods for quantifying vessel wall deformations have been published (Lalande *et al.*, 2002; Krug *et al.*, 2003; Lorenzo-Valdès *et al.*, 2004; Jackson

et al., 2009; Zhao *et al.*, 2009; Xiong and Taylor, 2010; Biesdorf *et al.*, 2011; Schwartz *et al.*, 2012). Except for Jackson *et al.* (2009) all these methods have been evaluated on the aorta. Most methods use only 2D image information (Lalande *et al.*, 2002; Krug *et al.*, 2003; Lorenzo-Valdès *et al.*, 2004; Jackson *et al.*, 2009) or have been evaluated on other image modalities than CTA (Lalande *et al.*, 2002; Krug *et al.*, 2003; Lorenzo-Valdès *et al.*, 2004; Jackson *et al.*, 2009; Zhao *et al.*, 2009).

Lalande *et al.* (2002); Krug *et al.* (2003) and Jackson *et al.* (2009) perform a segmentation of the aortic lumen in all time frames of a 2D image. The distention is then quantified by calculating the area of the segmentation for each time frame. Lalande *et al.* (2002) compare the compliance based on manual measurements to their automatic method and compare healthy subjects to Marfan syndrome patients, while Jackson *et al.* (2009) evaluate only the reproducibility of the method on clinical data.

Both Lorenzo-Valdès *et al.* (2004) and Schwartz *et al.* (2012) use a combination of segmentation in the first time point and registration of the subsequent time points to analyze the vessel deformation. Lorenzo-Valdès *et al.* (2004) use a 2D analysis but combine all 2D time point images into a single 3D image which is used in the registration. The area change over the heart cycle is then calculated by integrating the determinant of the Jacobian within a manually segmented area of the first time point. Schwartz *et al.* (2012) perform an independent registration of all time points to the first time point and do not quantify the distensibility, but only visualize the effect of stent grafting on the deformations of the vessel.

Zhao *et al.* (2009) take a different approach by performing a 4D graph cut segmentation which is initialized by combining 3D fast-marching based segmentations of each time frame. For the analysis of the deformations over the heart cycle a statistical shape model is constructed. The shape and motion parameters of this model are then used by a support vector machine classifier to distinguish healthy subjects from connective tissue disorder patients. Distensibility nor compliance was quantified in this study.

Both Xiong and Taylor (2010) and Biesdorf *et al.* (2011) use 4D ECG-gated CTA images. Xiong and Taylor (2010) use geodesic active contours to create a segmentation in each frame of the sequence. These segmentations are then used to determine the stress tensor from Cauchy's momentum equation, which describes the deformation of the aorta. Using this model, errors made by the segmentation are reduced. They only report the Young modulus which is used in the model to describe the elasticity of the aorta. Biesdorf *et al.* (2011) fit an elliptical model to the lumen cross-section of the first time frame. The cross-sections of the subsequent time frames are then determined using a Kalman filter.

Our work has three important contributions. First, we demonstrate that manual annotation of the carotid lumen for distensibility measurements is not sufficiently precise. Second, we present and evaluate an automatic method for computing distensibility in the carotid artery from CTA. Third, we make the data on which this study is based, both 4D CTA image data and their associated clinical descriptions, available through our website
().

We first describe the automatic method in Section 5.2, followed in Section 5.3 by a description of the data, the manual method, and the experiments to evaluate both the manual and

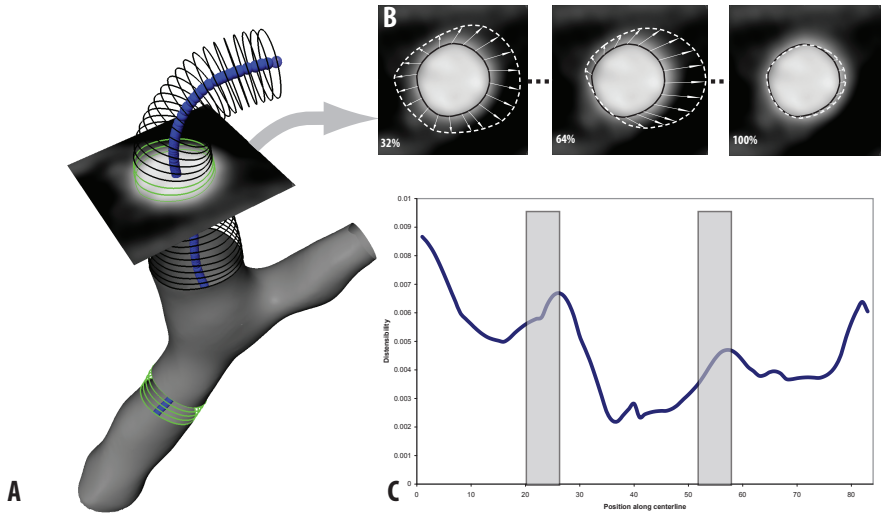

Figure 5.1: (A) Visualization of the lumen surface, the centerline (dark balls), the lumen contours in black and the contours from which the distensibility is determined (light contours). (B) Deformations found using the registration on the plane indicated in (A). The deformations are shown for 32%, 64% and 100% of the RR-interval. The dark solid contour shows the contour of the first cardiac phase, the dashed white contour indicates the deformed contour of the shown cardiac phase. The deformations in (B) are amplified by a factor 10 for illustration purposes. The orange [TODO change color] area at 64% RR-interval shows the determined area change for that time point. (C) Calculated distensibility measures for all positions along the centerline. The horizontal axis corresponds to the positions along the the centerline shown in (A) and the masked areas correspond to the measurements at the light contours in (A).

automatic method. Results follow in Section 5.4 and we end with a discussion in Section 5.5 and conclusion in Section 5.6.

5.2 Automatic method

The automatic method consists of a segmentation method, which generates a surface model of the lumen in the first cardiac phase, and an elastic registration method, which finds the deformation of this lumen surface over all cardiac phases. Using the deformation, the lumen area for each phase can be calculated from which the distensibility can be derived. These steps are explained in more detail below and are illustrated in Figure 5.1.

The method starts with annotating three points x_i, in the common carotid arteries (CCA), in the internal carotid arteries (ICA) and in the external carotid artery (ECA), respectively. Using these three seed points a region of interest (ROI) is defined on which all subsequent processing is performed. To align all time points of the ROI image to the first time point, an elastic registration procedure is performed. After alignment, all time points are averaged to

obtain an image with improved signal to noise ratio (I_{nrd}):

$$I_{nrd} = \frac{1}{N} \sum_{t=0}^{N-1} I_{0t} \tag{5.2}$$

where the summation is over all time points N and I_{0t} is the resulting image of the registration of time point t to the first time point. The lumen is segmented on I_{nrd} and the lumen area over time is derived from the registration result.

5.2.1 Segmentation

To create a surface model of the lumen, a levelset based segmentation method (Manniesing *et al.*, 2010) is applied to the noise reduced 3D image I_{nrd}, where the three seed points $\boldsymbol{x}_i$ are used to initialize the algorithm. The noise reduced image I_{nrd} is used because the lumen segmentation is more stable on this image (see Section 5.3.1 for an example slice). A potential disadvantage of this could be the blurring caused by registration errors. In Section 5.3.6 we therefore evaluate the sensitivity of the method to increased amounts of blurring.

The centerline is found by fitting spheres in the obtained surface model using the Vascular Modeling Toolkit (Antiga and Steinman, 2004). Cross-sectional contours are generated at 0.5 mm intervals along the centerline by intersecting the plane perpendicular to the centerline with the lumen surface (Figure 5.1A).

5.2.2 Registration

Registration of the images at different time points is achieved using the registration toolbox `elastix` (Klein *et al.*, 2010). For each dataset we perform both a set of 3D registrations in which all time points are independently registered to the first time point, and a 4D registration in which all time points are registered simultaneously. A cubic B-spline model is used to parameterize the deformation field (Rueckert *et al.*, 1999). In the 4D technique also the deformation in the time dimension is modeled using a cyclic B-spline resulting in smooth deformations over time (Metz *et al.*, 2011). Because we expect smooth area changes during the cardiac cycle, the 4D registration method is expected to perform better as it imposes these smooth deformations and is more robust against the image noise (Metz *et al.*, 2011). The spatial distance between control points of the B-spline grid is set to 5.0 mm. For the 4D registration method a the control point spacing in the time dimension is set to 1 time point. The influence of this control point spacing in the temporal dimension on the measured distensibility is determined experimentally. The 3D registration technique uses the sum of squared intensity differences as a similarity metric. The 4D registration technique minimizes the variance of the intensities over the time dimension. For the optimization we use an adaptive stochastic gradient descent optimizer (Klein *et al.*, 2009). Registration is performed in a multi-resolution framework with 3 resolution levels. The registration yields a deformation $\boldsymbol{T}_{0t}$, between the first time point (0) and each other time point (t) within the RR-interval (Figure 5.1B).

5.2.3 Distensibility quantification

The change in cross-sectional area of the vessel at a certain centerline position for all cardiac phases is determined from the contours at the first cardiac phase and the deformation field using Gauss' integral theorem (Arfken and Weber, 2005):

$$\Delta A = \iint_{\Omega} \boldsymbol{\nabla} \cdot \boldsymbol{T}_{0t}\, d\Omega = \int_{\partial\Omega} \boldsymbol{T}_{0t} \cdot \boldsymbol{n}\, dr \tag{5.3}$$

where $\partial\Omega$ is the contour around the undeformed lumen area Ω of the first time point and $\boldsymbol{n}$ is the normal to this contour. Using this approach, the area changes within the plane of the contour are calculated ($\boldsymbol{n}$ is in this plane and thus $\boldsymbol{T}_{0t} \cdot \boldsymbol{n}$ is the projection of $\boldsymbol{T}_{0t}$ on the cross-sectional plane) for all time points with respect to the first time point. From the resulting area time curve the distensibility is determined using Equation 5.1 (Figure 5.1C). We then define the distensibility of the CCA and ICA as the average distensibility measurements over sections of 3.5 mm along the centerline (light contours in Figure 5.1A).

5.2.4 Relation to previous work

Using a combination of segmentation and registration to determine the deformations over time was also pursued by Lorenzo-Valdès *et al.* (2004) and Schwartz *et al.* (2012). Schwartz *et al.* (2012) do not report any quantification results. In contrast to Lorenzo-Valdès *et al.* (2004) who analyze 2D cine MR images of the aorta, we consider 3D ECG-gated CTA of the carotid artery. In the case of the carotid artery, 3D information is especially important as the whole artery moves during a heart cycle. Lorenzo-Valdès *et al.* (2004) use a 3D (x,y,t) to 2D registration to ensure a coherent registration over time. However, the cyclic behavior of the motion is not exploited in that model. Our 4D registration method models the deformation of the whole heart cycle as a cyclic B-spline transform (see Section 5.2.2). Furthermore, we use a different method (see Section 5.2.3) to calculate the area change from the registration result. The segmentation of the first time point, which is done manually in Lorenzo-Valdès *et al.* (2004), only requires two initialization points in our method.

5.3 Experiments

The feasibility of manual carotid distensibility measurements was evaluated using inter observer measurements. The performance of the automatic method was assessed by comparison to manual annotations and using synthetically deformed CTA data. Next to this, we quantify the influence of spatial blurring (caused by registration errors and the CTA reconstruction kernel) and temporal blurring (caused by the 4D reconstruction) on the automatic method. We also compared manual and automatic measurements by investigating the relation with cardiovascular risk factors. Below we first describe the CTA data, and subsequently we describe the experimental setup in more detail.

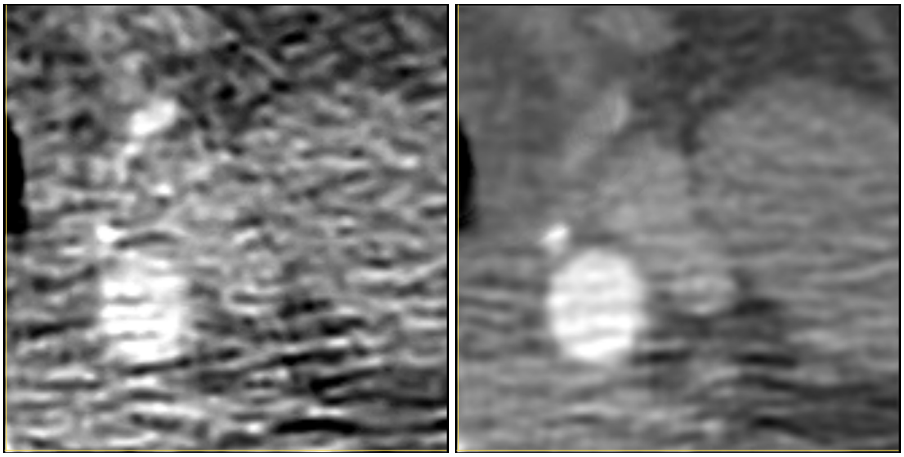

(a) (b)

Figure 5.2: Example slice of the first time point (a) before and (b) after averaging over time.

5.3.1 Data

We acquired 81 4D CTA datasets of patients (mean age 65 ± 9; 48 male, 33 female) with ischemic cerebrovascular symptoms who underwent CTA of the carotid arteries for clinical workup. Scanning was performed on a 64-slice dual-source multi-detector CT scanner (Siemens, SOMATOM Definition, Forchheim, Germany). The ECG-gated CTA data was used to reconstruct multiphase 4D datasets at 8% steps of the cardiac RR interval (the interval between two R waves of the ECG signal), resulting in a time series of 13 3D CTA images per patient for one heart beat. The scan range was 40 mm and image reconstructions were made with a 12 cm field of view, a matrix size of 512x512, a slice thickness of 1.0 mm and an intermediate (B31f) reconstruction kernel. The resulting image had a (x,y,z) resolution of 0.2x0.2x0.5 mm. All patients received 80 ml contrast material followed by 40 ml saline bolus chaser. Figure 5.2a shows an example slice of the image in the first time point and in Figure 5.2b the same slice is shown after averaging over time (I_{nrd}, see Section 5.2). A clinical expert excluded both carotids of five patients because of insufficient image quality and one carotid artery of another patient because of the presence of a carotid stent.

Blood pressure was measured using an arm cuff during two episodes of continuous measurements. The average of these two measurements was calculated and brachial pulse pressure (Δp) was calculated as the difference between mean systolic and mean diastolic pressure.

5.3.2 Manual measurements

Manual measurement was performed on the first 38 CTA datasets that were available. One patient had an occluded carotid artery and another patient had two internal carotid arteries with significant juxtaluminal calcifications, which hampered luminal measurements. Thus

76 CCA and 73 ICA were analyzed. Using a custom made tool based on MeVisLab (MeVis Research, Bremen, Germany) a centerline through the CCA and ICA was drawn in the first cardiac phase for both the left and right carotid artery. Along this centerline MPR images perpendicular to the centerline were created using trilinear interpolation, yielding cross-sections of the carotid artery at different positions along the centerline. The same centerline was used for all 13 cardiac phases. A contour of the lumen area was drawn at two locations along the carotid artery, proximal to the bifurcation in the CCA and approximately 1 cm distal to the bifurcation in the ICA. For every cardiac phase a contour of the lumen area was drawn at the same positions along the centerline. The contours were defined by seed points through which a spline was fitted. The observers could add as many seed points to the contour as they thought were needed to position the contour exactly on the lumen border. The positions of the seed points were not limited to the voxel centers, so the observers were able to draw the contours with subvoxel precision. The cross-sectional area was calculated directly from the drawn contours (Gelder, 1995). In the previous studies on the aorta (Zhang *et al.*, 2007; Ganten *et al.*, 2008; Weber *et al.*, 2009) the area was calculated using voxel counting. Calculation of the cross-sectional area from the drawn contours then leads to the curve of the lumen area during one heart cycle. Using Equation 5.1 the distensibility was then determined.

A second observer annotated the lumen border in the same MPR images. This second annotation was performed on a subset of 10 randomly selected patients for both the left and the right CCA and ICA. As each dataset contains 13 time points, this results in 520 pairs of area measurements and 40 pairs of area change measurements. Both observers used the same centerline to generate the MPR images and drew the contour at the same position along the centerline. In this way the precision of the contour drawing can be estimated.

Interobserver variability in lumen measurements was assessed using Bland-Altman analysis on both the individual area measurements and the maximum area change measured by both observers for each dataset.

5.3.3 Synthetic deformations

To assess the accuracy of the automatic 3D and 4D algorithms, a synthetic deformation was applied to the CTA images and the area change of a circular contour was calculated from both registration results. This experiment was performed on the same 38 datasets for which manual measurements were made. This set was split into two sets, containing the left and right carotid artery respectively.

The 3D test sets were created by using the first time point of the 4D data sets and scaling these 3D datasets in the axial plane using Lanczos resampling (Turkowski, 1990). In this way we approximate an expansion of the blood vessel. The scaling factor was set to $\frac{1}{0.9}$ which is consistent with the expected area change (Zhang *et al.*, 2007; Ganten *et al.*, 2008). The scaled datasets were then registered to the original datasets using the 3D registration method.

To construct the 4D test sets (for the 4D registration method), the scaling factor was

changed over the time points according to the following formula:

$$S(t) = \frac{1}{1 - 0.1\, sin^2(\frac{\pi t}{13})} \tag{5.4}$$

where S is the scaling factor and $t \in [0, 12]$ indicates the time frame. Thus the first time frame is not scaled and half way the cardiac cycle the scaling $S(t = 6)$ is the same as for the 3D test images ($\frac{1}{0.9}$). This time frame ($t = 6$) was used to evaluate the 4D method. Each time frame was scaled individually.

Because the true area change is known, the error in the area change for each of the analysis methods can be calculated:

$$\begin{aligned} E_r &= dA_r - dA_{true} \\ &= (A_r - A_0) - (S^2 * A_0 - A_0) \\ &= A_r - S^2 * A_0 \end{aligned} \tag{5.5}$$

Here E_r is the error in the area change, dA_r is the area change calculated from the registration, dA_{true} is the true area change, A_r is the area calculated from the registration result, A_0 is the area of the initial contour and S is the scaling factor from Equation 5.4. For the 4D registration E_r was calculated for various control point spacings in the temporal dimension.

The 3D and 4D registration based method were compared using a paired t-test.

5.3.4 Comparison of automatic and manual measurements

The area curves resulting from the manual and automatic method were compared for all 38 datasets for which manual measurements were performed. To ensure a fair comparison we used the manual contour of the first time point for the automatic measurements instead of the surface contours of the segmentation. For the automatic measurements in this experiment the averaging over the 3.5 mm section is omitted, since the manual distensibility measurements are also based on one contour only.

The carotid lumen cross-sectional areas of different patients can differ by a factor of more than four. To be able to compare the area curves of different patients, the area curves were normalized by dividing each curve by its mean area over the complete cardiac cycle. Also the curve peak position for each patient can be different due to a different vascular geometry or distance to the heart, which causes the ECG trigger during scanning. To compensate for these peak position differences, all curves were temporarily aligned by synchronizing the position of their maximum value. From the normalized curves the mean curve and the curves representing mean $\pm$ the standard deviation were calculated.

The smoothness of the area curves was assessed by inspecting the absolute value of the second order derivative of the normalized area curves.

The correlation between manual and automatic measurements was calculated using the Pearson correlation coefficient.

5.3.5 Control point spacing in the t-dimension

As the 4D registration method models the transformation over time using a B-spline, the spacing between the control points in the time dimension has a direct influence on the ability of the registration to capture the morphological changes of the carotid artery during a heart cycle. To assess the influence of the temporal control point spacing on the measured distensibility we performed an experiment in which we varied this spacing over the following set: {1, 2, 3, 4} time points which corresponds to {8, 16, 24, 32} % of the RR-interval.

5.3.6 Influence of spatial and temporal blurring

The segmentation of the vessel lumen is performed in a time averaged image after motion compensation using the estimated transformation. This time averaging results in an image with improved SNR, but may also introduce blurring of the lumen border due to registration errors. Furthermore, the used reconstruction kernel (B31f) causes some spatial blurring. To estimate this effect the noise reduced image (I_{nrd}) was blurred using a Gaussian kernel with a sigma of 0.5, 1, 2 and 3 voxels. On this blurred image the lumen was segmented and the distensibility calculated the result of which was compared to the measurements using the non-blurred image.

The 4D ECG-gated CTA reconstruction results in 13 time point images over the cardiac cycle. In cases where there is rapid movement of the carotid artery during a heart beat, this may introduce some blurring. To estimate the effect of temporal blurring, the 4D image was blurred in the time dimension using a Gaussian kernel with a sigma of 0.5, 1, 2 and 3 time points, corresponding to 4, 8, 16 and 24% of the RR-interval. After this temporal blurring the distensibility was calculated and compared to the measurements based on the non-blurred image.

5.3.7 Relation with cardiovascular risk factors

From literature the distensibility is expected to be lower for patients suffering from hypertension (Laurent *et al.*, 1994; Liang *et al.*, 2001). Therefore, we tested whether this association could be reproduced by the manual and automatic measurements. Results of manual and automatic distensibility measurements per location (Left/Right; Common/Internal) were compared between patients with and without the following general cardiovascular risk factors: diabetes, hypercholesterol, hypertension and smoking. The medians of both patient groups were calculated and the 95% confidence intervals for this median were calculated using the Hodges-Lehmann estimator (Deshpande *et al.*, 1995). To determine whether the medians differed significantly, the Mann-Whitney U test with a p-value threshold for significance of 0.05 was used. Although we test 16 relations, this p-value is justified as we only want to test if the manual and automatic measurements can reproduce known relations. If the aim of this experiments was to find unknown associations of the carotid distensibility, the p-value should be corrected for multiple comparisons. This experiment was only performed using the manual measurements and the 4D registration method. The significant associations found by the automatic method were also verified on a larger dataset.

5.4 Results

5.4.1 Manual measurements

In Figure 5.3 the Bland-Altman plot for manual area measurements is shown. The mean area difference (observer 1 - observer 2) between the two observers is $-2.4\,\mathrm{mm}^2$ ($p < 0.01$) which means that on average the cross-sectional areas annotated by the second observer are larger. The limits of agreement are $-13\,\mathrm{mm}^2$ and $8.8\,\mathrm{mm}^2$.

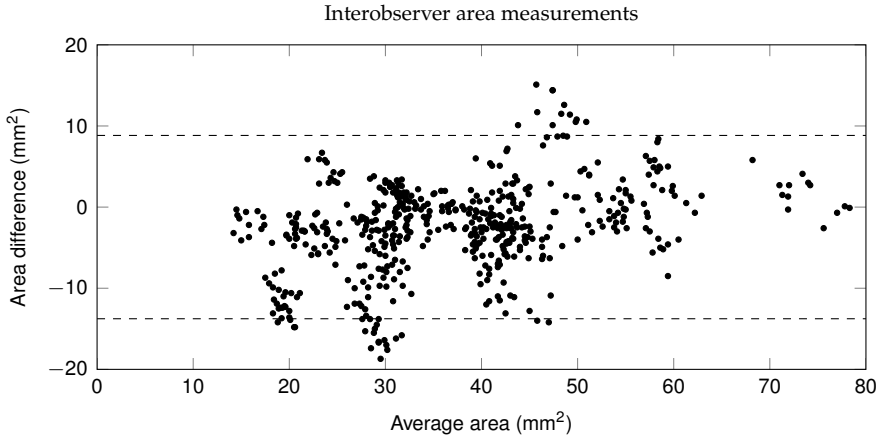

Figure 5.3: Bland-Altman plot of the area measurements on 10 datasets with 13 time points. On the horizontal axis the average area of both observers is shown, the vertical axis shows the difference between both observers in a single area measurement and the dashed lines show the limits of agreement.

Figure 5.3 shows the variation between two observers in measuring a single lumen cross-sectional area. For each patient there are 52 points (left and right, common and internal carotid artery, 13 time points) that are not statistically independent, which causes the clustering in the Bland-Altman plot.

The Bland-Altman plot of the area change ΔA for both observers is shown in Figure 5.4. Here the limits of agreement are $-4.8\,\mathrm{mm}^2$ and $3.4\,\mathrm{mm}^2$. The average area change that was measured by Observer 1 was $5.1\,\mathrm{mm}^2$ and Observer 2 found an average change of $5.8\,\mathrm{mm}^2$ (p=0.03). As can be seen from these graphs, the measured area change $(2 - 8\,\mathrm{mm}^2)$ is within the range of the interobserver variability in measuring lumen area.

5.4.2 Synthetic deformations

Using the synthetically deformed images, we calculated the difference between the expected area change due to the applied scaling and the area change calculated from a circular contour and the deformation field from the registration.

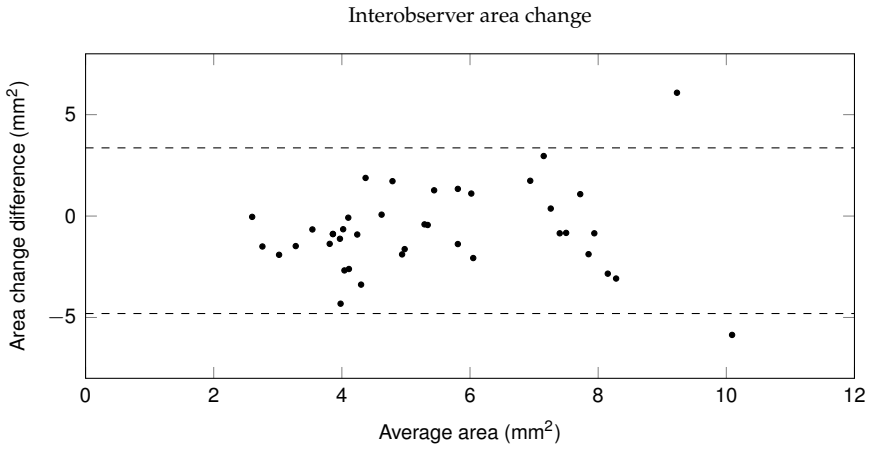

Figure 5.4: Bland-Altman plot of the area change measured by the two observers. On the horizontal axis the average of the area change measured by both observers is shown, the vertical axis shows the difference between the area change measured by both observers and the dashed lines shows the limits of agreement.

control point spacing	Left (mm^2)	Right (mm^2)
1	-0.26 ± 0.34	-0.25 ± 0.23
2	-0.25 ± 0.23	-0.24 ± 0.23
3	-0.33 ± 0.33	-0.32 ± 0.32
4	-0.75 ± 0.48	-0.74 ± 0.48
3D	-0.86 ± 0.17	-0.83 ± 0.15

Table 5.1: Average area measurement errors over all time points for the 3D registration and for for various B-Spline control point spacings in the time dimension of the 4D registration.

Table 5.1 shows the errors in the area measurements for the 3D registration and for different B-spline control point spacings in the time dimension of the 4D registration. The area measurement errors shown in Table 5.1 for a control point spacing of one time point (8% RR-interval) do not differ statistically significantly from the optimal setting of two time points (16 %RR-interval). To minimize the temporal smoothing (see also Section 5.4.4) a control point spacing of 1 time point was used for the 4D registration method.

The algorithms based on 3D and on 4D registration both underestimate the lumen area change. However the error is well below the expected area change of 5.6 mm^2 (Beaussier *et al.*,

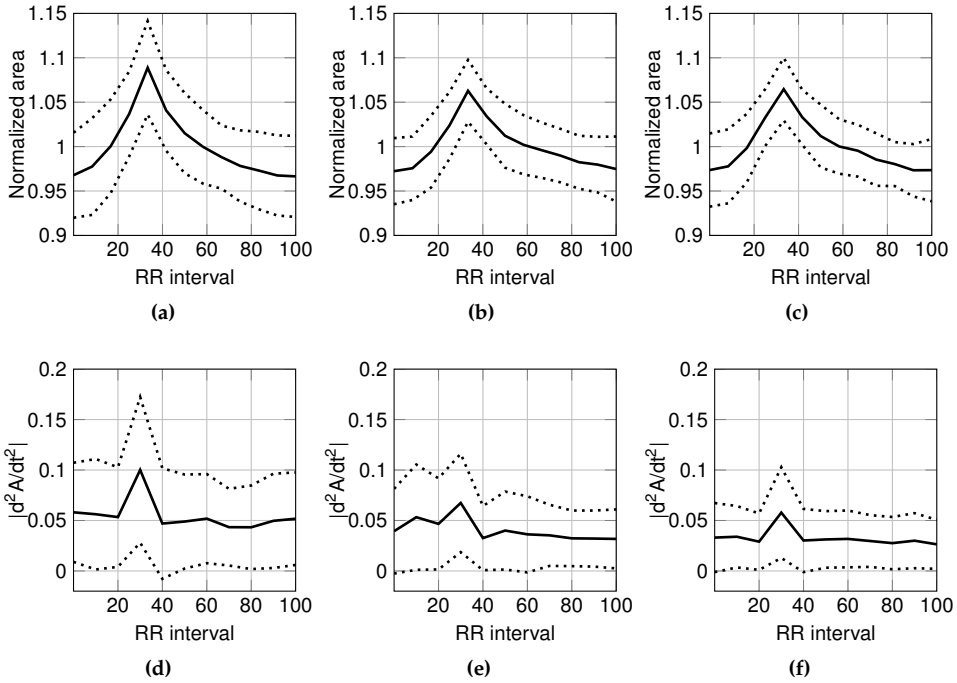

Figure 5.5: Normalized area graphs (top row) and the absolute value of their second order derivative (bottom row) of (a,d) manual measurements, (b,e) automatic measurements using 3D registration and (c,f) 4D registration. The solid lines show the mean curves, the dotted lines represent the mean +/- the standard deviation.

2008)[1], which is an indication that this method can be used to estimate the area change. The p-value of the difference between the errors based on the 3D and the 4D method (paired t-test) was 0.005.

5.4.3 Comparison of automatic and manual measurements

Figure 5.5 shows on the top row a plot of the normalized area curves for the manual measurements, the automatic method using 3D registration, and the automatic method using 4D registration, respectively. The solid line shows the mean curve, the dotted lines show the mean $\pm$ the standard deviation. As can be seen from this figure, the 4D registration based automatic measurements show less variation around the mean curve than manual measurements. The bottom row of Figure 5.5 shows the magnitude of the second order derivative of

[1]The reported CCA mean diameter is 7.857 ± 0.922mm and the reported diameter change is 0.456 ± 0.167mm.

the normalized area curves. From these curves it is clear that the curves of the manual measurements have the highest absolute value and the largest standard deviation while using 4D registration leads to the smallest absolute value of the second order derivative. Thus on average the manual measurements are the most irregular and using 4D registration results in the smoothest curves.

Figure 5.6a, 5.6b and 5.6c show the scatter plots of the manual *vs*. the automatic distensibility measurements for the 3D and 4D method and for the 3D *vs*. the 4D method respectively. The average Pearson correlation coefficient between manual and automatic distensibility measurements was 0.62 for the 3D method and 0.64 for the 4D method. The correlation coefficient between the 3D and the 4D method was 0.90.

Because the 4D method produced slightly smaller errors in the synthetic deformation experiments (Section 5.4.2) and also results in smoother curves, we choose the 4D registration method for the subsequent experiments.

5.4.4 Control point spacing in the t-dimension

In Figure 5.7 the boxplots of the measured distensibility for various values of the control point spacing in the t-dimension of the 4D registration method are shown. Increasing the control point spacing in the t-dimension leads to smoother transformations over time which result in smaller distensibility values. For the subsequent experiments we chose a control point spacing of 8% of the RR-interval. This way the smoothing in the time dimension is minimal.

5.4.5 Influence of spatial and temporal blurring

Table 5.2 shows the effect of spatial and temporal blurring on the measured distensibility. The shown values are the average differences $\mathcal{D}_a$, the average absolute difference $\mathcal{D}_{abs}$, the relative difference $\mathcal{D}_{rel}$:

$$\mathcal{D}_a = \frac{1}{N}\sum_i (\mathcal{D}_{i0} - \mathcal{D}_{i\sigma})$$

$$\mathcal{D}_{abs} = \frac{1}{N}\sum_i |\mathcal{D}_{i0} - \mathcal{D}_{i\sigma}|$$

$$\mathcal{D}_{rel} = \frac{1}{N}\sum_i (\frac{|\mathcal{D}_{i0} - \mathcal{D}_{i\sigma}|}{\mathcal{D}_{i0}})$$

and the Pearson correlation coefficient between $\mathcal{D}_{i0}$ and $\mathcal{D}_{i\sigma}$, where N is the number of measurements, $\mathcal{D}_i 0$ is the distensibility of the ith image measured using the non-blurred image and $\mathcal{D}_{i\sigma}$ is the distensibility measured on the ith image blurred with a Gaussian kernel. As the blurring increases, the difference to the measurements based on the non-blurred image becomes larger. However, the expected movement and registration errors are small and the influence of blurring for small values of σ is very small.

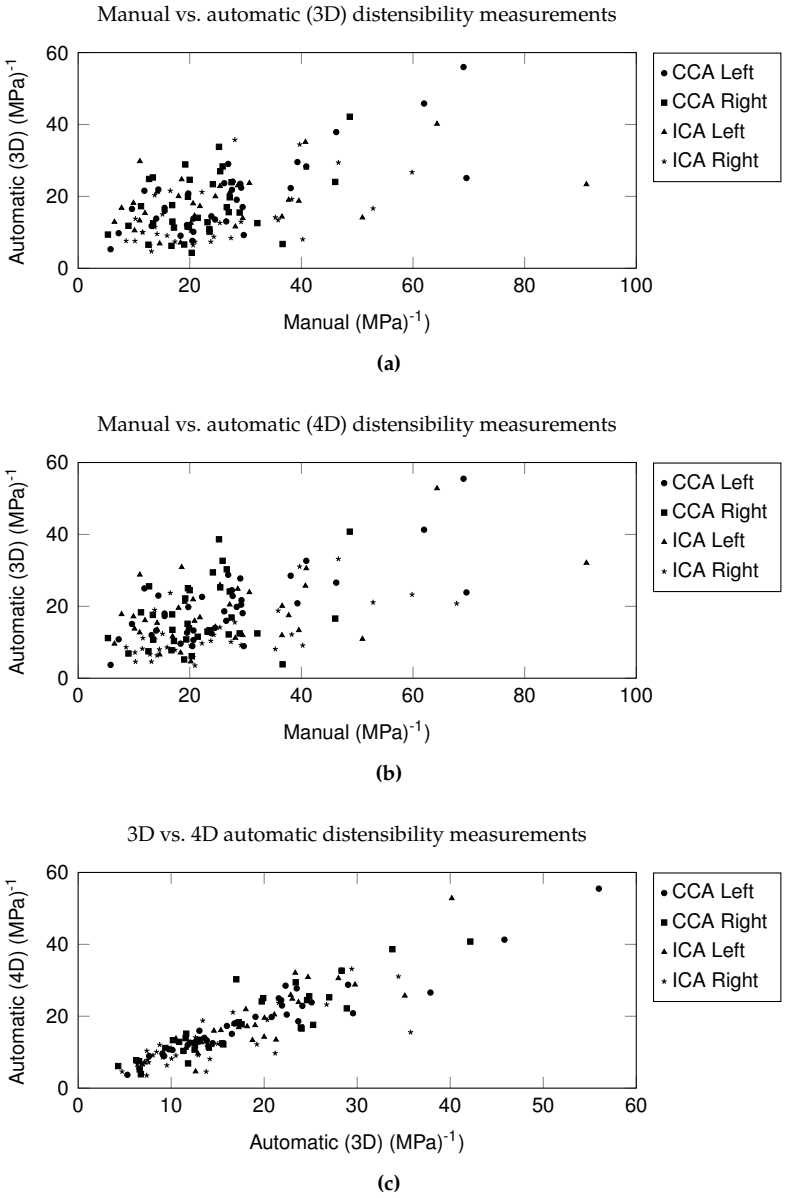

Figure 5.6: Scatterplot of the distensibility measurements of (a) manual and 3D method, (b) manual and 4D method and (c) 3D and 4D method.

	Spatial σ (voxels)				Temporal σ (time points)			
	0.50	1.0	2.0	3.0	0.5	1	2	3
Average difference $(MPa)^{-1}$	-0.15	-0.28	-0.32	-0.24	-0.08	0.20	-0.21	-0.40
Average absolute difference $(MPa)^{-1}$	0.59	1.1	2.0	2.7	0.60	0.95	1.49	1.5
Average relative difference	0.03	0.06	0.12	0.14	0.03	0.05	0.06	0.06
Average correlation coefficient	0.99	0.98	0.94	0.91	0.98	0.93	0.93	0.95

Table 5.2: Average distensibility differences and Pearson correlation coefficient between measurements based on the non-blurred image and when using Gaussian blurring with various values of σ, both for the spatial and the temporal dimension.

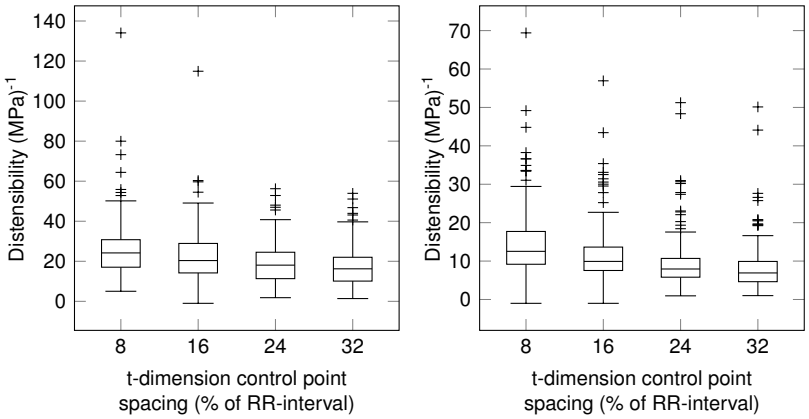

Figure 5.7: Influence of the control point spacing of the 4D registration method in the t-dimension on the measured distensibility of (a) the CCA and (b) the ICA.

5.4.6 Relation with cardiovascular risk factors

In Table 5.3 the median distensibility values and their 95% confidence intervals for both manual and automatic measurements are provided for patients with (gray rows) and without certain cardiovascular risk factors. For the manual measurements, the distensibility of the right ICA for patients who smoke or have smoked was significantly increased (p=0.012). However, the difference between the left and the right (for which no difference between smokers and non smokers was found) is not significant (p=0.6 and p=0.8 for smokers and non smokers respectively). The automatic measurements indicated a lower distensibility of both the right and left CCA for patients suffering from hypertension (p=0.0014 and p=0.0011 for the right and left CCA, respectively).

Table 5.3 shows the results on the 38 datasets for which both manual and automatic measurements were available. Because an additional 38 CTA datasets were available for the automatic method, we repeated measurements on this larger set. For the complete set (n=76) the median distensibility for patients with and without hypertension was 22 $(20-25)$ $(\mathrm{MPa})^{-1}$ and 29 $(25-35)$ $(\mathrm{MPa})^{-1}$ for the left (p=0.018) and 23 $(19-27)$ $(\mathrm{MPa})^{-1}$ and 29 $(25-33)$ $(\mathrm{MPa})^{-1}$ for the right CCA (p=0.024), respectively. All other differences in distensibility remained insignificant.

For each risk factor listed in Table 5.3, the whole group of 38 patients was divided between patients with and without one specific risk factor. This means that the patients in the 'normal group' may very well suffer from one of the other cardiovascular risk factors, which can explain the range of distensibility measurements in the normal groups.

Cardiovascular risk factor	Number of Patients	CCA				ICA			
		Left		Right		Left		Right	
		Manual	Auto	Manual	Auto	Manual	Auto	Manual	Auto
Diabetes	25	26 (21-30)	27 (23-31)	23 (19-27)	27 (24-31)	25 (19-32)	13 (11-17)	23 (18-28)	12 (17-25)
	13	*23 (17-44)*	*21 (15-39)*	*20 (15-25)*	*20 (12-28)*	*21 (15-28)*	*16 (11-25)*	*26 (14-42)*	*9 (20-13)*
Hypercholesterol	9	19 (11-27)	21 (12-38)	21 (14-27)	24 (15-32)	18 (10-28)	11 (8-15)	19 (12-29)	11 (22-9)
	29	*27 (22-34)*	*26 (21-30)*	*22 (19-26)*	*25 (21-30)*	*26 (20-33)*	*15 (12-20)*	*25 (19-33)*	*12 (18-29)*
Hypertension	18	19 (23-39)	**32 (26-41)**	24 (20-29)	**30 (27-34)**	25 (19-33)	15 (11-21)	23 (16-37)	13 (21-18)
	20	*22 (17-27)*	***20 (16-23)***	*19 (16-24)*	***19 (14-24)***	*21 (16-31)*	*13 (10-19)*	*24 (18-30)*	*11 (17-20)*
Smoking	10	25 (17-34)	24 (18-31)	23 (18-33)	27 (21-32)	19 (13-25)	13 (8-23)	**14 (12-33)**	10 (18-11)
	28	*25 (21-31)*	*25 (21-31)*	*21 (18-24)*	*24 (20-29)*	*26 (20-34)*	*14 (11-19)*	***27 (22-33)***	*12 (19-27)*

Table 5.3: Median distensibility values and their confidence intervals in $(\mathrm{MPa})^{-1}$. Patients with listed cardiovascular risk factors are on the italic rows. For the bold numbers the medians of the two groups (with and without risk factor) are significantly different at $p < 0.05$

5.5 Discussion

We investigated the feasibility to determine carotid artery distensibility on 4D CTA using manual measurements and a new registration based automatic method. Beaussier *et al.* (2008) reported a mean diameter in the CCA of 7.875 ± 0.922mm with a diameter change of 0.456 ± 0.167mm. Assuming a circular cross-section, the resulting mean area change is $5.6\,\text{mm}^2$. As can be seen from the Bland-Altman plots in Figure 5.4, this expected area change is smaller than the limits within which the manual area change measurements of the two observers agree. This indicates that manual assessment of the carotid artery distensibility is a difficult task, if feasible at all. This can also be seen in Figure 5.5a which shows a large spread in the normalized graphs, due to measurement errors. This interobserver variability is also noted in the study by Ganten *et al.* (2008) on the aortic distensibility measurements although they do not show any numbers to confirm this. The corresponding automatic measurements (Figure 5.5c) show less variation. Note that this decreased variation in the curves is not due to smoothing caused by the automatic method, because the area changes within one heart cycle of a single patient are still captured.

The large variation in the manual measurements shown in Figure 5.3 and 5.4 also explains the poor correlation with the automatic measurements. This variation may be caused by the fact that the same centerline was used to create the MPRs on all time points. Therefore translations of the carotid artery along the centerline will result in measurements at different physical positions throughout the cardiac cycle. This procedure, however, was also pursued in previous studies on CTA distensibility measurements (Zhang *et al.*, 2007; Ganten *et al.*, 2008; Weber *et al.*, 2009; Xiong and Taylor, 2010; Biesdorf *et al.*, 2011). The online available supplemental material and the movies on the website show the deformation of a carotid artery during one heart cycle which confirms this longitudinal movement. Drawing a centerline at each time point of the RR-interval and creating new MPR images at manually selected corresponding positions could improve the manual procedure but would also make it much more time consuming.

The conclusion that manual lumen annotations are not sufficiently precise to derive distensibility, leaves us with the lack of a good reference standard for evaluating our automatic method. US measurements can neither provide a good reference standard as they assume a circular vessel cross-section, which is not valid in the investigated bifurcation area. To cope with the lack of a reference standard other evaluation methods should be considered. One of these evaluation methods was to use synthetic deformations, in which the true distensibility is known. Although the deformation sizes in our synthetic experiments are realistic the noise realization in both the static and deformed images is the same (they come from the same image). In real practice the noise distribution will be the same for the whole time series of the cardiac cycle (same scanning protocol) but the noise realizations will be different. The synthetic method can still be used to provide an indication of algorithm performance and for algorithm comparison. The experiments using synthetic deformations show that the automatic measurements slightly underestimate the lumen area. This error however is smaller than the desired precision.

Comparing the 4D and 3D registration method we can see that the 4D method produced slightly smaller errors for the experiments using synthetic deformations although the difference is small. The correlation between the 4D method and the manual measurements is a bit higher, but as noted above, the manual measurements are not sufficiently precise to be used as reference standard. The standard variation of the curves for the 4D method is smaller (Figure 5.5b and 5.5c) and the area curves are more smooth (Figure 5.5e and 5.5f). We therefore conclude that the 4D registration method is the preferred method for the automatic distensibility measurements.We investigated the influence of spatial (caused by registration errors and the reconstruction kernel) and temporal (caused by the 4D reconstruction) blurring on the measured distensibility. This influence is small for the relevant blurring scale.

We used a second experiment to evaluate the automatic measurements without using the manually defined reference standard. In this experiment we investigated if the automatic measurements could reproduce known associations of the measured distensibility with general cardiovascular risk factors. The manual measurements show an association between smoking and the distensibility of the right CCA. However, the distribution of these distensibility values is very skewed as can be seen in Table 5.3. The automatic method shows a significant reduction in carotid artery distensibility for patients suffering from hypertension compared to normotensive patients. This relation is consistently found for both the left and right CCA. This relation was not found for the manual measurements. The fact that this observed relation between the cardiovascular risk factors is consistent with literature (Laurent *et al.*, 1994; Liang *et al.*, 2001) supports our conclusion that automatic measurement is more reliable than manual measurement.

5.5.1 Availability of the data

All CTA datasets and the related patient information used in this study are made available through our website (http://ctadist.bigr.nl). Of each patient a 4D CTA image and a description containing the following parameters are available: sex, age, systolic BP, diastolic BP, diabetes, hypercholesterolemia, hypertension, smoking. This data can be used to verify our results or to design a new improved method. For the first 20 subjects also animations are provided of the movement of the carotid artery during a single heart cycle.

5.6 Conclusion

In conclusion, we presented and evaluated two automatic methods for measuring the carotid artery distensibility in 4D CTA data, and evaluated the feasibility of manually performing the same measurements. Our experiments demonstrated that measuring distensibility based on manual lumen annotations is not sufficiently precise, as the variance in the area change measurements is of the same order of magnitude as the expected distensibility area changes. In contrast, the automatic methods show good performance on synthetic data, and were able to reproduce known relations with cardiovascular risk factors, demonstrating that distensibility measurement using our automatic method is feasible.

Acknowledgements

Reinhard Hameeteman, Wiro Niessen and Theo van Walsum were supported by the Stichting voor de Technische Wetenschappen (STW) of The Netherlands Organization for Scientific Research (NWO). Stefan Klein received financial support from the Innovational Research Incentives Scheme of the Netherlands Research Organization (NWO, VENI-Grant 639.021.919)

Chapter 6

Cross-sectional and longitudinal carotid artery wall elasticity measurements on CTA and their relation to cardiovascular risk factors

Based on:

K. Hameeteman, G.P. Zahnd, A. van der Lugt, W.J. Niessen, S. Klein, Cross-sectional and longitudinal carotid artery wall elasticity measurements on CTA and their relation to cardiovascular risk factors, *in preparation*

6.1 Introduction

There is an increase in the prevalence of cardiovascular diseases (CVD), and currently it is the leading cause of death in the western world (Roger *et al.*, 2011). Atherosclerosis, a disease of the vessel wall, is the primary cause of cardiovascular disease. Thickening of the vessel wall due to atherosclerosis may lead to narrowing of the lumen which in turn decreases the blood and oxygen supply proximal to the stenotic region. In the case of the carotid artery this may lead to cerebral ischemic events. Finding parameters that can predict the formation of atherosclerotic plaque is therefore of the utmost importance.

Arterial wall elasticity is considered as biomarker for plaque formation as it is associated with accumulation of atherosclerotic plaque (Newman *et al.*, 1971; Christensen and Neubauer, 1988). The elasticity of the carotid artery can be described by the well established cross-sectional measure distensibility ($\mathcal{D}$), but also by a measure in the direction of the blood flow, the longitudinal deformation ($\mathcal{L}$). The vessel distensibility $\mathcal{D}$ is defined (Laurent *et al.*, 2006) as the maximum change in cross-sectional area during a heart cycle, relative to the pressure change, scaled by the minimum area. $\mathcal{L}$ describes a shearing deformation of the intima-media complex with regard to the adventitia tissues. These vessel wall layers have been shown to undergo a distinct, cyclic and reproducible deformation during the cardiac cycle (Persson *et al.*, 2003).

Traditionally, $\mathcal{D}$ is assessed by acquiring a 2D (B or M-mode) ultrasound (US) image sequence parallel to the centerline of the carotid artery (Van Popele *et al.*, 2001; Pannier *et al.*, 2002) and subsequently measuring the minimum and maximum vessel wall distances during one or more heart cycles. Assuming a circular cross-section, the required area measures are then calculated. Several studies have demonstrated the feasibility of distensibility measurement in large vessels like the aortic arch and abdominal aorta, using ECG-gated CTA (Weber *et al.*, 2009; Ganten *et al.*, 2008; Zhang *et al.*, 2007). An advantage of CTA over ultrasound is that the true cross-sectional area can be measured, and thus non-circular cross-sections can be accounted for. In Chapter 5 we introduced an automated method to measure the carotid distensibility on 4D ECG-gated Computed Tomography Angiography (CTA) images. This study also showed there is a statistically significant relation between the presence of hypertension and the measured distensibility.

In recent years B-mode US imaging has also been used to investigate $\mathcal{L}$ (Ahlgren *et al.*, 2009, 2012; Zahnd *et al.*, 2011) and has been shown to be associated with the presence of cardiovascular risk factors (Ahlgren *et al.*, 2009, 2012; Zahnd *et al.*, 2011). Also it has been shown to be an independent marker from traditional risk markers and providing a better screening potential for very early-stage atherosclerosis, *i.e.* before there is plaque formation (Zahnd *et al.*, 2012). Therefore, despite the fact that $\mathcal{L}$ has gained little attention yet, it constitutes a relevant and complementary risk marker that could improve the characterization of vascular health.

In this study, we aim to investigate the relation between $\mathcal{D}$ and $\mathcal{L}$, and their relation with four cardiovascular risk factors in a study group of patients with ischemic cerebrovascular symptoms. To the best of our knowledge, this is the first study to assess $\mathcal{L}$ in CTA imaging.

CTA imaging seems a well-suited modality for assessing $\mathcal{L}$, as the 3D representation permits to simultaneously assess $\mathcal{L}$ over the entire circumference of the lumen.

The remainder of this paper is organized as follows: Section 6.2 provides the characteristics of the study population and image acquisition protocol, describes the method to measure the $\mathcal{D}$ and $\mathcal{L}$, and explains the statistical analysis. The results of the analysis are presented in Section 6.3. The paper closes with a discussion in Section 6.4.

6.2 Materials and methods

6.2.1 Image acquisition

After Institutional Review Board approval, 81 4D CTA datasets of patients with ischemic cerebrovascular symptoms who underwent CTA of the carotid arteries for clinical workup were acquired. Selection of patients was based on the availability of Dual-source multi-detector CT (DSCT) scanning equipment for this research protocol. All patients (mean age 65 ± 9 y.o.; 48 male, 33 female) gave written informed consent. Scanning was performed on a 64-slice Dual-source multi-detector CT (DSCT) scanner (Siemens, SOMATOM Definition, Forchheim, Germany). First, a non-gated DSCT Angiography (DSCTA) of the carotid arteries was performed which ranged from the aortic arch to the circle of Willis followed by an ECG-gated DSCTA. The ECG-gated DSCTA had a scan range of 40 mm. Scan parameters were: 120 kVp, 150 mAs/rotation, collimation 32×0.6 mm with double sampling in the longitudinal direction, table feed 3.8 - 7.7 mm/rotation, pitch 0.2 - 0.4, in which the pitch and table feed were variable by heart rate. All patients received 80 ml contrast material (Iodixanol 320 mg/ml, Visipaque, Amersham Health, Little Chalfont, UK), followed by 40 ml saline bolus chaser, each at an injection rate of 4 ml/sec. The ECG-gated DSCTA data was used to reconstruct multiphase 4D datasets at 8% steps of the cardiac RR interval, resulting in 13 3D CTA images per patient. Image reconstructions were made with a 12 cm field of view, a matrix size of 512×512 (real in-plane resolution equals 0.4×0.4 mm^2), a slice thickness of 1.0 mm, a reconstruction increment of 0.6 mm and an intermediate (B31f) reconstruction kernel. We excluded six patients because of insufficient image quality and one patient because of the presence of a carotid stent. Blood pressure was measured using an arm cuff during two episodes of continuous measurements. The average of these two measurements was registered and brachial pulse pressure (ΔP) was calculated as the difference between mean systolic and mean diastolic pressure.

We obtained clinical measures and information on risk factors and medication during the patient's visit at the outpatient clinic. Subjects were categorized as ever or never smoking. Hypertension was defined as systolic blood pressure over 140 mm Hg and/or diastolic blood pressure over 90 mm Hg during two episodes of at least 15 minutes of continuous non-invasive blood pressure measurement and/or treatment with antihypertensive medication. Blood-pressure-lowering drugs comprised ACE-inhibitors, calcium-antagonists, beta-blockers, and diuretics. Hypercholesterolemia was defined as fasting cholesterol over 5.0 mmol/l, and/or use of cholesterol-lowering drugs. Diabetes was defined as fasting serum

glucose levels over 7.9 mmol/l, nonfasting serum glucose levels over 11.0 mmol/l, or use of antidiabetic medication.

6.2.2 Measurement method

In this section the definitions of $\mathcal{D}$ and $\mathcal{L}$ are given as well as a description of the method to measure those quantities on 4D CTA data.

The carotid artery distensibility $\mathcal{D}$ is defined (Laurent *et al.*, 2006) as:

$$\mathcal{D} = \frac{\Delta A}{A_{\min} \Delta P} \tag{6.1}$$

where ΔA is difference between the maximal and minimal cross-sectional area during one heart cycle, A_{min} is the minimal cross-sectional area and ΔP is the pulse pressure. $\mathcal{D}$ is averaged over a section of 3.5 mm.

The distensibility measurement of the carotid artery on 4D CTA is based on the method introduced in Chapter 5. This method was extended to also enable assessment of $\mathcal{L}$. Below follows a short description of the original method followed by the modifications. For details about the original method we refer to Chapter 5.

The deformations of the carotid artery during a heart cycle are obtained by combining a 4D registration method (Metz *et al.*, 2011) and a levelset based segmentation method (Manniesing *et al.*, 2010). The 4D registration aligns all cardiac phases of the 4D image and also finds the displacement between these phases. The registered images are combined to create a single 3D image with improved signal-to-noise (SNR) ratio. On this 3D image the carotid lumen border is found by the segmentation method. This segmentation method requires only two seed points to create a complete surface model of the lumen: one in the Common Carotid Artery (CCA) and one in the Internal Carotid Artery (ICA). The VMTK package (Antiga and Steinman, 2004) is then used to robustly find the centerline of the vessel. Cross-sectional planes perpendicular to this centerline are then created at an interval of 0.5 mm. The deformations within the cross-sectional plane are calculated from the displacements as determined by the registration, and the plane normal vector. These deformations lead to the minimal area and maximum area change over a single heart cycle. Together with the pulse pressure, these measurements lead to an estimate of the distensibility of the carotid artery for each position along the centerline.

While the definition of $\mathcal{D}$ is well established, there is no standard measure for $\mathcal{L}$. Therefore we define a measure analogous to $\mathcal{D}$ (see Figure 6.1 for a visualization of this definition). First we compute $\mathcal{L}(\boldsymbol{x}, t)$ for every position $\boldsymbol{x}$ along the centerline and for all cardiac phases t:

$$\mathcal{L}(\boldsymbol{x}, t) = \frac{1}{N \Delta P} \sum_{i=1}^{N} (\boldsymbol{T_i}(\boldsymbol{x}, \boldsymbol{t}) - \boldsymbol{T_i'}(\boldsymbol{x}, \boldsymbol{t})) \cdot \boldsymbol{n}(\boldsymbol{x}) \tag{6.2}$$

the summation is over the N points of a discretized cross-sectional contour (inner circle in Figure 6.1), ΔP is the pulse pressure, $\boldsymbol{T}_i$ is the displacement at position i on the contour with respect to the first phase of the cardiac cycle (arrows of the inner circle in Figure 6.1), $\boldsymbol{T}_i'$

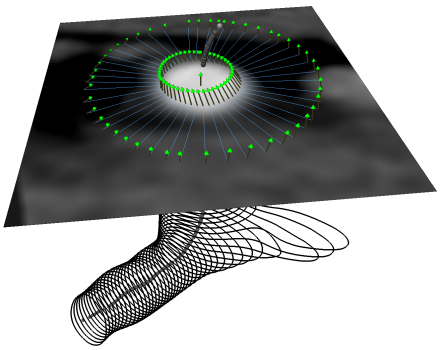

Figure 6.1: Visualization of the movement of the lumen border (inner circle of arrows) and the reference movement (outer circle of arrows) of an expanded (visualized by the lines connecting the two arrow sets) contour. The dots indicate the artery centerline. The shown plane is perpendicular to this centerline. The arrow in the middle of the lumen is the unit normal vector perpendicular to the cross-sectional plane. (vectors are scaled by a factor two for illustration purposes).

is the displacement (outer circle arrows in Figure 6.1) of a reference position (outer circle in Figure 6.1) and $\boldsymbol{n}$ is a unit vector in the direction of the centerline (arrow in the center of Figure 6.1). To obtain the reference positions, the analyzed lumen contour is expanded by 10 mm. For each centerline position $\boldsymbol{x}$ we take the difference between the maximum and minimum value of $\mathcal{L}(\boldsymbol{x}, t)$ over a complete heart cycle and average this difference value over a section of 3.5 mm (seven contours at intervals of 0.5 mm along the centerline):

$$\mathcal{L} = \frac{1}{7}\sum_{i=1}^{7}(\max_{t}(\mathcal{L}(\boldsymbol{x_i}, t)) - \min_{t}(\mathcal{L}(\boldsymbol{x_i}, t))) \tag{6.3}$$

where *max* and *min* are taken over all cardiac phases t. This measure thus reflects the movement of the lumen artery per pressure unit (mm/MPa) with respect to its surrounding tissue in the direction of the centerline during one heart cycle.

For each patient four measurement are made of both $\mathcal{D}$ and $\mathcal{L}$: proximal to the bifurcation in the right and left CCA, and approximately 1 cm distal to the bifurcation in the right and left ICA. Both CCA as well as both ICA measurements are averaged, resulting in two $\mathcal{D}$ and $\mathcal{L}$ measurements per patient.

6.2.3 Statistical Analysis

The correlation between the CCA and ICA measurements and between $\mathcal{D}$ and $\mathcal{L}$ is investigated using the Pearson correlation coefficient. For $\mathcal{D}$ and $\mathcal{L}$ also the scatter plots of both the CCA and ICA measurements are made.

In order to assess the relation of $\mathcal{D}$ and $\mathcal{L}$ with cardiovascular risk factors, a general linear model (Mardia *et al.*, 1979) is applied. For the aorta the elasticity is known to be decreasing with age, and differs between male and female (Rose *et al.*, 2010; Natoli *et al.*, 2005; Waddell

	Absent				Present			
Risk factor	♂	♀	age	ΔP	♂	♀	age	ΔP
Diabetes	31	19	64.0	55 ± 13	12	11	63.3	61 ± 14
Hypercholesterolemia	11	5	65.3	55 ± 14	32	25	63.4	57 ± 14
Hypertension	20	12	62.7	52 ± 11	23	18	64.6	61 ± 15
Smoking	9	14	67.1	56 ± 10	34	16	62.3	57 ± 15

Table 6.1: Distribution of the patients over the the two groups (Absent and Present) for the different risk factors, as well as mean age and pulse pressure in mm Hg $\pm$ standard deviation.

et al., 2001). Because we expect the same effect for the carotid artery, we use the age and sex of patients as covariates in our analysis. In a first experiment we use a basic model considering only age and sex as covariates. In a second experiment we apply an extended model in which all other risk factors are used as covariates, besides age and sex.

To test the normality assumption a visual inspection of the measurement histograms is performed followed by a Shapiro-Wilk test (Shapiro and Wilk, 1965) and if necessary the distribution is normalized through an appropriate data transformation. For both the $\mathcal{D}$ and $\mathcal{L}$, outliers are identified based on the outlier labeling rule (Hoaglin and Iglewicz, 1987). The measurements of a patient are removed if the CCA and/or ICA measurement falls outside the interval $[Q1 - 2.2(Q3 - Q1), Q3 + 2.2(Q3 - Q1)]$, where $Q1$ and $Q3$ are the higher end of the first and third quartile respectively. The descriptive power of the predictors in the extended model is tested by inspection of the scatter plots and the Pearson correlation coefficients of $\mathcal{D}$ and $\mathcal{L}$ *vs.* their predicted values $\hat{\mathcal{D}}$ and $\hat{\mathcal{L}}$ for both the CCA and ICA measurements.

All statistical analyses are carried out using SPSS version 20.

6.3 Results

According to the Shapiro-Wilk test the outcome measures $\mathcal{D}$ and $\mathcal{L}$ are not normally distributed. To normalize the distribution of the measurements the logarithm (base 10) is taken. Based on the outlier labeling rule the measurements of one patient are removed. Table 6.1 shows how the patient group is distributed over the different risk factors. In Table 6.2 the means and standard deviations of the original CCA and ICA measurements are shown for each of the risk factors while ignoring the other risk factors. The log transformed measurements are shown in Table 6.3. The Pearson correlation coefficients of $\log(\mathcal{D})$ and $\log(\mathcal{L})$ for the CCA and ICA measurements are given in Table 6.4. Figure 6.2 visualizes the relation between $\log(\mathcal{D})$ and $\log(\mathcal{L})$ for the CCA and ICA.

The left side of Table 6.5 shows the p-values from the basic model. In these tests there are two statistically significant ($p < 0.05$) results for the $\log(\mathcal{D})$ measurements of the CCA. There is a statistically significant difference in mean $\log(\mathcal{D})$ for patients suffering from diabetes and/or hypertension. From Table 6.2 we can see that $\mathcal{D}$ in the CCA is smaller for patients with these risk factors. The right side of Table 6.5 shows the p-values for the extended model.

		$\mathcal{D}$ $(1/MPa)$				$\mathcal{L}$ (mm/MPa)			
		Absent		Present		Absent		Present	
	Risk factor	μ	σ	μ	σ	μ	σ	μ	σ
CCA	Diabetes	26	11	23	14	42	41	35	18
	Hypercholesterolemia	24	16	25	11	43	49	39	31
	Hypertension	29	14	22	10	50	49	32	15
	Smoking	23.0	8.2	26	14	40	43	39	32
ICA	Diabetes	14.0	8.7	14.4	6.4	48	25	51	35
	Hypercholesterolemia	13.0	6.5	14.5	8.4	44	25	50	29
	Hypertension	15.3	7.9	13.3	8.1	51	25	48	31
	Smoking	11.9	5.1	15.2	8.9	38	12	54	32

Table 6.2: Means (μ) and standard deviations (σ) of $\mathcal{D}$ and $\mathcal{L}$ measurements in the CCA and ICA for the two groups of each of the risk factors (Absent and Present).

		$\log(\mathcal{D})$ $(-log(MPa))$				$\log(\mathcal{L})$ $(log(mm/MPa))$			
		Absent		Present		Absent		Present	
	Risk factor	μ	σ	μ	σ	μ	σ	μ	σ
CCA	Diabetes	1.38	0.17	1.29	0.25	1.50	0.30	1.49	0.24
	Hypercholesterolemia	1.31	0.25	1.36	0.19	1.49	0.32	1.50	0.27
	Hypertension	1.42	0.19	1.30	0.19	1.56	0.32	1.45	0.23
	Smoking	1.34	0.15	1.35	0.22	1.49	0.26	1.50	0.29
ICA	Diabetes	1.08	0.23	1.12	0.21	1.63	0.23	1.63	0.24
	Hypercholesterolemia	1.08	0.18	1.10	0.23	1.57	0.26	1.64	0.22
	Hypertension	1.14	0.19	1.06	0.23	1.66	0.22	1.61	0.24
	Smoking	1.04	0.17	1.12	0.23	1.56	0.15	1.66	0.26

Table 6.3: Means (μ) and standard deviations (σ) of $\log(\mathcal{D})$ and $\log(\mathcal{L})$ measurements in the CCA and ICA for the two groups of each of the risk factors (Absent and Present).

With this extended model only the result for the $\mathcal{D}$ measurement of the CCA in relation to the presence of hypertension remains statistically significant.

Figure 6.3 shows a scatter plot of the predicted versus the measured elasticity parameters and their Pearson correlation coefficients, using the extended model for prediction of measurements based on cardiovascular risk factors, age and sex.

	1.	2.	3.	4.
1. log($\mathcal{D}$) CCA	1.0			
2. log($\mathcal{D}$) ICA	0.53	1.0		
3. log($\mathcal{L}$) CCA	0.55	0.35	1.0	
4. log($\mathcal{L}$) ICA	0.46	0.48	0.38	1.0

Table 6.4: Pearson correlation coefficients between the log($\mathcal{D}$) and log($\mathcal{L}$) measurements of the CCA and ICA.

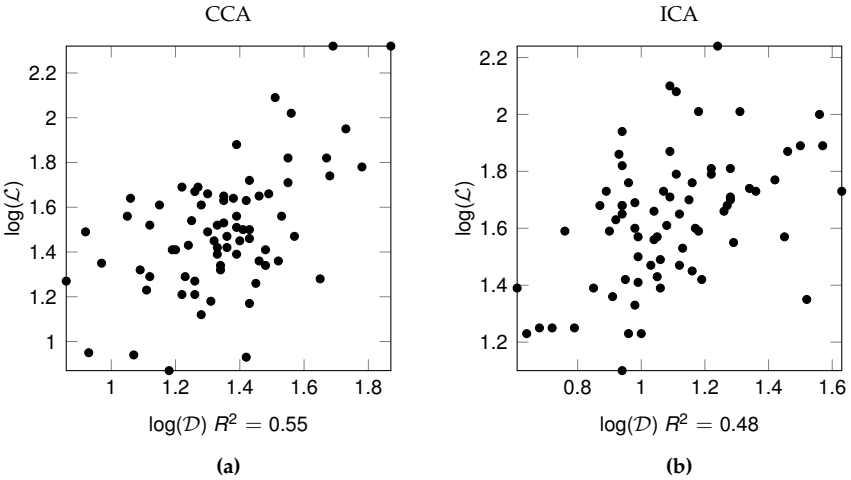

Figure 6.2: Scatterplot of log($\mathcal{L}$) in $(log(mm/MPa))$ *vs.* log($\mathcal{D}$) in $-log(MPa)$ for the (a) CCA and (b) ICA.

6.4 Discussion

In this paper we presented a method to measure the carotid artery wall elasticity in the radial and longitudinal direction, *i.e.* the distensibility ($\mathcal{D}$) and longitudinal deformation ($\mathcal{L}$). Both these measures were calculated in an automated fashion from 4D ECG gated CTA images. We investigated the relation between $\mathcal{D}$ and $\mathcal{L}$ and between both measures and four cardiovascular risk factors.

The mean measured $\mathcal{L}$ in the study population as shown in Table 6.2 was comparable to the average from previous studies (Ahlgren *et al.*, 2009, 2012; Zahnd *et al.*, 2011, 2012). There is a moderate correlation between the $\mathcal{D}$ and $\mathcal{L}$ measurements ($R^2 \approx 0.5$). The moderate correlation between $\mathcal{D}$ and $\mathcal{L}$ supports previous work showing that $\mathcal{L}$ is an independent predictor for atherosclerosis (Zahnd *et al.*, 2012).

We found a statistically significant relation between hypertension and the distensibility of the common carotid artery: patients suffering from hypertension on average have a reduced

	Basic model				Extended model			
	$\log(\mathcal{D})$		$\log(\mathcal{L})$		$\log(\mathcal{D})$		$\log(\mathcal{L})$	
risk factor	CCA	ICA	CCA	ICA	CCA	ICA	CCA	ICA
Diabetes	**0.044**	0.60	0.71	0.97	0.14	0.43	0.92	0.93
Hypercholesterolemia	0.51	0.84	0.89	0.37	0.088	0.49	0.66	0.20
Hypertension	**0.014**	0.21	0.10	0.49	**0.016**	0.095	0.10	0.22
Smoking	0.89	0.56	0.88	0.19	0.67	0.52	0.91	0.14

Table 6.5: Significance values for the basic and extended model. The statistically significant ($p<0.05$) values are shown in bold font.

distensibility, i.e. they have stiffer vessels. This association confirms the results that were reported in Chapter 5, where the statistical analysis was based on multiple Mann-Whitney-U tests, not correcting for multiple comparisons, age and sex. In the current work we used age and sex as covariates and also tested if the association hold when using all remaining risk factors as covariates.

Although not statistically significant in our population, inspecting the mean values in Table 6.2 reveals that there may be a small effect of CCA hypertension in relation to $\mathcal{L}$. In Table 6.5 this relation also has the smallest p-value of all test for $\mathcal{L}$ for both the basic and extended model.

The capability of the total model to predict $\mathcal{D}$ and $\mathcal{L}$ is shown in Figure 6.3. From this figure it can be concluded that $\mathcal{D}$ is better predictable from the used cardiovascular risk factors, age and sex than $\mathcal{L}$. Also the correlation of $\mathcal{D}$ and $\hat{\mathcal{D}}$ is larger for the CCA than for the ICA.

The patients in this study all had ischemic cerebrovascular symptoms, therefore the conclusions may not generalize to another population. This makes it difficult to compare the results of this study to previous studies in which a difference in $\mathcal{L}$ for patients with and without diabetes was found (Zahnd *et al.*, 2011). The "control" group for the non-diabetic patients in our study were not healthy subjects, which may be the cause of no statistically significant difference in mean $\mathcal{L}$ between the groups.

Another cause of the discrepancy with Zahnd *et al.* (2011) may be the use of CTA *vs*. US. The order of magnitude of the assessed longitudinal deformation has been reported to be one millimeter, estimated *in vivo* with high accuracy in US B-mode imaging using an experimental setup (Cinthio *et al.*, 2005) as well as on a larger clinical database (Zahnd *et al.*, 2013). The resolution of the CTA images was $0.4 \times 0.4 \times 1.0$ mm^3 which is much coarser than what can be achieved using B-mode US, where the pixel size is usually around 30 μm^2. The lower resolution of the CTA images as compared to the US makes it much harder to capture small deformations described by $\mathcal{L}$.

For smaller vessels, the magnitude of $\mathcal{D}$ and $\mathcal{L}$ also becomes smaller, and it is more difficult to quantify them. This may explain the lack of statistically significant results for all ICA measurements as this artery is smaller than the CCA.

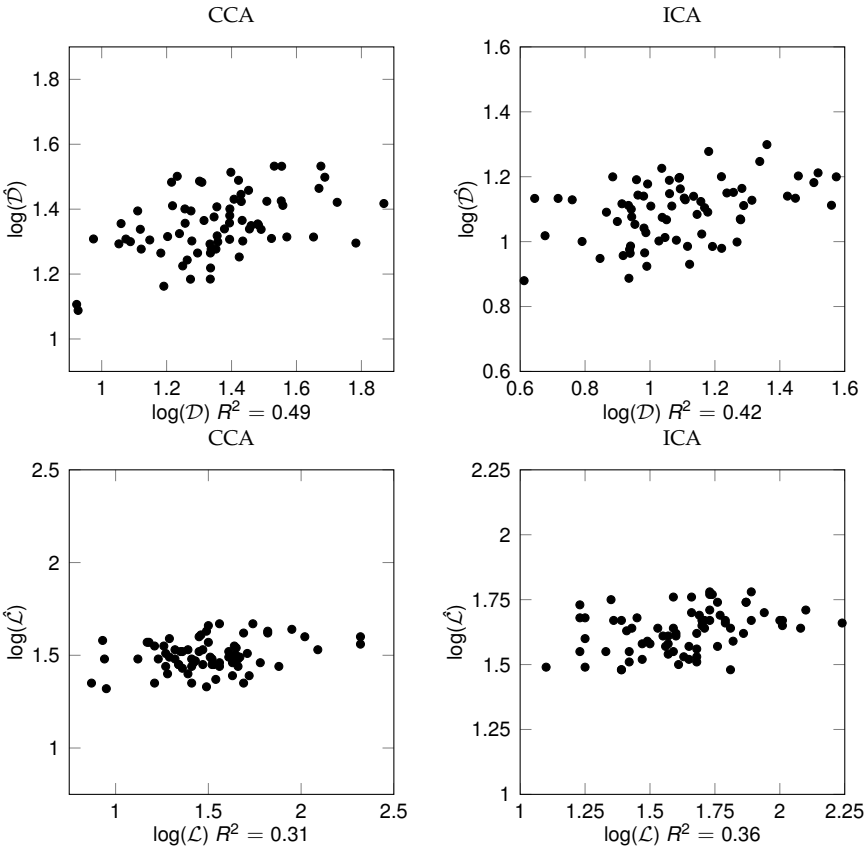

Figure 6.3: Scatterplot of log($\hat{\mathcal{D}}$) *vs.* log($\mathcal{D}$) in $-log(MPa)$ on the top row and log($\hat{\mathcal{L}}$) *vs.* log($\mathcal{L}$) in $(log(mm/MPa))$ on the bottom row for the CCA (left column) and ICA (right column), respectively.

The method to measure $\mathcal{D}$ described in this study may be used to perform automated measurements to assess the carotid artery elasticity. The results from this study also suggest that a higher spatial resolution is required to assess $\mathcal{L}$, which can be achieved using US. Future work should focus on comparison of CTA and US to investigate which modality results in more accurate elasticity measurements.

In conclusion, we presented a method to measure the distensibility and longitudinal deformations of the carotid artery on CTA image. The study described in this paper confirms the previously found relation between hypertension and carotid artery distensibility in a more thorough statistical analysis. For the longitudinal deformations we measured values that are comparable to those reported in previous studies with US, but we could not confirm, in our population, previously reported associations with cardiovascular risk factors.

Chapter 7

Summary and discussion

7.1 Summary

Medical imaging techniques such as magnetic resonance imaging (MRI) and computed tomography (CT) play an important role in the diagnosis and treatment of cardiovascular disease. Extraction of quantitative measures, which are related to the presence or state of the disease, is important to optimally exploit the information that is present in the image. Objective analysis of MRI and CT images can be achiefed efficiently by using automated analysis techniques. Relevant quantitative measures derived from images are called quantitative imaging biomarkers (QIBs). In this thesis we present and evaluate several methods to measures QIBs related to atherosclerosis of the carotid artery.

The first QIB that is considered in this thesis is lumenal stenosis. In **Chapter 2** the state-of-the-art CT angiography (CTA) techniques are described. Using CTA blood vessels can be imaged. From these images the degree of stenosis and the increase of the wall volume caused by atherosclerosis can be determined using (semi)automated analysis software. This enables studying different disease stages without any surgical intervention. In **Chapter 3** an evaluation framework that allows a standardized, objective and quantitative comparison of carotid artery lumen segmentation and stenosis grading algorithms is presented. The basis of such a freamework is a representative set of imaging data with an accurate estimate of the QIB to be extracted (reference standard). We described the data repository comprising 56 multi-center, multi-vendor CTA datasets, the creation of the reference standard and the evaluation measures. This framework has been introduced at the MICCAI 2009 workshop *3D Segmentation in the Clinic: A Grand Challenge III*. We compared the results of eight teams that participated in this challenge. These results show that automated segmentation of the vessel lumen is possible with a precision that is comparable to manual annotation. Although (semi)automated stenosis grading is a logical next step after lumen segmentation, this step is seldomly made. The results of the three teams that submitted semi-automated stenosis grading showed that manual measurements is still much more precise. The framework is open for new submissions through the website http://cls2009.bigr.nl. To date 14 teams have submitted lumen segmentation results and three teams have submitted stenosis grading results. In **Chapter 4** we presented and evaluated a method for carotid vessel wall volume quantification on MRI data. The method for lumen and outer wall segmentation combines two segmentation techniques: one based on "deformable models" and a correction step based on pattern recognition techniques. After selecting two initialization points, the vessel wall volume in a region around the bifurcation is automatically determined. The method was trained on eight datasets (16 carotids) from a population based study in the elderly. For this training set one observer manually annotated both the lumen and outer wall. Evaluation was performed on a separate set of 19 datasets (38 carotids) from the same study for which two observers made manual annotations. On the test set Wall volume and normalized wall index measurements resulting from the manual annotations were compared to the automatic measurements. Our experiments show that the results of the automated method are comparable to the manual measurements. All image data and annotations used in this study together with the measurements are publicly available through the website .

In **Chapter 5** the focus shifted to carotid artery distensibility, a measure for the elasticity of the vessel wall. In this chapter we investigated the feasibility of measuring carotid artery distensibility on 4D CTA. We investigated this for both manual measurements (38 images) and using automated methods (76 images). On a subset (10 images) of the manual measurements a second observer performed manual measurements. The inter-observer variability was assessed using a Bland-Altman analysis. Since the inter-observer variability was very large, we concluded that the distensibility cannot reliably measured using manual annotation. We compared two versions of the automatic method: one using 3D registration and one using a 4D registration method. The latter resulted in more smooth deformations over time. The automatic method was evaluated using a synthetic deformation and by investigating whether known relations with cardiovascular risk factors could be reproduced. The relation between the distensibility and cardiovascular risk factors was tested with a Mann-Whitney U test. Automatic measurements revealed an association with hypertension whereas the manual measurements did not. This relation has also been found in previous studies. We conclude that carotid artery distensibility measurements should be performed automatically and that the method described in this chapter is suitable for that. All CTA datasets and related clinical data used in this study can be downloaded from our website (http://ctadist.bigr.nl). In **Chapter 6** we further analyzed the relation between cardiovascular risk factors and carotid artery wall elasticity. Besides the distensibility, in this Chapter we investigated the longitudinal deformation. For the measurements of this deformation in the direction of the centerline we also presented an automated method. The relation with the following cardiovascular risk factors was analyzed: diabetes, hypercholesterolemia, hypertension and smoking. Traditionally, both the distensibility and the longitudinal deformations are measured using ultrasound. In this study we investigated the possibility to measure these quantities using CTA imaging data. CTA images have the advantage that they allow fully three-dimensional measurements. We analyzed the distensibility and longitudinal deformations in 81 patients with ischemic cerebrovascular symptoms, and investigated their relation with the four mentioned cardiovascular risk factors. For each risk factor, statistical analyses were performed with a general linear model, using i) a basic model considering only age and sex as covariates, and ii) an extended model considering age, sex, and the other risk factors as covariates. We found a moderate correlation between the distensibility and the longitudinal deformations of around 0.5. The average distensibility was $24 \pm 1\,(MPa)^{-1}$ (mean $\pm$ standard deviation) in the CCA and $14.2 \pm 0.9\,(MPa)^{-1}$ in the ICA. The longitudinal deformations were $40 \pm 35\,mm/MPa$ in the common carotid artery and $49 \pm 28\,mm/MPa$ in the internal carotid artery. We found a statistically significant decrease in the mean distensibility of the common carotid artery for patients suffering from hypertension. This relation remained significant after correction for age, sex and the other three investigated risk factors. No significant associations of the longitudinal deformations with any of the cardiovascular risk factors were found.

7.2 Discussion

The purpose of the research presented in this thesis was to develop and evaluated methods for the automated measurement of QIBs for atherosclerosis of the carotid artery in order to reduce the required manual labor and eliminate the inter- and intra-observer variability. While not fully automatic, the methods presented in this thesis require only two or three mouse clicks. Manual measurements of the presented quantitative imaging biomarkers would require drawing many (*i.e.* tens to hundreds) contours. The limited amount of user interaction makes the presented methods suitable for large scale analysis and makes the introduction of these QIBs in epidemiological studies and clinical trails feasible. Such large studies would enable further evaluation of the diagnostic value of the measured imaging biomarkers.

The evaluations presented in this thesis show that automated measurement can approach or even exceed the precision of the manual measurements. The best lumen segmentation method discussed in Chapter 3 has a Dice coefficient which is larger and a mean surface distance which is smaller than the average variation between the three manual annotations. The results from Chapter 5 show that the variation in manual annotations is too large to be able to measure the subtle changes in cross-sectional area of the carotid during a heart cycle. As shown in this chapter the automated method appears to be able to capture these small deformations.

All studies described in this thesis had a cross-sectional setup. To study the value of the presented QIBs for e.g. the prediction of the progression of carotid artery atherosclerosis a longitudinal study design would be required. Except for the imaging data of the evaluation framework presented in Chapter 3 all study populations presented in this thesis were single center and single vendor. Multi-center and multi-vendor experiments would be required to be able to port these methods into clinically usable products.

One of the key characteristics of scientific research is reproducibility. If a scientific experiment is not repeatable it is not differentiable from miracles or legends Ibanez and Schroeder (2010). This reproducibility should first of all be possible for the researcher himself. For research fields in which the implementation of a scientific method plays an important role in gathering the results, maintaining a well organized source code repository is essential to be able to achieve this reproducibility. In principle the publication of a method in a scientific journal should suffice for the reader to make his own implementation. But to reproduce the presented results also the data is needed. Researchers in the field of biomedical image processing often are not the owner for the data on which they develop their algorithms, but sharing of data should be advocated as much as possible Johnson *et al.* (2006).

The data used in the studies presented in this thesis have been made publicly available through various websites. This enables other researcher to reproduce our results and encloses an invitation to improve on them, and to compare with the results of other methods.

References

Abegunde, D., Beaglehole, R., Durivage, S., Epping-Jordan, J., Mathers, C., Shengelia, B., Strong, K., Tukuitonga, C. and Unwin, N. *Preventing chronic disease: a vital investment*. World Health Organization, 2005.

Agatston, A.S., Janowitz, W.R., Hildner, F.J., Zusmer, N.R., Viamonte, Jr, M. and Detrano, R. Quantification of coronary artery calcium using ultrafast computed tomography. *Journal of the American College of Cardiology*, 3 1990. 15(4):827–832.

Ahlgren, Å., Cinthio, M., Steen, S., Nilsson, T., Sjöberg, T., Persson, H. and Lindström, K. Longitudinal displacement and intramural shear strain of the porcine carotid artery undergo profound changes in response to catecholamines. *American Journal of Physiology - Heart and Circulatory Physiology*, 2012. 302(5):H1102–H1115.

Ahlgren, Å., Cinthio, M., Steen, S., Persson, H., Sjöberg, T. and Lindström, K. Effects of adrenaline on longitudinal arterial wall movements and resulting intramural shear strain: a first report. *Clinical Physiology and Functional Imaging*, 2009. 29(5):353–359.

Antiga, L. and Steinman, D.A. Robust and objective decomposition and mapping of bifurcating vessels. *IEEE Transactions on Medical Imaging*, 6 2004. 23(6):704–713.

Arfken, G.B. and Weber, H.J. *Mathematical Methods for Physicists, Sixth Edition: A Comprehensive Guide*. Academic Press, 6 edition, 7 2005.

Azencot, J. and Orkisz, M. Deterministic and stochastic state model of right generalized cylinder (RGC-sm): application in computer phantoms synthesis. *Graphical Models*, 2003. 65(6):323–350.

Baltaxe Milwer, M., Flórez Valencia, L., Hernández Hoyos, M., Magnin, I.E. and Orkisz, M. Fast-marching contours for the segmentation of vessel lumen in cta cross-sections. In *Engineering in Medicine and Biology Society, 2007. EMBS 2007. 29th Annual International Conference of the IEEE*. 8 2007 pages 791 –794. Slice-based.

Beaussier, H., Masson, I., Collin, C., Bozec, E., Laloux, B., Calvet, D., Zidi, M., Boutouyrie, P. and Laurent, S. Carotid plaque, arterial stiffness gradient, and remodeling in hypertension. *Hypertension*, 10 2008. 52(4):729–736.

Beitzke, D., Wolf, F., Edelhauser, G., Plank, C., Schernthaner, R., Weber, M., Nolz, R., Lammer, J. and Loewe, C. Computed tomography angiography of the carotid arteries at low kv settings: a prospective randomised trial assessing radiation dose and diagnostic confidence. *European Radiology*, 11 2011. 21(11):2434–2444.

Berg, M., Zhang, Z., Ikonen, A., Manninen, H. and Vanninen, R. Carotid stenosis assessment with ct angiography using advanced vessel analysis software. *International Congress Series*, 2005. 1281:322 – 327. CARS 2005: Computer Assisted Radiology and Surgery.

Biesdorf, A., Wörz, S., Müller, T., Weber, T., Heye, T., Hosch, W., von Tengg-Kobligk, H. and Rohr, K. Model-based segmentation and motion analysis of the thoracic aorta from 4dǎecg-gated cta images. In G. Fichtinger, A. Martel and T. Peters, editors, *Medical Image Computing and Computer-Assisted Intervention - MICCAI 2011*, volume 6891 of *Lecture Notes in Computer Science*, pages 589–596. Springer Berlin / Heidelberg, 2011.

Binaghi, S., Maeder, P., Uské, A., Meuwly, J.Y., Devuyst, G. and Meuli, R.A. Three-dimensional computed tomography angiography and magnetic resonance angiography of carotid bifurcation stenosis. *European Neurology*, 2001. 46(1):25–34.

Bossuyt, P.M., Reitsma, J.B., Bruns, D.E., Gatsonis, C.A., Glasziou, P.P., Irwig, L.M., Lijmer, J.G., Moher, D., Rennie, D., De Vet, H.C.W. and Standards for Reporting of Diagnostic Accuracy. Towards complete

and accurate reporting of studies of diagnostic accuracy: the stard initiative. *Clinical Radiology*, 8 2003. 58(8):575–580.

Brinkmann, B., Manduca, A. and Robb, R. Optimized homomorphic unsharp masking for mr grayscale inhomogeneity correction. *IEEE Transactions on Medical Imaging*, 4 1998. 17(2):161–171.

Cademartiri, F., Mollet, N.R., Runza, G., Bruining, N., Hamers, R., Somers, P., Knaapen, M., Verheye, S., Midiri, M., Krestin, G.P. and De Feyter, P.J. Influence of intracoronary attenuation on coronary plaque measurements using multislice computed tomography: observations in an ex vivo model of coronary computed tomography angiography. *European Radiology*, 7 2005. 15(7):1426–1431.

Cademartiri, F., Van der Lugt, A., Luccichenti, G., Pavone, P. and Krestin, G.P. Parameters affecting bolus geometry in cta: a review. *Journal of Computer Assisted Tomography*, 2002. 26(4):598–607.

Catmull, E. and Rom, R. A class of local interpolating splines. *Computer Aided Geometric Design*, 1974. pages 317–326.

Chan, T. and Vese, L. Active contours without edges. *IEEE Transactions Image Processing*, 2001. 10(2):266–277.

Chappell, F.M., Wardlaw, J.M., Young, G.R., Gillard, J.H., Roditi, G.H., Yip, B., Pell, J.P., Rothwell, P.M., Brown, M.M., Gough, M.J. and Randall, M.S. Carotid artery stenosis: accuracy of noninvasive tests–individual patient data meta-analysis. *Radiology*, 5 2009. 251(2):493–502.

Christensen, T. and Neubauer, B. Increased arterial wall stiffness and thickness in medium-sized arteries in patients with insulin-dependent diabetes mellitus. *Acta Radiologica*, 1988. 29(3):299–302.

Cinthio, M., Ahlgren, Å., Jansson, T., Eriksson, A., Persson, H. and Lindström, K. Evaluation of an ultrasonic echo-tracking method for measurements of arterial wall movements in two dimensions. *IEEE Transactions on Ultrasonics, Ferroelectrics, and Frequency Control*, 2005. 52(8):1300–1311.

Cohen, M., DuBois, R. and Zeineh, M. Rapid and effective correction of rf inhomogeneity for high field magnetic resonance imaging. *Human Brain Mapping*, 8 2000. 10(4):204–211.

Cuisenaire, O. Fully automated segmentation of carotid and vertebral arteries from CTA. In *The Midas Journal*. 2009 .

Cuisenaire, O., Virmani, S., Olszewski, M.E. and Ardon, R. Fully automated segmentation of carotid and vertebral arteries from contrast enhanced cta. In J.M. Reinhardt and J.P.W. Pluim, editors, *Medical Imaging 2008: Image Processing*, volume 6914. SPIE, 2008 page 69143R.

De Koning, P., Schaap, J., Janssen, J., Westenberg, J., Van der Geest, R. and Reiber, J. Automated segmentation and analysis of vascular structures in magnetic resonance angiographic images. *Magnetic Resonance in Medicine*, 12 2003. 50(6):1189–1198.

De Monyé, C., De Weert, T.T., Zaalberg, W., Cademartiri, F., Siepman, D.A.M., Dippel, D.W.J. and Van der Lugt, A. Optimization of ct angiography of the carotid artery with a 16-mdct scanner: craniocaudal scan direction reduces contrast material-related perivenous artifacts. *American Journal of Roentgenology*, 6 2006. 186(6):1737–1745.

De Weert, T.T., Cretier, S., Groen, H.C., Homburg, P., Cakir, H., Wentzel, J.J., Dippel, D.W.J. and Van der Lugt, A. Atherosclerotic plaque surface morphology in the carotid bifurcation assessed with multidetector computed tomography angiography. *Stroke*, 4 2009. 40(4):1334–1340.

De Weert, T.T., De Monyé, C., Meijering, E., Booij, R., Niessen, W.J., Dippel, D.W.J. and Van der Lugt, A. Assessment of atherosclerotic carotid plaque volume with multidetector computed tomography angiography. *International Journal of Cardiovascular Imaging*, 10 2008. 24(7):751–759.

De Weert, T.T., Ouhlous, M., Meijering, E., Zondervan, P.E., Hendriks, J.M., Van Sambeek, M.R.H.M., Dippel, D.W.J. and Van der Lugt, A. In vivo characterization and quantification of atherosclerotic carotid plaque components with multidetector computed tomography and histopathological correlation. *Arteriosclerosis, Thrombosis, and Vascular Biology*, 10 2006. 26(10):2366–2372.

De Weert, T.T., Ouhlous, M., Zondervan, P.E., Hendriks, J.M., Dippel, D.W.J., Van Sambeek, M.R.H.M. and Van der Lugt, A. In vitro characterization of atherosclerotic carotid plaque with multidetector computed tomography and histopathological correlation. *European Radiology*, 9 2005. 15(9):1906–1914.

Dehnavi, R., Doornbos, J., Tamsma, J., Stuber, M., Putter, H., der Geest, R.V., Lamb, H. and Roos, A.D. Assessment of the carotid artery by MRI at 3T: a study on reproducibility. *Journal of Magnetic Resonance Imaging*, 5 2007. 25(5):1035–1043.

Deshpande, J.V., Gore, A.P. and Shanubhogue, A. *Statistical Analysis of Nonnormal Data*. Wiley-Interscience, 1995.

Dice, L.R. Measures of the amount of ecologic association between species. *Ecology*, 7 1945. 26(3):297–302.

Doré, V. and Cheriet, M. Robust NL-means filter with optimal pixel-wise smoothing parameter for statistical image denoising. *IEEE Transactions on Signal Processing*, 2009. 57(5):1703–1716.

Elgersma, O.E., Buijs, P.C., Wüst, A.F., Van der Graaf, Y., Eikelboom, B.C. and Mali, W.P. Maximum internal carotid arterial stenosis: assessment with rotational angiography versus conventional intraarterial digital subtraction angiography. *Radiology*, 12 1999. 213(3):777–783.

Eliasziw, M., Streifler, J.Y., Fox, A.J., Hachinski, V.C., Ferguson, G.G. and Barnett, H.J. Significance of plaque ulceration in symptomatic patients with high-grade carotid stenosis. north american symptomatic carotid endarterectomy trial. *Stroke*, 2 1994. 25(2):304–308.

ESR. White paper on imaging biomarkers. *Insights Imaging*, 5 2010. (1):42–45.

Estes, J.M., Quist, W.C., Lo Gerfo, F.W. and Costello, P. Noninvasive characterization of plaque morphology using helical computed tomography. *Journal of Cardiovascular Surgery*, 10 1998. 39(5):527–534.

European Carotid Surgery Trial Collaborators. Randomised trial of endarterectomy for recently symptomatic carotid stenosis: final results of the mrc european carotid surgery trial (ecst). *Lancet*, 5 1998. 351(9113):1379–1387.

Flórez Valencia, L., Azencot, J. and Orkisz, M. Carotid arteries segmentation in CT images with use of a right generalized cylinder model. In *The Midas Journal*. 2009 .

Flórez Valencia, L., Azencot, J., Vincent, F., Orkisz, M. and Magnin, I. Segmentation and Quantification of Blood Vessels in 3D Images using a Right Generalized Cylinder State Model. In *Proc. IEEE Int. Conf. Image Process.* 2006 pages 2441–2444.

Freiman, M., Frank, J., Weizman, L., Nammer, E., Shilon, O., Joskowicz, L. and Sosna, J. Nearly automatic vessels segmentation using graph-based energy minimization. In *The Midas Journal*. 2009 .

Freund, Y. and Schapire, R.E. A decision-theoretic generalization of on-line learning and an application to boosting. *Journal of Computer and System Sciences*, 1997. 55(1):119 – 139.

Frostegård, J. Sle, atherosclerosis and cardiovascular disease. *Journal of Internal Medicine*, 2005. 257(6):1365–2796.

Ganten, M., Krautter, U., von Tengg-Kobligk, H., Böckler, D., Schumacher, H., Stiller, W., Delorme, S., Kauczor, H., Kauffmann, G. and Bock, M. Quantification of aortic distensibility in abdominal aortic aneurysm using ECG-gated multi-detector computed tomography. *European Radiology*, 5 2008. 18(5):966–973.

Gelder, A. Efficient computation of polygon area and polyhedron volume. In A. Paeth, editor, *Graphic Gems V*, pages 35–41. Academic Press, 1995.

Ginneken, B.V., III, S.G.A., Hoop, B.D., de Vorst, S.V.A.V., Duindam, T., Niemeijer, M., Murphy, K., Schilham, A., Retico, A., Fantacci, M.E., Camarlinghi, N., Bagagli, F., Gori, I., Hara, T., Fujita, H., Gargano, G., Bellotti, R., Tangaro, S., Bolaños, L., Carlo, F.D., Cerello, P., Cheran, S.C., Torres, E.L. and Prokop, M. Comparing and combining algorithms for computer-aided detection of pulmonary nodules in computed tomography scans: The ANODE09 study. *Medical Image Analysis*, 2010. 14(6):707 – 722.

Glagov, S., Weisenberg, E., Zarins, C.K., Stankunavicius, R. and Kolettis, G.J. Compensatory enlargement of human atherosclerotic coronary arteries. *New England Journal of Medicine*, 5 1987. 316(22):1371–1375.

Groen, H.C., Gijsen, F.J.H., Van der Lugt, A., Ferguson, M.S., Hatsukami, T.S., Van der Steen, A.F.W., Yuan, C. and Wentzel, J.J. Plaque rupture in the carotid artery is localized at the high shear stress region: a case report. *Stroke*, 8 2007. 38(8):2379–2381.

Gülsün, M. and Tek, H. Segmentation of carotid arteries by graph-cuts using centerline models. In *The Midas Journal*. 2009 .

Hackländer, T., Wegner, H., Hoppe, S., Danckworth, A., Kempkes, U., Fischer, M., Mertens, H. and Caldwell, J.H. Agreement of multislice ct angiography and mr angiography in assessing the degree of carotid artery stenosis in consideration of different methods of postprocessing. *Journal of Computer Assisted Tomography*, 2006. 30(3):433–442.

Halliday, A., Mansfield, A., Marro, J., Peto, C., Peto, R., Potter, J., Thomas, D. and Asymptomatic Carotid Surgery Trial (A.C.S.T) Collaborative Group. Prevention of disabling and fatal strokes by successful carotid endarterectomy in patients without recent neurological symptoms: randomised controlled

trial. *Lancet*, 5 2004. 363(9420):1491–1502.

Hameeteman, K., Freiman, M., Zuluaga, M., Joskowicz, L., Rozie, S., Van Gils, M., Van den Borne, L., Sosna, J., Berman, P., Cohen, N., Douek, P., Sanchez, I., Aissat, M., Van der Lugt, A., Krestin, G., Niessen, W. and Van Walsum, T. Carotid lumen segmentation and stenosis grading challenge. 2009a.

Hameeteman, K., Freiman, M., Zuluaga, M., Joskowicz, L. and Van Walsum, T. Grand challenge iii: Carotid lumen segmentation and stensosis grading. 2009b.

Hameeteman, K., Zuluaga, M., Freiman, M., Joskowicz, L., Cuisenaire, O., Valencia, L.F., Gulsun, M., Krissian, K., Mille, J., Wong, W., Orkisz, M., Tek, H., Hoyos, M.H., Benmansour, F., Chung, A., Rozie, S., Gils, M.V., den Borne, L.V., Sosna, J., Berman, P., Cohen, N., Douek, P., Sánchez, I., Aissat, M., Schaap, M., Metz, C., Krestin, G.P., der Lugt, A.V., Niessen, W. and Walsum, T.V. Evaluation framework for carotid bifurcation lumen segmentation and stenosis grading. *Medical Image Analysis*, 8 2011. 15(4):477–488.

Hankey, G.J., Warlow, C.P. and Molyneux, A.J. Complications of cerebral angiography for patients with mild carotid territory ischaemia being considered for carotid endarterectomy. *Journal of Neurology, Neurosurgery and Psychiatry*, 7 1990a. 53(7):542–548.

Hankey, G.J., Warlow, C.P. and Sellar, R.J. Cerebral angiographic risk in mild cerebrovascular disease. *Stroke*, 2 1990b. 21(2):209–222.

Heckel, F., Konrad, O., Hahn, H. and Peitgen, H. Interactive 3d medical image segmentation with energy-minimizing implicit functions. *Computers &; Graphics*, 2011. 35(2):275 – 287. Virtual Reality in Brazil Visual Computing in Biology and Medicine Semantic 3D media and contentCultural Heritage.

Heimann, T., Van Ginneken, B., Styner, M.A., Arzhaeva, Y., Aurich, V., Bauer, C., Beck, A., Becker, C., Beichel, R., Bekes, G., Bello, F., Binnig, G., Bischof, H., Bornik, A., Cashman, P.M.M., Chi, Y., Córdova, A., Dawant, B.M., Fidrich, M., Furst, J., Furukawa, D., Grenacher, L., Hornegger, J., Kainmüller, D., Kitney, R.I., Kobatake, H., Lamecker, H., Lange, T., Lee, J., Lennon, B., Li, R., Li, S., Meinzer, H.P., Németh, G., Raicu, D., Rau, A.M., Van Rikxoort, E.M., Rousson, M., Ruskó, L., Saddi, K.A., Schmidt, G., Seghers, D., Shimizu, A., Slagmolen, P., Sorantin, E., Soza, G., Susomboon, R., Waite, J.M., Wimmer, A. and Wolf, I. Comparison and evaluation of methods for liver segmentation from ct datasets. *IEEE Transactions on Medical Imaging*, 8 2009. 28(8):1251–1265.

Hoaglin, D.C. and Iglewicz, B. Fine-tuning some resistant rules for outlier labeling. *Journal of the American Statistical Association*, 1987. 82(400):1147–1149.

Hobson, 2nd, R., Weiss, D.G., Fields, W.S., Goldstone, J., Moore, W.S., Towne, J.B. and Wright, C.B. Efficacy of carotid endarterectomy for asymptomatic carotid stenosis. the veterans affairs cooperative study group. *New England Journal of Medicine*, 1 1993. 328(4):221–227.

Hofman, A., Duijn, C.V., Franco, O., Ikram, M., Janssen, H.A., Klaver, C., Kuipers, E., Nijsten, T., Stricker, B., Tiemeier, H., Uitterlinden, A., Vernooij, M. and Witteman, J. The rotterdam study: 2012 objectives and design update. *European Journal of Epidemiology*, 8 2011. 26(8):657–686.

Hollingworth, W., Nathens, A.B., Kanne, J.P., Crandall, M.L., Crummy, T.A., Hallam, D.K., Wang, M.C. and Jarvik, J.G. The diagnostic accuracy of computed tomography angiography for traumatic or atherosclerotic lesions of the carotid and vertebral arteries: a systematic review. *European Journal of Radiology*, 10 2003. 48(1):88–102.

Homburg, P.J., Rozie, S., Van Gils, M.J., Van den Bouwhuijsen, Q.J.A., Niessen, W.J., Dippel, D.W.J. and Van der Lugt, A. Association between carotid artery plaque ulceration and plaque composition evaluated with multidetector ct angiography. *Stroke*, 2 2011. 42(2):367–372.

Hoover, A., Jean-Baptiste, G., Jiang, X., Flynn, P.J., Bunke, H., Goldgof, D.B., Bowyer, K., Eggert, D.W., Fitzgibbon, A. and Fisher, R.B. An experimental comparison of range image segmentation algorithms. *IEEE Transactions Pattern Analysis and Machine Intelligence*, 1996. 18(7):673–689.

Howard, P., Bartlett, E.S., Symons, S.P., Fox, A.J. and Aviv, R.I. Measurement of carotid stenosis on computed tomographic angiography: reliability depends on postprocessing technique. *Canadian Association of Radiologists Journal*, 6 2010. 61(3):127–132.

Ibanez, L. and Schroeder, W. The case for open science. *Kitware white paper*, 2 2010.

Ibanez, L., Schroeder, W., Ng, L. and Cates, J. *The ITK Software Guide*. Kitware, Inc. ISBN 1-930934-15-7, http://www.itk.org/ItkSoftwareGuide.pdf, second edition, 2005.

Ikram, M.A., Van der Lugt, A., Niessen, W.J., Krestin, G.P., Koudstaal, P.J., Hofman, A., Breteler, M.M.B.

and Vernooij, M.W. The rotterdam scan study: design and update up to 2012. *European Journal of Epidemiology*, 10 2011. 26(10):811–824.

Jackson, C., Shirodaria, C., Lee, J., Francis, J., Choudhury, R., Channon, K., Noble, J., Neubauer, S. and Robson, M. Reproducibility and accuracy of automated measurement for dynamic arterial lumen area by cardiovascular magnetic resonance. *International Journal of Cardiovascular Imaging*, 2009. 25:797–808.

JAMA. Endarterectomy for asymptomatic carotid artery stenosis. executive committee for the asymptomatic carotid atherosclerosis study. *JAMA*, 5 1995. 273(18):1421–1428.

Johnson, C., Moorhead, R., Munzner, T., Pfister, H., Rheingans, P. and Yoo, T.S. *NIH/NSF Visualization Research Challenges Report*. IEEE Computer Society, 2006.

Josephson, S.A., Bryant, S.O., Mak, H.K., Johnston, S.C., Dillon, W.P. and Smith, W.S. Evaluation of carotid stenosis using ct angiography in the initial evaluation of stroke and tia. *Neurology*, 8 2004. 63(3):457–460.

Kang, X., Polissar, N., Han, C., Lin, E. and Yuan, C. Analysis of the measurement precision of arterial lumen and wall areas using high-resolution MRI. *Magnetic Resonance in Medicine*, 12 2000. 44(6):968–972.

Kégl, B., Krzyzak, A., Linder, T. and Zeger, K. Learning and design of principal curves. *IEEE Transactions Pattern Analysis and Machine Intelligence*, 3 2000. 22(3):281–297.

Kirbas, C. and Quek, F. A review of vessel extraction techniques and algorithms. *ACM Computing Surveys*, 2004. 36(2):81–121.

Klein, S., Pluim, J.P.W., Staring, M. and Viergever, M.A. Adaptive stochastic gradient descent optimisation for image registration. *International Journal of Computer Vision*, 2009. 81(3):227–239.

Klein, S., Staring, M., Murphy, K., Viergever, M.A. and Pluim, J.P.W. elastix: a toolbox for intensity-based medical image registration. *IEEE Transactions on Medical Imaging*, 1 2010. 29:196 – 205. Software available from the elastix website.

Koelemay, M., Nederkoorn, P., Reitsma, J. and Majoie, C. Systematic review of computed tomography angiography for assessment of carotid artery disease. *Stroke*, 2004. 35:2306–2312.

Krissian, K. and Arencibia-García, S. A minimal cost path and level set evolution approach for carotid bifurcation segmentation. In *The Midas Journal*. 2009 .

Krug, R., Boese, J.M. and Schad, L.R. Determination of aortic compliance from magnetic resonance images using an automatic active contour model. *Physics in Medicine and Biology*, 8 2003. 48(15):2391–2404.

Kwee, R.M. Systematic review on the association between calcification in carotid plaques and clinical ischemic symptoms. *Journal of Vascular Surgery*, 4 2010. 51(4):1015–1025.

Lalande, A., Khau Van Kien, P., Salvé, N., Ben Salem, D., Legrand, L., Walker, P.M., Wolf, J.E. and Brunotte, F. Automatic determination of aortic compliance with cine-magnetic resonance imaging: an application of fuzzy logic theory. *Investigative Radiology*, 12 2002. 37(12):685–691.

Laurent, S., Caviezel, B., Beck, L., Girerd, X., Billaud, E., Boutouyrie, P., Hoeks, A. and Safar, M. Carotid artery distensibility and distending pressure in hypertensive humans. *Hypertension*, 6 1994. 23(6 Pt 2):878–883.

Laurent, S., Cockcroft, J., Bortel, L.V., Boutouyrie, P., Giannattasio, C., Hayoz, D., Pannier, B., Vlachopoulos, C., Wilkinson, I., Struijker-Boudier, H. and for Non-invasive Investigation of Large Arteries, E.N. Expert consensus document on arterial stiffness: methodological issues and clinical applications. *European Heart Journal*, 11 2006. 27(21):2588–2605.

Lee, S.W., Antiga, L., Spence, J.D. and Steinman, D.A. Geometry of the carotid bifurcation predicts its exposure to disturbed flow. *Stroke*, 8 2008. 39(8):2341–2347.

Lesage, D., Angelini, E.D., Bloch, I. and Funka-Lea, G. A review of 3d vessel lumen segmentation techniques: Models, features and extraction schemes. *Medical Image Analysis*, 2009. 13(6):819 – 845.

Liang, Y.L., Shiel, L.M., Teede, H., Kotsopoulos, D., McNeil, J., Cameron, J.D. and McGrath, B.P. Effects of blood pressure, smoking, and their interaction on carotid artery structure and function. *Hypertension*, 1 2001. 37(1):6–11.

Liu, Y., Hopper, K.D., Mauger, D.T. and Addis, K.A. Ct angiographic measurement of the carotid artery: optimizing visualization by manipulating window and level settings and contrast material attenuation. *Radiology*, 11 2000. 217(2):494–500.

Lorenzo-Valdès, M., Sanchez-Ortiz, G., Bogren, H., Mohiaddin, R. and Rueckert, D. Determination of

aortic distensibility using non-rigid registration of cine MR images. In C. Barillot, D. Haynor and P. Hellier, editors, *Medical Image Computing and Computer-Assisted Intervention - MICCAI 2004*, volume 3216 of *Lecture Notes in Computer Science*, pages 754–762. Springer Berlin / Heidelberg, 2004.

Lovett, J.K., Gallagher, P.J., Hands, L.J., Walton, J. and Rothwell, P.M. Histological correlates of carotid plaque surface morphology on lumen contrast imaging. *Circulation*, 10 2004. 110(15):2190–2197.

Manniesing, R., Schaap, M., Rozie, S., Hameeteman, K., Vukadinovic, D., der Lugt, A.V. and Niessen, W. Robust cta lumen segmentation of the atherosclerotic carotid artery bifurcation in a large patient population. *Medical Image Analysis*, 12 2010. 14(6):759–69.

Manniesing, R., Viergever, M. and Niessen, W. Vessel axis tracking using topology constrained surface evolution. *IEEE Transactions on Medical Imaging*, 3 2007. 26(3):309 –316.

Mardia, K.V., Kent, J.T. and Bibby, J.M. *Multivariate Analysis*. Academic Press, 1979.

Martin, D., Fowlkes, C., Tal, D. and Malik, J. A database of human segmented natural images and its application to evaluating segmentation algorithms and measuring ecological statistics. In *Proc. Eighth IEEE International Conference on Computer Vision ICCV 2001*, volume 2. 7 2001 pages 416–423.

Metz, C., Klein, S., Schaap, M., Walsum, T.V. and Niessen, W. Nonrigid registration of dynamic medical imaging data using nD+t B-splines and a groupwise optimization approach. *Medical Image Analysis*, 2011. 15 (2):238–249.

Mille, J., Benmansour, F. and Cohen, L. Carotid lumen segmentation based on tubular anisotropy and contours without edges. In *The Midas Journal*. 2009 .

Morra, J.H., Tu, Z., Apostolova, L.G., Green, A.E., Toga, A.W. and Thompson, P.M. Automatic subcortical segmentation using a contextual model. *Medical Image Computing and Computer-Assisted Intervention*, 2008. 11(Pt 1):194–201.

Naghavi, M., Libby, P., Falk, E., Casscells, S.W., Litovsky, S., Rumberger, J., Badimon, J.J., Stefanadis, C., Moreno, P., Pasterkamp, G., Fayad, Z., Stone, P.H., Waxman, S., Raggi, P., Madjid, M., Zarrabi, A., Burke, A., Yuan, C., Fitzgerald, P.J., Siscovick, D.S., De Korte, C.L., Aikawa, M., Juhani Airaksinen, K.E., Assmann, G., Becker, C.R., Chesebro, J.H., Farb, A., Galis, Z.S., Jackson, C., Jang, I.K., Koenig, W., Lodder, R.A., March, K., Demirovic, J., Navab, M., Priori, S.G., Rekhter, M.D., Bahr, R., Grundy, S.M., Mehran, R., Colombo, A., Boerwinkle, E., Ballantyne, C., Insull, Jr, W., Schwartz, R.S., Vogel, R., Serruys, P.W., Hansson, G.K., Faxon, D.P., Kaul, S., Drexler, H., Greenland, P., Muller, J.E., Virmani, R., Ridker, P.M., Zipes, D.P., Shah, P.K. and Willerson, J.T. From vulnerable plaque to vulnerable patient: a call for new definitions and risk assessment strategies: Part i. *Circulation*, 10 2003. 108(14):1664–1672.

Nandalur, K.R., Hardie, A.D., Raghavan, P., Schipper, M.J., Baskurt, E. and Kramer, C.M. Composition of the stable carotid plaque: insights from a multidetector computed tomography study of plaque volume. *Stroke*, 3 2007. 38(3):935–940.

Natoli, A.K., Medley, T.L., Ahimastos, A.A., Drew, B.G., Thearle, D.J., Dilley, R.J. and Kingwell, B.A. Sex steroids modulate human aortic smooth muscle cell matrix protein deposition and matrix metalloproteinase expression. *Hypertension*, 11 2005. 46(5):1129–1134.

Newman, D.L., Gosling, R.G. and Bowden, N.L. Changes in aortic distensibility and area ratio with the development of atherosclerosis. *Atherosclerosis*, 1971. 14(2):231–240.

Niemeijer, M., Ginneken, B.V., Cree, M.J., Mizutani, A., Quellec, G., Sanchez, C.I., Zhang, B., Hornero, R., Lamard, M., Muramatsu, C., Wu, X., Cazuguel, G., You, J., Mayo, A., Li, Q., Hatanaka, Y., Cochener, B., Roux, C., Karray, F., Garcia, M., Fujita, H. and Abramoff, M.D. Retinopathy online challenge: automatic detection of microaneurysms in digital color fundus photographs. *IEEE Transactions on Medical Imaging*, 1 2010. 29(1):185–195.

North American Symptomatic Carotid Endarterectomy Trial Collaborators. Beneficial effect of carotid endarterectomy in symptomatic patients with high-grade carotid stenosis. north american symptomatic carotid endarterectomy trial collaborators. *New England Journal of Medicine*, 8 1991. 325(7):445–453.

Oliver, T.B., Lammie, G.A., Wright, A.R., Wardlaw, J., Patel, S.G., Peek, R., Ruckley, C.V. and Collie, D.A. Atherosclerotic plaque at the carotid bifurcation: Ct angiographic appearance with histopathologic correlation. *American Journal of Neuroradiology*, 5 1999. 20(5):897–901.

Orkisz, M., Flórez Valencia, L. and Hernández Hoyos, M. Models, algorithms and applications in vascular image segmentation. *Machine Graphics and Vision*, 2008. 17(1/2):5–33.

Pannier, B., Avolio, A., Hoeks, A., Mancia, G. and Takazawa, K. Methods and devices for measuring

arterial compliance in humans. *American Journal of Hypertension*, 8 2002. 15(8):743–753.

Persson, M., Ahlgren, Å., Jansson, T., Eriksson, A., Persson, H. and Lindström, K. A new non-invasive ultrasonic method for simultaneous measurements of longitudinal and radial arterial wall movements: first in vivo trial. *Clinical Physiology and Functional Imaging*, 2003. 23(5):247–251.

Prokop, M. Principal of computed tomography angiography. In G. Rubin and N. Rofsky, editors, *CT and MR Angiogrphy: Comprehensive Vascular Assessment*. Lippincott Williams & Wilkins, 2012.

Puchner, S., Popovic, M., Wolf, F., Reiter, M., Lammer, J. and Bucek, R.A. Multidetector cta in the quantification of internal carotid artery stenosis: value of different reformation techniques and axial source images compared with selective carotid arteriography. *Journal of Endovascular Therapy*, 6 2009. 16(3):336–342.

Randoux, B., Marro, B., Koskas, F., Duyme, M., Sahel, M., Zouaoui, A. and Marsault, C. Carotid artery stenosis: prospective comparison of ct, three-dimensional gadolinium-enhanced mr, and conventional angiography. *Radiology*, 7 2001. 220(1):179–185.

Roger, V., Go, A., Lloyd-Jones, D., Adams, R., Berry, J., Brown, T., Carnethon, M., Dai, S., Simone, G.D., Ford, E., Fox, C., Fullerton, H., Gillespie, C., Greenlund, K.J., Hailpern, S., Heit, J.A., Ho, P.M., Howard, V., Kissela, B., Kittner, S., Lackland, D., Lichtman, J., Lisabeth, L., Makuc, D., Marcus, G., Marelli, A., Matchar, D., McDermott, M., Meigs, J., Moy, C., Mozaffarian, D., Mussolino, M., Nichol, G., Paynter, N., Rosamond, W., Sorlie, P., Stafford, R., Turan, T., Turner, M., Wong, N., Wylie-Rosett, J., American Heart Association Statistics Committee and Stroke Statistics Subcommittee. Heart disease and stroke statistics–2011 update: a report from the american heart association. *Circulation*, 2 2011. 123(4):e18–e209.

Romero, J.M., Babiarz, L.S., Forero, N.P., Murphy, E.K., Schaefer, P.W., Gonzalez, R.G. and Lev, M.H. Arterial wall enhancement overlying carotid plaque on ct angiography correlates with symptoms in patients with high grade stenosis. *Stroke*, 5 2009. 40(5):1894–1896.

Rose, J.L., Lalande, A., Bouchot, O., Bourennane, E.B., Walker, P.M., Ugolini, P., Revol-Muller, C., Cartier, R. and Brunotte, F. Influence of age and sex on aortic distensibility assessed by mri in healthy subjects. *Magnetic Resonance Imaging*, 2 2010. 28(2):255–263.

Rothwell, P.M., Eliasziw, M., Gutnikov, S.A., Fox, A.J., Taylor, D.W., Mayberg, M.R., Warlow, C.P., Barnett, H.J.M. and Collaboration, C.E.T. Analysis of pooled data from the randomised controlled trials of endarterectomy for symptomatic carotid stenosis. *Lancet*, 1 2003. 361(9352):107–116.

Rothwell, P.M., Gibson, R. and Warlow, C.P. Interrelation between plaque surface morphology and degree of stenosis on carotid angiograms and the risk of ischemic stroke in patients with symptomatic carotid stenosis. on behalf of the european carotid surgery trialists' collaborative group. *Stroke*, 3 2000. 31(3):615–621.

Rozie, S., De Weert, T.T., De Monyé, C., Homburg, P.J., Tanghe, H.L.J., Dippel, D.W.J. and Van der Lugt, A. Atherosclerotic plaque volume and composition in symptomatic carotid arteries assessed with multidetector ct angiography; relationship with severity of stenosis and cardiovascular risk factors. *European Radiology*, 9 2009. 19(9):2294–2301.

Rueckert, D., Sonoda, L.I., Hayes, C., Hill, D.L.G., Leach, M.O. and Hawkes, D.J. Nonrigid registration using free-form deformations: Application to breast MR images. *IEEE Transactions on Medical Imaging*, 1999. 18:712–721.

Saba, L., Anzidei, M., Sanfilippo, R., Montisci, R., Lucatelli, P., Catalano, C., Passariello, R. and Mallarini, G. Imaging of the carotid artery. *Atherosclerosis*, 2 2012. 220(2):294–309.

Saba, L., Caddeo, G., Sanfilippo, R., Montisci, R. and Mallarini, G. Efficacy and sensitivity of axial scans and different reconstruction methods in the study of the ulcerated carotid plaque using multidetector-row ct angiography: comparison with surgical results. *American Journal of Neuroradiology*, 4 2007. 28(4):716–723.

Saba, L. and Mallarini, G. Carotid plaque enhancement and symptom correlations: an evaluation by using multidetector row ct angiography. *American Journal of Neuroradiology*, 2011. 32(10):1919–1925.

Salvado, O., Hillenbrand, C., Zhang, S. and Wilson, D. Method to correct intensity inhomogeneity in mr images for atherosclerosis characterization. *IEEE Transactions on Medical Imaging*, 2006. 25(5):539–552.

Schaap, M., Metz, C., Walsum, T.V., der Giessen, A.V., Weustink, A., Mollet, N., Bauer, C., Bogunovic, H.,

Castro, C., Deng, X., Dikici, E., O'Donnell, T., Frenay, M., Friman, O., Hernández Hoyos, M., Kitslaar, P., Krissian, K., Kühnel, C., Luengo-Oroz, M.A., Orkisz, M., Smedby, O., Styner, M., Szymczak, A., Tek, H., Wang, C., Warfield, S.K., Zambal, S., Zhang, Y., Krestin, G.P. and Niessen, W. Standardized evaluation methodology and reference database for evaluating coronary artery centerline extraction algorithms. *Medical Image Analysis*, 2009. 13/5:701–714.

Scharstein, D. and Szeliski, R. A taxonomy and evaluation of dense two-frame stereo correspondence algorithms. *International Journal on Computer Vision*, 2002. 47(1-3):7–42.

Scherl, H., Hornegger, J., Prümmer, M. and Lell, M. Semi-automatic level-set based segmentation and stenosis quantification of the internal carotid artery in 3d cta data sets. *Medical Image Analysis*, 2 2007. 11(1):21–34.

Schroeder, W., Martin, K. and Lorensen, B. *Visualization Toolkit: An Object-Oriented Approach to 3D Graphics, 4th Edition*. Kitware, 12 2006.

Schwartz, E., Holfeld, J., Czerny, M. and Langs, G. Visualizing changes in vessel wall dynamics due to stent-grafting in the aortic arch. In *Proc IEEE Int Biomedical Imaging (ISBI) Symp*. 2012 pages 788–791.

Shapiro, S.S. and Wilk, M.B. An analysis of variance test for normality (complete samples). *Biometrika*, 1965. 52(3-4):591–611.

Shrout, P.E. and Fleiss, J.L. Intraclass correlations: uses in assessing rater reliability. *Psychological Bulletin*, 3 1979. 86(2):420–428.

Sled, J., Zijdenbos, A. and Evans, A. A nonparametric method for automatic correction of intensity nonuniformity in MRI data. *IEEE Transactions on Medical Imaging*, 2 1998. 17(1):87–97.

Streifler, J.Y., Eliasziw, M., Fox, A.J., Benavente, O.R., Hachinski, V.C., Ferguson, G.G. and Barnett, H.J. Angiographic detection of carotid plaque ulceration. comparison with surgical observations in a multicenter study. north american symptomatic carotid endarterectomy trial. *Stroke*, 6 1994. 25(6):1130–1132.

Takaya, N., Yuan, C., Chu, B., Saam, T., Underhill, H., Cai, J., Tran, N., Polissar, N., Isaac, C., Ferguson, M., Garden, G., Cramer, S., Maravilla, K., Hashimoto, B. and Hatsukami, T. Association between carotid plaque characteristics and subsequent ischemic cerebrovascular events: a prospective assessment with MRI–initial results. *Stroke*, 3 2006. 37(3):818–823.

Tax, D.M., Breukelen, M.V., Duin, R.P. and Kittler, J. Combining multiple classifiers by averaging or by multiplying? *Pattern Recognition*, 2000. 33(9):1475 – 1485.

Thévenaz, P. and Unser, M. Optimization of mutual information for multiresolution image registration. *IEEE Transactions on Image Processing*, 2000. 9(12):2083–2099.

Tu, Z., Zheng, S., Yuille, A.L., Reiss, A.L., Dutton, R.A., Lee, A.D., Galaburda, A.M., Dinov, I., Thompson, P.M. and Toga, A.W. Automated extraction of the cortical sulci based on a supervised learning approach. *IEEE Transactions on Medical Imaging*, 4 2007. 26(4):541–552.

Turk, G. and O'Brien, J. Shape transformation using variational implicit functions. In *SIGGRAPH '99: Proceedings of the 26th annual conference on Computer graphics and interactive techniques*. ACM Press/Addison-Wesley Publishing Co., New York, NY, USA, 1999 pages 335–342.

Turkowski, K. Graphics gems. In A.S. Glassner, editor, *Graphics gems*, chapter Filters for common resampling tasks, pages 147–165. Academic Press Professional, Inc., San Diego, CA, USA, 1990.

Tustison, N., Avants, B., Cook, P., Zheng, Y., Egan, A., Yushkevich, P. and Gee, J. N4itk: improved n3 bias correction. *IEEE Transactions on Medical Imaging*, 6 2010. 29(6):1310–1320.

Uotani, K., Watanabe, Y., Higashi, M., Nakazawa, T., Kono, A.K., Hori, Y., Fukuda, T., Kanzaki, S., Yamada, N., Itoh, T., Sugimura, K. and Naito, H. Dual-energy ct head bone and hard plaque removal for quantification of calcified carotid stenosis: utility and comparison with digital subtraction angiography. *European Radiology*, 8 2009. 19(8):2060–2065.

Van den Bouwhuijsen, Q., Vernooij, M., Hofman, A., Krestin, G., der Lugt, A.V. and Witteman, J. Determinants of magnetic resonance imaging detected carotid plaque components: the rotterdam study. *European Heart Journal*, 2011.

Van Popele, N.M., Grobbee, D.E., Bots, M.L., Asmar, R., Topouchian, J., Reneman, R.S., Hoeks, A.P., der Kuip, D.A.V., Hofman, A. and Witteman, J.C. Association between arterial stiffness and atherosclerosis: the Rotterdam Study. *Stroke*, 2 2001. 32(2):454–460.

Van Straten, M., Venema, H.W., Streekstra, G.J., Majoie, C.B.L.M., Den Heeten, G.J. and Grimbergen,

C.A. Removal of bone in ct angiography of the cervical arteries by piecewise matched mask bone elimination. *Medical Physics*, 10 2004. 31(10):2924–2933.

Van 't Klooster, R., De Koning, P., Dehnavi, R., Tamsma, J., De Roos, A., Reiber, J. and Van der Geest, R. Automatic lumen and outer wall segmentation of the carotid artery using deformable three-dimensional models in MR angiography and vessel wall images. *Journal of Magnetic Resonance Imaging*, 2012. 35(1):156–165.

Varghese, A., Crowe, L., Mohiaddin, R., Gatehouse, P., Yang, G., Firmin, D. and Pennell, D. Inter-study reproducibility of 3d volume selective fast spin echo sequence for quantifying carotid artery wall volume in asymptomatic subjects. *Atherosclerosis*, 12 2005. 183(2):361–366.

Venema, H.W., Hulsmans, F.J. and Den Heeten, G.J. Ct angiography of the circle of willis and intracranial internal carotid arteries: maximum intensity projection with matched mask bone elimination-feasibility study. *Radiology*, 3 2001. 218(3):893–898.

Vukadinovic, D., Rozie, S., Van Gils, M., Van Walsum, T., Manniesing, R., Van der Lugt, A. and Niessen, W.J. Automated versus manual segmentation of atherosclerotic carotid plaque volume and components in cta: associations with cardiovascular risk factors. *International Journal of Cardiovascular Imaging*, 4 2012. 28(4):877–887.

Vukadinovic, D., Van Walsum, T., Manniesing, R., Rozie, S., Hameeteman, R., De Weert, T.T., Van der Lugt, A. and Niessen, W.J. Segmentation of the outer vessel wall of the common carotid artery in cta. *IEEE Transactions on Medical Imaging*, 1 2010. 29(1):65–76.

Waddell, T.K., Dart, A.M., Gatzka, C.D., Cameron, J.D. and Kingwell, B.A. Women exhibit a greater age-related increase in proximal aortic stiffness than men. *Journal of Hypertension*, 12 2001. 19(12):2205–2212.

Walker, L.J., Ismail, A., McMeekin, W., Lambert, D., Mendelow, A.D. and Birchall, D. Computed tomography angiography for the evaluation of carotid atherosclerotic plaque: correlation with histopathology of endarterectomy specimens. *Stroke*, 4 2002. 33(4):977–981.

Wang, H., Das, S., Suh, J., Altinay, M., Pluta, J., Craige, C., Avants, B., Yushkevich, P. and Initiative, A.D.N. A learning-based wrapper method to correct systematic errors in automatic image segmentation: consistently improved performance in hippocampus, cortex and brain segmentation. *NeuroImage*, 4 2011. 55(3):968–985.

Wardlaw, J.M., Chappell, F.M., Best, J.J.K., Wartolowska, K., Berry, E. and N. H. S Research and Development Health Technology Assessment Carotid Stenosis Imaging Group. Non-invasive imaging compared with intra-arterial angiography in the diagnosis of symptomatic carotid stenosis: a meta-analysis. *The Lancet*, 5 2006. 367(9521):1503–1512.

Warfield, S.K., Zou, K.H. and Wells, W.M. Simultaneous truth and performance level estimation (staple): an algorithm for the validation of image segmentation. *IEEE Transactions on Medical Imaging*, 7 2004. 23(7):903–921.

Warlow, C., Sudlow, C., Dennis, M., Wardlaw, J. and Sandercock, P. Stroke. *The Lancet*, 10 2003. 362(9391):1211–1224.

Waterton, J.C. and Pylkkanen, L. Qualification of imaging biomarkers for oncology drug development. *European Journal of Cancer*, 4 2012. 48(4):409–415.

Waugh, J.R. and Sacharias, N. Arteriographic complications in the dsa era. *Radiology*, 1 1992. 182(1):243–246.

Weber, T., Ganten, M., Böckler, D., Geisbüsch, P., Kopp-Schneider, A., Kauczor, H. and von Tengg-Kobligk, H. Assessment of thoracic aortic conformational changes by four-dimensional computed tomography angiography in patients with chronic aortic dissection type B. *European Radiology*, 1 2009. 19(1):245–253.

West, J., Fitzpatrick, J.M., Wang, M.Y., Dawant, B.M., Maurer, C.R., Kessler, R.M., Maciunas, R.J., Barillot, C., Lemoine, D., Collignon, A., Maes, F., Suetens, P., Vandermeulen, D., van den Elsen, P.A., Napel, S., Sumanaweera, T.S., Harkness, B., Hemler, P.F., Hill, D.L., Hawkes, D.J., Studholme, C., Maintz, J.B., Viergever, M.A., Malandain, G. and Woods, R.P. Comparison and evaluation of retrospective intermodality brain image registration techniques. *Journal of Computer Assisted Tomography*, 1997. 21(4):554–566.

Willinsky, R.A., Taylor, S.M., TerBrugge, K., Farb, R.I., Tomlinson, G. and Montanera, W. Neurologic

complications of cerebral angiography: prospective analysis of 2,899 procedures and review of the literature. *Radiology*, 5 2003. 227(2):522–528.

Wintermark, M., Arora, S., Tong, E., Vittinghoff, E., Lau, B.C., Chien, J.D., Dillon, W.P. and Saloner, D. Carotid plaque computed tomography imaging in stroke and nonstroke patients. *Annals of Neurology*, 8 2008a. 64(2):149–157.

Wintermark, M., Glastonbury, C., Tong, E., Lau, B.C., Schaeffer, S., Chien, J.D., Haar, P.J. and Saloner, D. Semi-automated computer assessment of the degree of carotid artery stenosis compares favorably to visual evaluation. *Journal of the Neurological Sciences*, 2008b. 269(1-2):74 – 79.

Wintermark, M., Jawadi, S., Rapp, J., Tihan, T., Tong, E., Glidden, D., Abedin, S., Schaeffer, S., Acevedo-Bolton, G., Boudignon, B., Orwoll, B., Pan, X. and Saloner, D. High-resolution ct imaging of carotid artery atherosclerotic plaques. *American Journal of Neuroradiology*, 5 2008c. 29(5):875–882.

Wong, W., So, R. and Chung, A. Principal Curves: a technique for preliminary carotid lumen segmentation and stenosis grading. In *The Midas Journal*. 2009 .

Xiong, G. and Taylor, C.A. Physics-based modeling of aortic wall motion from ECG-gated 4d computed tomography. *Medical Image Computing and Computer-Assisted Intervention*, 2010. 13(Pt 1):426–434.

Yuan, C., Beach, K., Smith, L. and Hatsukami, T. Measurement of atherosclerotic carotid plaque size in vivo using high resolution magnetic resonance imaging. *Circulation*, 12 1998. 98(24):2666–2671.

Yuan, C., Lin, E., Millard, J. and Hwang, J. Closed contour edge detection of blood vessel lumen and outer wall boundaries in black-blood MR images. *Magnetic Resonance Imaging*, 2 1999. 17(2):257–266.

Yuan, C., Mitsumori, L.M., Beach, K.W. and Maravilla, K.R. Carotid atherosclerotic plaque: noninvasive mr characterization and identification of vulnerable lesions. *Radiology*, 11 2001. 221(2):285–299.

Yuan, C., Murakami, J.W., Hayes, C.E., Tsuruda, J.S., Hatsukami, T.S., Wildy, K.S., Ferguson, M.S. and Strandness, Jr, D. Phased-array magnetic resonance imaging of the carotid artery bifurcation: preliminary results in healthy volunteers and a patient with atherosclerotic disease. *Journal of Magnetic Resonance Imaging*, 1995. 5(5):561–565.

Zahnd, G., Boussel, L., Marion, A., Durand, M., Moulin, P., Sérusclat, A. and Vray, D. Measurement of two-dimensional movement parameters of the carotid artery wall for early detection of arteriosclerosis: a preliminary clinical study. *Ultrasound in Medecine and Biology*, 2011. 37(9):1421–1429.

Zahnd, G., Orkisz, M., Sérusclat, A., Moulin, P. and Vray, D. Evaluation of a Kalman-based block matching method to assess the bi-dimensional motion of the carotid artery wall in B-mode ultrasound sequences. *Medical Image Analysis*, 2013. 17(5):573–585.

Zahnd, G., Vray, D., Sérusclat, A., Alibay, D., Bartold, M., Brown, A., Durand, M., Jamieson, L., Kapellas, K., Maple-Brown, L., O'Dea, K., Moulin, P., Celermajer, D. and Skilton, M. Longitudinal displacement of the carotid wall and cardiovascular risk factors: associations with aging, adiposity, blood pressure and periodontal disease independent of cross-sectional distensibility and intima-media thickness. *Ultrasound in Medecine & Biology*, 2012. 38(10):1705–1715.

Zhang, J., Fletcher, J., Vrtiska, T., Manduca, A., Thompson, J., Raghavan, M., Wentz, R. and McCollough, C. Large-vessel distensibility measurement with electrocardiographically gated multidetector CT: phantom study and initial experience. *Radiology*, 10 2007. 245(1):258–266.

Zhang, S., Cai, J., Luo, Y., Han, C., Polissar, N., Hatsukami, T. and Yuan, C. Measurement of carotid wall volume and maximum area with contrast-enhanced 3d mr imaging: initial observations. *Radiology*, 7 2003. 228(1):200–205.

Zhang, Z., Berg, M., Ikonen, A., Könönen, M., Kälviäinen, R., Manninen, H. and Vanninen, R. Carotid stenosis degree in ct angiography: assessment based on luminal area versus luminal diameter measurements. *European Radiology*, 11 2005. 15(11):2359–2365.

Zhao, F., Zhang, H., Wahle, A., Thomas, M.T., Stolpen, A.H., Scholz, T.D. and Sonka, M. Congenital aortic disease: 4d magnetic resonance segmentation and quantitative analysis. *Medical Image Analysis*, 6 2009. 13(3):483–493.

Zuluaga, M., Orkisz, M., Delgado Leyton, E., Doré, V., Morales Pinzón, A. and Hernández Hoyos, M. Adaptations of MARACAS algorithm to the segmentation of the carotid bifurcation and stenosis quantification in CTA images. In *The Midas Journal*. 2009 .

Samenvatting

Medische beeldvormende technieken, zoals magnetic resonance imaging (MRI) en computed tomography (CT), spelen een belangrijke rol in de diagnose en behandeling van cardiovasculaire aandoeningen. Het extraheren van kwantitatieve gegevens uit deze beelden, die iets zeggen over de aanwezigheid en ernst van de ziekte, is belangrijk voor het optimaal benutten van de informatie die in deze beelddata beschikbaar is. De analyse van MRI- en CT-beelden kan objectief en efficiënt worden uitgevoerd door deze te automatiseren. Relevante kwantitatieve parameters die uit beelddata worden verkregen, worden ook wel "Quantitative Imaging Biomarkers" (QIBs) genoemd. In dit proefschrift beschrijven en evalueren we een aantal methoden voor het extraheren van QIBs die gerelateerd zijn aan atherosclerose van de halsslagader (arteria carotis of kortweg carotis).

Allereerst behandelen we de vernauwing van het lumen, de stenosegraad. In **Hoofdstuk 2** beschrijven we de huidige state-of-the-art in CT angiography (CTA) technieken. Met behulp van CTA kunnen bloedvaten worden afgebeeld. Uit deze beelden kan daarna de stenosegraad en de door atherosclerose veroorzaakte vaatwandverdikking (plaque) bepaald worden met behulp van (semi-) automatische analysesoftware. Dit maakt het mogelijk de verschillende stadia van de atherosclerose in het bloedvat te volgen zonder dat daarvoor een chirurgische ingreep nodig is. In **Hoofdstuk 3** is een evaluatiesysteem beschreven voor de gestandaardiseerde, objectieve en kwantitatieve vergelijking van methodes voor lumensegmentatie en stenosegraadmetingen van de carotis. De basis van zo'n evaluatiesysteem is een set representatieve beelddata, waarin de te bepalen QIB nauwkeurig bekend is (referentiestandaard). In dit hoofdstuk beschrijven we de database met beelddata -bestaande uit 56 CTA-datasets- en de manier waarop de referentiestandaard is verkregen. De CTA-data zijn verzameld bij verschillende medische centra en verkregen met behulp van scanners van verschillende fabrikanten. Dit evaluatiesysteem is in 2009 geïntroduceerd tijdens de MICCAI-workshop *3D Segmentation in the Clinic: A Grand Challenge III*. We vergelijken de resultaten van acht teams die aan deze workshop deelnamen. De resultaten laten zien dat met automatische lumensegmentatie een vergelijkbare precisie kan worden bereikt als met handmatige annotatie. Hoewel de (semi-)automatische kwantificatie van de stenosegraad een logische vervolgstap op lumensegmentatie is, blijkt deze stap nog niet vaak gemaakt te worden. De resultaten van de drie teams die een semi-automatische stenosegraadmeting hebben geëvalueerd, laten zien dat de handmatige metingen veel nauwkeuriger zijn. Het

evaluatiesysteem staat open voor nieuwe inzendingen en is beschikbaar via de website http://cls2009.bigr.nl. Op dit moment hebben 14 teams resultaten ingestuurd voor de lumensegmentatie en drie teams voor de stenosegraadmetingen.

In **Hoofdstuk 4** is een methode gepresenteerd en geëvalueerd voor de kwantificatie van het vaatwandvolume van de carotis in MRI data. De gepresenteerde methode voor lumen- en buitenwandsegmentatie combineert twee segmentatietechnieken: een techniek gebaseerd op "deformable models" en een correctiestap door middel van patroonherkenningstechnieken. Na het initialiseren van het algoritme met twee punten, wordt het vaatwandvolume in een gebied rond de bifurcatie automatisch bepaald. De methode is getraind op acht datasets (16 carotiden) uit een populatiestudie onder ouderen. Deze trainingsset is door een waarnemer manueel geannoteerd. De evaluatie is gebaseerd op een aparte set van 19 datasets (38 carotiden) uit dezelfde populatiestudie. Voor deze evaluatieset zijn door twee waarnemers handmatige annotaties gemaakt. Voor de evaluatieset zijn het vaatwandvolume en de genormaliseerde vaatwandindex (verhouding tussen het lumen- en vaatwandvolume) van de handmatige annotaties vergeleken met de automatische metingen. Onze experimenten tonen aan dat de automatische metingen vergelijkbaar zijn met de handmatige metingen. Alle beelddata en annotaties uit deze studie zijn samen met de meetresultaten publiekelijk beschikbaar via de website .

In **Hoofdstuk 5** gaat de aandacht naar de distensibiliteit van de carotis, een maat voor de elasticiteit van de vaatwand. In dit hoofdstuk hebben we de mogelijkheden onderzocht om de distensibiliteit van de carotis te meten op vierdimensionale (4D) CTA-beelddata. We hebben dit onderzocht zowel voor handmatige metingen (38 beelden) als voor een nieuwe automatische methode (76 beelden). Op een deelverzameling (10 beelden) van de handmatige metingen heeft een tweede waarnemer ook metingen verricht. De variatie tussen deze twee handmatige metingen (interwaarnemervariatie) is beoordeeld met behulp van een Bland-Altmananalyse. Uit deze analyse bleek dat de precisie van de handmatige metingen te laag is om de distensibiliteit te kunnen meten. Twee automatische methodes zijn met elkaar vergeleken: één gebaseerd op 3D-registratie en één gebaseerd op 4D-registratie. De 4D-methode resulteerde in een veel gelijkmatiger deformatiepatroon in de tijd. De automatische methode is geëvalueerd door gebruik te maken van synthetische deformaties en door te onderzoeken of de methode bekende relaties tussen de distensibiliteit en cardiovasculaire risicofactoren kon reproduceren. Deze relatie tussen distensibiliteit en cardiovasculaire risicofactoren is onderzocht met een Mann-Whitneytoets. De automatische distensibiliteitsmetingen bleken geassocieerd te zijn met hypertensie, terwijl de handmatige metingen deze associatie niet hadden. Dit verband tussen distensibiliteit en hypertensie is ook in andere studies gevonden. Onze conclusie is dat distensibiliteitsmetingen voor de carotis met behulp van een automatische methode dienen te worden uitgevoerd en dat de methode die in dit hoofdstuk wordt beschreven daarvoor kan worden gebruikt. Alle CTA-datasets en de bijbehorende klinische data die in deze studie zijn gebruikt, kunnen worden gedownload van de

website http://ctadist.bigr.nl.

In **Hoofdsuk 6** wordt de analyse van de relatie tussen cardiovasculaire risicofactoren en de elasticiteit van de carotis vervolgd. Behalve naar distensibiliteit wordt in dit hoofdstuk gekeken naar de longitudinale deformatie. Voor de meting van deze deformatie langs de vaatwand wordt ook een automatische methode gepresenteerd. De relatie met de volgende cardiovasculaire risicofactoren hebben we geanalyseerd: diabetes, hypercholesterolemie, hypertensie en roken. Doorgaans wordt zowel de distensibiliteit als de longitudinale deformatie gemeten met behulp van echoscopie. In deze studie hebben we de mogelijkheden onderzocht om beide grootheden te meten met CTA-beelddata. CTA maakt het mogelijk volledig driedimensionale metingen te verrichten. We hebben de distensibiliteit en longitudinale deformatie geanalyseerd voor 81 patiënten met ischemische cerebrovasculaire symptomen en de relatie tussen deze metingen en de vier cardiovasculaire risicofactoren onderzocht. Voor elke van de genoemde risicofactoren zijn twee statische analyses gedaan met een General Linear Model: i) met een basis model waarin alleen leeftijd en geslacht als covarianten zijn meegenomen, en ii) met een uitgebreid model waarin leeftijd, geslacht en de andere risicofactoren als covarianten zijn meegenomen. We hebben een matige correlatie tussen de distensibiliteit en longitudinale deformatie gevonden van ongeveer 0.5. De gemiddelde distensibiliteit was $24 \pm 1\ (MPa)^{-1}$ (gemiddelde $\pm$ standaard deviatie) voor de carotis (communis) en $14.2 \pm 0.9\ (MPa)^{-1}$ voor de interne carotis. De longitudinale deformaties waren respectievelijk $40 \pm 35\ mm/MPa$ en $49 \pm 28\ mm/MPa$. De groottes van deze waarden komen overeen met de bevindingen uit eerdere op echoscopie gebaseerde studies. We vonden een statisch significante daling van de distensibiliteit in de carotis communis voor patiënten met hypertensie. Deze relatie bleef significant na de correctie voor leeftijd, geslacht en de drie andere cardiovasculaire risicofactoren. Voor de longitudinale deformatie hebben we geen significante associaties gevonden.

Samenvattend, hebben we in dit proefschrift de geautomatiseerde analyse van de volgende vier aan atherosclerose van de carotis gerelateerde QIBs onderzocht: de stenosegraad, het vaatwandvolume, de distensibiliteit en de longitudinale deformatie. Voor de laatste drie hebben we nieuwe geautomatiseerde methodes gepresenteerd en de nauwkeurigheid ervan geëvalueerd. Alle beelddata die in de gepresenteerde studies zijn gebruikt, hebben we online beschikbaar gemaakt. Dit maakt verdere evaluatie en vergelijking met andere methodes mogelijk. Voor de lumensegmentatie en stenosegraadmetingen hebben we daarnaast een online evaluatiesysteem opgezet. De gepresenteerde evaluaties laten zien dat MRI-vaatwandmetingen en 4D-CTA-distensibiliteitsmetingen met behulp van de gepresenteerde geautomatiseerde methodes kunnen worden verricht.

Dankwoord

Aan de uitvoering van een muziekstuk gaat vaak een intensieve individuele voorbereiding vooraf. Iedereen oefent zijn eigen partij tot ze perfect klinkt, waarna een dirigent die individuele bijdragen tot één geheel maakt en laat uitmonden in een gezamenlijk kunstwerk. Het behalen van een doctorsgraad is eigenlijk het omgekeerde. Tijdens het onderzoek zijn er heel veel mensen betrokken bij het discussiëren over de onderzoeksvraag, het verzamelen van de benodigde data, het implementeren van een algoritme en het schrijven van het artikel. Naarmate het einde van het promotieonderzoek nadert, wordt het aantal deelnemers aan dat project gestaag minder, tot je uiteindelijk in je eentje al het gedane werk moet verdedigen tegenover de promotiecommissie. Maar hoewel er op het titelblad van mijn proefschrift slechts één naam prijkt, heb ik dit project natuurlijk niet alleen uitgevoerd. Graag wil ik iedereen bedanken die op de een of andere manier aan de totstandkoming van dit proefschrift heeft bijgedragen. Een aantal mensen wil ik hieronder in het bijzonder bedanken.

Wiro, bedankt voor de mogelijkheden die je me hebt geboden. De positieve perspectieven en vertrouwen in de goede resultaten die ongetwijfeld op de genomen keuzes zouden volgen, werkten sterk stimulerend. De ontspannen, maar gedreven manier waarop jij de groep leidt zijn inspirerend en geven vertrouwen. Toen jij een paar jaar geleden een ballonnetje opliet over het starten van een bedrijf dat onderzoekssoftware geschikt zou moeten maken voor klinisch gebruik, was ik meteen enthousiast. Het heeft vervolgens nog lang geduurd, maar het bestaan van Quantib is nu een feit en ik verheug me op de verdere samenwerking.

Stefan, je bent mijn copromotor, maar ik heb eigenlijk geen idee wanner je die status gekregen hebt. Op een gegeven moment was je het gewoon. Ik heb veel bewondering voor je oog voor detail en je zeer nauwgezette lezing van mijn papers die na jouw commentaar de status van concept zelden te boven kwamen. Dat ze toch gepubliceerd zijn, komt doordat je ook wist te motiveren. Ik moest me volgens jou vaak maar “even kwaad maken” en dan was er weer een compleet nieuwe versie. Commentaar van jou was ook zelden te weerleggen. Je had heel vaak gelijk. Bedankt voor je betrokkenheid en ik zie uit naar een verdere samenwerking rondom `elastix`.

Theo, jij hebt me de eerste beginselen van OO geleerd en mijn kennis van C++ en STL verdiept. Je was altijd bereid mee te denken over programmeerproblemen, onderzoeksopzetten en koffieapparaten en alle (niet)lineaire combinaties die daar-

van te maken zijn. Ik kijk met veel plezier terug op de organisatie van de MICCAI Carotide Challenge die ik samen met jou gedaan heb. Het was veel werk, maar gelukkig konden we ook veel gebruiken van de Coronary Challenge die je samen met Coert en Michiel had georganiseerd.

Als onderzoek je niet motiveert moet je niet gaan promoveren, maar bij BIGR is de verleiding groot er alleen al vanwege de collega's te gaan werken. Coert, Fedde, Michiel en Renske, jullie zijn het langst mijn naaste collega's geweest. Lang waren jullie ook de sociale basis van de groep en werden bijna alle "buiten-BIGR-events" door jullie georganiseerd. Ik denk met heel veel plezier terug aan alle borrels, etentjes, de rodeklaversmiley, koffiesessies, jongleeroefeningen en filmavonden.

Coert en Renske, jullie zijn de meest constante factor in mijn carrière tot nu toe. We hebben veel samen beleefd en ik vind het fantastisch die collegiale band binnen Quantib te kunnen voortzetten. Het is een eer jullie als paranimfen te hebben.

Toen ik voor het eerst bij BIGR kwam had de groep meer stafleden dan promovendi en studenten bij elkaar en was er nog geen stuctureel ruimtetekort. Ik kreeg een plek in een kamer aan de zuidkant van het gebouw, met uitzicht op de Maas. Als een van de weinigen binnen BIGR heb ik mijn eerste kamer niet (hoeven te) verlaten. Al mijn kamergenoten moesten dat wel. Het aantal kamergenoten dat ik had varieerde tussen de nul en vier. Ik begon bij Coert en Michiel op de kamer en nadat die de veroverde ruimte op de 23e verdieping gingen verdedigen nam ik die taak voor op me voor 'mijn' kamer. Deze periode van rust en eenzaamheid diende ook als tussenperiode naar een lange tijd waarin ik slechts vrouwelijke kamergenoten had. Achtereenvolgens kwamen en gingen Lejla, Danijela, Azadeh en Karin. De laatste maanden kwam er weer een nieuw soort dynamiek in de kamer met het zuidelijk temperament van Gerardo, Francesco en Jean-Marie. Iedereen bedankt voor zijn of haar bijdrage aan de prettige sfeer die er altijd in Ee2108 aanwezig was.

Veel onderzoek van BIGR gebeurt in samenwerking met de afdeling Radiologie en Epidemiologie. In het bijzonder heb ik in dit verband de samenwerking met Aad van der Lugt gewaardeerd. Aad, jij hebt het vermogen de kliniek, het medisch onderzoek en het meer technische onderzoek binnen BIGR te combineren en daarin veel werk voor elkaar te krijgen. Sietske, bedankt voor de samenwerking binnen de distensibility studie en de challenge. Marjon, bedankt voor het challengewerk en de samenwerking voor het boekhoofdstuk. Marianne bedankt voor het vele werk dat jij voor de vaatwandstudie hebt gedaan.

Een van de vaste sociale activiteiten van BIGR was het jaarlijkse midweekweekend. De organisatie daarvan samen met Hortense en Esben was een leuke ervaring. Het gewenste avonturenpark viel helaas niet binnen het budget, maar een koe melken en boter maken waren een grappig alternatief voor studeerkamerstedelingen. Conferenties zijn behalve inspirerend op wetenschappelijk gebied ook altijd een mooie gelegenheid om een ander land te verkennen. Nora, de parkentocht na de SPIE conferentie in San Diego samen met Lauge en Pechin was een grote belevenis waaraan ik met veel genoegen terugdenk. Een conferentiebezoek met daaraan

verbonden stedentrip wordt aanzienlijk vergemakkelijkt als je een gids hebt. Marcel, als vaste bezoeker van de RSNA wist jij die massale conferentie klein te krijgen en heb je me wegwijs gemaakt in Chicago. Bedankt voor de gezelligheid. En zo zou ik door kunnen gaan met de combinaties van ECR met Wenen, de MICCAI met Londen en ISBI met Rotterdam. Allemaal mooie ervaringen.

Hui, we did a lot of work together and your urge for results is admirable. It's an honour to be your paranymph. Guillaume, thanks for the cooperation on my last paper.

Petra en Desiree, zonder jullie support en reminders zou dit proefschrift nog een tijd op zich laten wachten. Bedankt voor alle ondersteuning.

Ellen, onze relatie is vrijwel even oud als mijn promotieonderzoek. Jij hebt me altijd de steun geboden die ik nodig had, ook al betekende dat soms dat je me wekenlang 's avonds en in de weekeinden moest missen. Je hielp me te focussen, doelgericht te werken en wist mij te stimuleren verder te gaan als het onderzoek niet de gewenste resultaten gaf. Het is goed dat dit promotieonderzoek wordt afgerond, maar een lange toekomst samen met jou is het mooiste dat ik me kan wensen.

Publications

Journal Papers

- **K. Hameeteman**, G.P. Zahnd, A. van der Lugt, W.J. Niessen, S. Klein, Cross-sectional and longitudinal carotid artery wall elasticity measurements on CTA and their relation to cardiovascular risk factors, *in preparation.*
- H. Tang, T. van Walsum, **K. Hameeteman**, R. Shahzad, L.J. van Vliet and W.J. Niessen, Lumen segmentation and stenosis quantification of atherosclerotic carotid arteries in CTA utilizing a centerline intensity prior, *Medical Physics*, 40(5),2013.
- **K. Hameeteman**, S. Rozie, C.T. Metz, R. Manniesing, T. van Walsum, A. van der Lugt, W.J. Niessen and S. Klein, Automatic carotid artery distensibility measurements from CTA using nonrigid registration, *Medical Image Analysis*, 17(5):515-524, 2013.
- **K. Hameeteman**, R. van 't Klooster, M. Selwaness, A. van der Lugt, J.C.M. Witteman, W.J. Niessen and S. Klein, Carotid wall volume quantification from magnetic resonance images using deformable model fitting and learning-based correction of systematic errors, *Physics in Medicine and Biology*, 58(5):1605, 2013.
- H. Tang, T. van Walsum, R.S. van Onkelen, **K. Hameeteman**, S. Klein, M. Schaap, Q.J.A. van den Bouwhuijsen, J.C.M. Witteman, A. van der Lugt, L.J. van Vliet and W.J. Niessen, Semiautomatic carotid lumen segmentation for quantification of lumen geometry in multispectral MRI, *Medical Image Analysis*, 16(6):1202-1215, 2012.
- **K. Hameeteman**, M.A. Zuluaga, M. Freiman, L. Joskowicz, O. Cuisenaire, L. Flórez Valencia, M.A. Gülsün, K. Krissian, J. Mille, W.C.K. Wong, M. Orkisz, H. Tek, M. Hernández Hoyos, F. Benmansour, A.C.S. Chung, S. Rozie, M. van Gils, L. van den Borne, J. Sosna, P. Berman, N. Cohen, P.C. Douek, I. Sánchez, M. Aissat, M. Schaap, C.T. Metz, G.P. Krestin, A. van der Lugt, W.J. Niessen and T. van Walsum, Evaluation framework for carotid bifurcation lumen segmentation and stenosis grading, *Medical Image Analysis*, 15(4):477-488, 2011.
- R. Manniesing, M. Schaap, S. Rozie, **K. Hameeteman**, D. Vukadinovic, A. van der Lugt and W.J. Niessen, Robust CTA lumen segmentation of the atherosclerotic carotid artery bifurcation in a large patient population, *Medical Image Analysis*, 14(6):759-69, 2010.
- D. Vukadinovic, T. van Walsum, R. Manniesing, S. Rozie, **K. Hameeteman**, T.T. de Weert, A. van der Lugt and W.J. Niessen, Segmentation of the outer vessel wall of the common carotid artery in CTA, *IEEE Transactions on Medical Imaging*, 29(1):65–76, 2010.

Conference Papers

- H. Tang, T. van Walsum, **K. Hameeteman**, M. Schaap, A. van der Lugt, L.J. van Vliet and W.J. Niessen, Lumen segmentation of atherosclerotic carotid arteries in CTA, *IEEE International Symposium on Biomedical Imaging 2012*, pages 274-277, 2012.
- H. Tang, M. Selwaness, **K. Hameeteman**, A. van der Lugt, L.J. van Vliet, W.J. Niessen and T. van Walsum, Semiautomatic carotid intraplaque hemorrhage segmentation and volume quantification by in vivo MRI, *The MICCAI Workshop on Computing and Visualization for (Intra)Vascular Imaging (CVII) 2011*, 2011.

- H. Tang, T. van Walsum, R.S. van Onkelen, S. Klein, **K. Hameeteman**, M. Schaap, Q.J.A. van den Bouwhuijsen, J.C.M. Witteman, A. van der Lugt, L.J. van Vliet and W.J. Niessen, Multispectral MRI centerline tracking in carotid arteries, *Proc. SPIE 7962, 79621N (2011)*, 2011.
- H. Tang, R.S. van Onkelen, T. van Walsum, **K. Hameeteman**, M. Schaap, F.L. Tori, Q.J.A. van den Bouwhuijsen, J.C.M. Witteman, A. van der Lugt, L.J. van Vliet and W.J. Niessen, A semi-automatic method for segmentation of the carotid bifurcation and bifurcation angle quantification on black Blood MRA, *Medical Image Computing and Computer-Assisted Intervention - MICCAI 2010,Volume 6363/2010, 97-104*, 2010.
- **K. Hameeteman**, S. Rozie, C.T. Metz, S. Klein, T. van Walsum, A. van der Lugt and W.J. Niessen, Automated carotid artery distensibility measurements from CTA using nonrigid registration, *Proceedings of IEEE International Symposium on Biomedical Imaging: from Nano to Macro, 2010*, pages 13-16, 2010.
- F. van der Lijn, M. de Bruijne, Y.Y. Hoogendam, S. Klein, **K. Hameeteman**, M.M.B. Breteler and W.J. Niessen, Cerebellum segmentation in MRI using atlas registration and local multi-scale image descriptors, *Proceedings of IEEE International Symposium on Biomedical Imaging: from Nano to Macro, 2009*, 2009.
- **K. Hameeteman**, J.F. Veenland and W.J. Niessen, Volume preserving image registration via a post-processing stage, *SPIE, Medical Imaging 2008: Image Processing*, 6914, 2008

Conference Abstracts

- H. Tang, T. van Walsum, **K. Hameeteman**, A van der Lugt, L.J. van Vliet and W.J. Niessen, Lumen segmentation of atherosclerotic carotid arteries in CTA, *BME2013*, 2013.
- H. Tang, T. van Walsum, R.S. van Onkelen, S. Klein, **K. Hameeteman**, M. Schaap, Q.J.A. van den Bouwhuijsen, J.C.M. Witteman, A. van der Lugt, L.J. van Vliet and W.J. Niessen, Carotid artery centerline tracking in multispectral MRA, *NVPHBV2011*, 2011.
- **K. Hameeteman**, M.A. Zuluaga, M. Freiman, A. van der Lugt and T. van Walsum, A standardized evaluation framework for automated carotid bifurcation lumen segmentation and stenosis grading methods, *Radiological Society of North America, 96th Annual Meeting*, 2010.
- K. Hameeteman, S. Rozie, C.T. Metz, R. Manniesing, T. van Walsum, A. van der Lugt, W.J. Niessen, S. Klein, Automated carotid artery distensibility measurements from CTA using nonrigid registration, *Dutch BME conference 2011* , 2011.
- H. Tang, R.S. van Onkelen, T. van Walsum, **K. Hameeteman**, F.L. Tori, Q.J.A. van den Bouwhuijsen, J.C.M. Witteman, A. van der Lugt, L.J. van Vliet and W.J. Niessen, Carotid segmentation and carotid bifurcation angle quantification in black blood MRA, *Dutch BME conference 2011* , 2011.
- S. Rozie, P.J. Homburg, **K. Hameeteman**, W.J. Niessen, D.W.J. Dippel and A. van der Lugt, Evaluation of pulsatile waveforms and mechanical properties in carotid arteries with ECG-gated dual-source CT angiography, *Radiological Society of North America, 95th Annual Meeting*, 2009.
- S. Rozie, P.J. Homburg, **K. Hameeteman**, J.J. Wentzel, D.W.J. Dippel, W.J. Niessen and A. van der Lugt, ECG-gated dual source CT angiography provides 4D-data to evaluate the distensibility of carotid arteries, *The third international symposium on biomechanics in vascular biology and cardiovascular disease*, 2008.

Conference Proceedings

- **K. Hameeteman**, M.A. Zuluaga, M. Freiman, L. Joskowicz, S. Rozie, M. van Gils, L. van den Borne, J. Sosna, P. Berman, N. Cohen, P.C. Douek, I. Sánchez, M. Aissat, A. van der Lugt, G.P. Krestin, W.J. Niessen and T. van Walsum, Carotid lumen segmentation and stenosis grading challenge, 2009.

Miscellaneous

- H. Tang, **K. Hameeteman**, A.G. Gelas and T. van Walsum, An implementation of the minimization of region-scalable fitting energy levelsets, *Insight Journal*, 2012.

PhD portfolio

Attended courses
Imaging Biomarkers (ESOR course) 2013
Presentation course (MI) 2011
EIBIR winter school 2010
Advanced MeVisLab Developers Workshop 2009
Pattern recognition course (BIGR) 2007
FSL & FreeSurfer course (Cardiff University) 2007
MeVisLab introduction course 2006
C++ course (BIGR) 2005

Given courses
MeVisLab C++ module development 2010
MeVisLab macro development 2007
Algorithm-Independent Machine Learning 2006
Introduction to image analysis for medical students 2009-2012

Student supervision
Supervision graduate student 2006-2007
Supervision 3 bachelor students 2010-2011

Conferences Presentations
Annual Meeting of the Radiological Society of North America (RSNA) 2010
IEEE International Symposium on Biomedical Imaging (ISBI) 2010
International conference on Medical Image Computing and Computer-Assisted Intervention (MICCAI) 2009
SPIE Medical Imaging 2007

Other presentations and conference and workshop attendance
European Congress of Radiology 2013
Reviewing for International Journal of Computer Assisted Radiology and Surgery 2011-2013
Third Dutch Conference on Bio-Medical Engineering (poster presentation) ... 2011
Machine learning for biomedical image analysis (ISBI workshop) 2010
Organisation BIGR trip 2010

Medical Informatics PhD days (oral presentation) 2009

Organization of international workshop:
'3D Segmentation in the Clinic: a Grand Challenge III', London, UK 2008
Demonstrations at the Medical Delta booth at ECR 2008
Information theoretic similarity measures for
image registration and segmentation (MICCAI workshop) 2009
European Congress of Radiology 2008
Imaging of carotid bifurcation atherosclerosis (COEUR Research Seminar) ... 2008
Medical Imaging Symposium for PhD students 2005,2008,2009,2011
Medical Informatics PhD days 2008-2011
MI Research colloquia (2 oral presentations) 2006-2012
BIGR Seminars (4 oral presentations) 2006-2012

About the author

Reinhard Hameeteman studied Applied Physics at Delft University of Technology, the Netherlands. In September 2006 he graduated at the Quantitative Imaging Group, Department of Imaging Science & Technology on "An error estimation method for non-rigid, mutual information based liver registration". This research was performed at the Biomedical Imaging Group Rotterdam (BIGR), Erasmus MC, The Netherlands. After his graduation he worked for two years as a scientific programmer and researcher at BIGR. This work was mainly focused on the analysis and registration of contrast enhanced liver series and segmentation tools for neuro image analysis. In October 2008 he started a Phd research project on image analysis of the carotid artery. The results of this research are described in this thesis. Together with four others he started the Erasmus MC spin-off Quantib in December 2012. Currently he is working as a research and development engineer at Quantib BV.

Quantib
Medical Image Quantification

CARDIALYSIS
Clinical Trial Management - Core Laboratories

fostering
discoveries